

# Experimental Study of the Spanwise Vortex Resonance Hypothesis for Turbulent Drag Reduction Over a Flat Plate in Salt Water

James C. S. Meng  
Stephen A. Huyer  
John M. Castano  
Daniel P. Thivierge  
Peter J. Hendricks  
Weapons Technology and Tactical Vehicle Systems Department



19970514 035

**Naval Undersea Warfare Center Division  
Newport, Rhode Island**

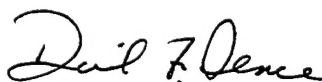
## **PREFACE**

This report was prepared under DARPA Order C341 PE 63569E, "Analysis of Electromagnetic Control of Turbulence," principal investigator J.C.S. Meng (Code 82). The sponsoring activity is the Defense Advanced Research Projects Agency (G. Jones, TTO).

The technical reviewer for this report was Promode R. Bandyopadhyay (Code 8233).

The authors express their appreciation to John Hoste, Jon Stinson, and Wayne Chancellor of McDonnell Douglas Technologies Inc. for making available MDTI's magnetic plate and controller schematics, and to Daniel M. Nosenchuck of Princeton University for providing his test matrix and skin friction reduction ratio. The authors also thank William J. Conforti (Code 5431) for his careful editing, James Q. Rice (Code 8233) for help in digitizing the spectral data, Robert N. Carpenter (Code 8212) for assistance with subsampling effects, and Promode R. Bandyopadhyay (Code 8233) for his thorough technical review and comments.

**Reviewed and Approved: 1 March 1997**



**David F. Dence**  
**Director, Weapons Systems**

REPORT DOCUMENTATION PAGE			Form Approved OMB No. 0704-0188	
Public reporting for this collection of information is estimated to average 1 hour per response, including the time for reviewing instructions, searching existing data sources, gathering and maintaining the data needed, and completing and reviewing the collection of information. Send comments regarding this burden estimate or any other aspect of this collection of information, including suggestions for reducing this burden, to Washington Headquarters Services, Directorate for Information Operations and Reports, 1215 Jefferson Davis Highway, Suite 1204, Arlington, VA 22202-4302, and to the Office of Management and Budget, Paperwork Reduction Project (0704-0188), Washington, DC 20503.				
1. AGENCY USE ONLY (Leave blank)		2. REPORT DATE 1 March 1997		3. REPORT TYPE AND DATES COVERED
4. TITLE AND SUBTITLE  Experimental Study of the Spanwise Vortex Resonance Hypothesis for Turbulent Drag Reduction Over a Flat Plate in Salt Water			5. FUNDING NUMBERS	
6. AUTHOR(S)  James C.S. Meng, Stephen A. Huyer, John M. Castano, Daniel P. Thivierge, Peter J. Hendricks				
7. PERFORMING ORGANIZATION NAME(S) AND ADDRESS(ES)  Naval Undersea Warfare Center Division 1176 Howell Street Newport, RI 02841-1708			8. PERFORMING ORGANIZATION REPORT NUMBER  TR 10,680	
9. SPONSORING/MONITORING AGENCY NAME(S) AND ADDRESS(ES)  Defense Advanced Research Projects Agency Washington, DC			10. SPONSORING/MONITORING AGENCY REPORT NUMBER	
11. SUPPLEMENTARY NOTES				
12a. DISTRIBUTION/AVAILABILITY STATEMENT  Approved for public release; distribution is unlimited.			12b. DISTRIBUTION CODE	
13. ABSTRACT (Maximum 200 words)  A series of tests was conducted by the Naval Undersea Warfare Center (NUWC) Division, Newport, RI, to assess the effectiveness of utilizing magnetohydrodynamic (MHD) technology for turbulent drag reduction. Methodologies applied in previous experiments conducted by Princeton University and McDonnell Douglas Technologies Inc. (MDTI) were examined. The matrix of specific test cases used in these earlier experiments was repeated, and the Princeton/MDTI magnetic plate (instrumented with electrodes and magnets) was provided to NUWC for these tests. The electrodes were pulsed in a specific pattern using an electrical controller constructed by NUWC based on the algorithm provided by researchers at MDTI. The plate was placed in the NUWC water tunnel, and careful measurements of skin friction (using hot-film anemometry) and integrated drag were made. A drag balance was designed and constructed by NUWC specifically for these tests to assess Princeton's and MDTI's reports of drag reduction.  The results obtained in the NUWC test series showed no integrated drag reduction based on force balance data. A consistent 8 to 15% skin friction reduction (based on hot-film measurements) was found locally downstream of the MHD controlled area. Analysis of the hot-film data showed skin friction reduction for only selected test cases. Detailed probability density function and spectral analyses were consistent with skin friction reduction.  A future program for evaluating flow control by electromagnetic forces is offered.				
14. SUBJECT TERMS  Turbulent Boundary Layers    Drag Reduction    Electromagnetics    Lorentz Force Electromagnetic Turbulence Control    Magnetohydrodynamics    Microturbulence			15. NUMBER OF PAGES 76	
			16. PRICE CODE	
17. SECURITY CLASSIFICATION OF REPORT Unclassified		18. SECURITY CLASSIFICATION OF THIS PAGE Unclassified		19. SECURITY CLASSIFICATION OF ABSTRACT Unclassified
20. LIMITATION OF ABSTRACT  SAR				

## TABLE OF CONTENTS

Section	Page
LIST OF ILLUSTRATIONS .....	ii
LIST OF TABLES .....	iii
1 INTRODUCTION .....	1
2 BACKGROUND .....	3
2.1 Literature Review .....	3
2.1.1 Streamwise Vorticity Inhibit Theory Based on Wall Layer Conductance by Electrolyte Injection and Counter-Vorticity Generated by Wallward Lorentz Pressure	3
2.1.2 Spanwise Vortex Resonance Theory .....	3
2.1.3 Simulation Results .....	5
2.1.4 Turbulent Boundary Layer Direct Resonance Theory .....	5
2.2 Technical Issues .....	6
2.2.1 Need for Basic Hydrodynamic Turbulence Measurements in Sea Water in Presence of EM Fields .....	7
2.2.2 Need for Processed Hydrodynamic Data .....	8
2.2.3 Need for Understanding of Skin Friction Reduction Mechanisms and Scaling Relationships .....	9
3 DESCRIPTION OF EXPERIMENTAL INVESTIGATION .....	11
3.1 Objectives .....	11
3.2 Experimental Setup .....	11
3.2.1 Sea Water Tunnel .....	11
3.2.2 Test Apparatus .....	12
3.2.3 Visualization of Lorentz Pressure Pulsing .....	19
3.2.4 Instrumentation .....	21
3.3 Experimental Test Conditions .....	28
3.3.1 MDTI/Princeton Test Matrices .....	30
3.3.2 NUWC Test Matrix .....	30
4 DATA ANALYSIS AND RESULTS .....	33
4.1 Time-Averaged Results .....	33
4.2 Turbulence Data Analysis .....	48
4.3 Pulsing Frequency Comparative Analysis .....	53
4.4 Relevance to Resonance Physics .....	55
5 DISCUSSION OF TEST SERIES DIFFERENCES .....	59
6 CONCLUSIONS .....	61
7 FUTURE DEVELOPMENT .....	63
8 BIBLIOGRAPHY .....	69
APPENDIX—EXPERIMENT TEST MATRIXES .....	A-1



## LIST OF ILLUSTRATIONS

Figure	Page
1 NUWC's Sea Water Tunnel Facility .....	12
2 MHD Flat Plate Test Bed Dimensions .....	13
3 MDTI Plate Situated in Floating Element Force Balance .....	14
4 Electrode Controller Block Diagram .....	15
5 Desired Electrode Switching Waveforms (Ideal) .....	16
6 Plate Layout and Corresponding Electrode Sequencing .....	17
7 MOSFET Power Stage .....	18
8 Ideal and Actual Electrode Voltage Waveforms from a Bundle of Electrodes .....	20
9 Actual Electrode Current Waveforms Taken from a Single Electrode .....	20
10 Ideal and Actual Electrode Voltage Waveforms Taken from a Single Electrode .....	21
11 Degraded Electrode Diagnostic Waveforms .....	22
12 Electrode Degradation Over Time in Salt Water .....	23
13 Floating Element Force Balance .....	23
14 Flexure Element Design .....	24
15 Static Force Balance Calibration Curve .....	25
16 Force Balance Dynamic Response .....	25
17 Standard and Customized Hot-Film Sensors .....	26
18 Frequency Response of Customized Hot-Film Sensor .....	26
19 Instrumentation Schematic .....	27
20 Typical Trace of a Hot-Film Signal, Illustrating Relevant Turbulent Time Scales at 1-Meter/Second Freestream Velocity .....	31
21 Baseline Skin Friction Coefficient Data for MHD-Off Test Cases .....	34
22 Average Drag Force for NUWC Repeat of the MDTI Tests .....	35
23 Difference in Average Drag Force for NUWC Repeat of MDTI Tests .....	35
24 Average Hot-Film Sensor Velocities for NUWC Repeat of MDTI Tests .....	36
25 Reduced Average Hot-Film Sensor Friction Velocities for NUWC Repeat of MDTI Tests .....	36
26 Average Friction Velocity (RMS Values) for NUWC Repeat of MDTI Tests .....	36
27 Average Local Shear Stress and Global Drag Reduction for NUWC Repeat of Princeton Tests: (a) 3 Meters/Second at 10 Volts vs Frequency; (b) 3 Meters/Second vs Voltage at Different Frequencies; (c) 3.7 Meters/Second at 17 Volts vs Frequency .....	38
28 Average Local Shear Stress and Global Drag Reduction for NUWC Repeat of Princeton Tests: (a) 1 Meter/Second at 5.5 Volts; (b) 1.4 Meters/Second at 6 Volts; (c) 1.8 Meters/Second at 6 Volts; (d) 2.3 Meters/Second at 8 Volts; (e) 2.7 Meters/Second at 10 Volts; (f) 3 Meters/Second at 21 Volts; (g) 3.4 Meters/Second at 21 Volts; (h) 3.7 Meters/Second at 21 Volts .....	39
29 Average Skin Friction Coefficient Data Compiled from Average Hot-Film Data and Global Drag Force Measurements for NUWC Repeat of Princeton Tests .....	41
30 Average Turbulence Intensity Results from NUWC Repeat of Princeton Tests .....	41
31 Average Difference in Drag Force and Standard Deviation of Drag for NUWC Test Series: (a) 4 Meters/Second at 10 Volts; (b) 4 Meters/Second and 500-Hz Pulsing Frequency .....	43
32 Average Difference in Drag Force and Shear Stress for NUWC Test Series: (a) 4 Meters/Second at 10 Volts; (b) 4 Meters/Second and 500-Hz Pulsing Frequency .....	44
33 Average Difference in Drag Force and Shear Stress for NUWC Test Series: (a) 5 Meters/Second at 10 Volts; (b) 5 Meters/Second and 500-Hz Pulsing Frequency .....	45

## LIST OF ILLUSTRATIONS (Cont'd)

Figure	Page
34 Average Skin Friction Coefficient Data Compiled from Average Hot-Film Data and Global Drag Force Measurements for NUWC Test Series.....	46
35 Average Turbulence Intensity Results from Entire NUWC Test Series .....	46
36 Skin Friction Coefficient Data for MHD-On and MHD-Off Test Cases .....	47
37 Probability Density Functions of Local Shear Stress Compiled from Hot-Film Data...	49
38 Probability Density Function of Shear Stress from Hot-Film Sensor Located Adjacent to MHD Array (3.4 Meters/Second, 21 Volts, 150-Hz Pulsing Frequency).	49
39 Probability Density Function of Shear Stress from Downstream Hot-Film Sensor (3.4 Meters/Second, 21 Volts, 150-Hz Pulsing Frequency).....	50
40 Probability Density Function of Shear Stress from Hot-Film Sensor Located Adjacent to MHD Array (4 Meters/Second, 25 Volts, 70-Hz Pulsing Frequency).....	50
41 Probability Density Function of Shear Stress from Downstream Hot-Film Sensor (4 Meters/Second, 25 Volts, 70-Hz Pulsing Frequency).....	51
42 Power Spectrum (Scaled by Inner Variables) of Wall Shear Stress (3.4 Meters/Second, 21 Volts, 150-Hz Pulsing Frequency).....	52
43 First Moment of Power Spectrum (Scaled by Inner Variables) of Wall Shear Stress (3.4 Meters/Second, 21 Volts, 150-Hz Pulsing Frequency). ....	52
44 Dominant Turbulent Boundary Layer and MHD Pulsing Frequencies of the Entire Current Test Series. ....	54

## LIST OF TABLES

Table	Page
1 Summary of Test Conditions.....	29
2 Dominant Flow Frequencies for MHD Plate.....	54
A-1 MDTI Test Matrix .....	A-1
A-2 Princeton Test Matrix .....	A-2
A-3 NUWC Test Plan.....	A-3

# EXPERIMENTAL STUDY OF THE SPANWISE VORTEX RESONANCE HYPOTHESIS FOR TURBULENT DRAG REDUCTION OVER A FLAT PLATE IN SALT WATER

## 1. INTRODUCTION

Ever since the discovery of turbulent boundary layers, fluid dynamicists have been investigating and pursuing drag reduction techniques. The Germans pioneered drag reduction via shaping, control of flow separation, suction, and blowing, and the British chemical industry initiated work in polymer drag reduction. Over several decades, the U.S. Navy has actively investigated laminar flow control using delayed laminar transition via heating and suction, and turbulent flow control using riblets, compliant surfaces, large eddy breakup devices (LEBUs), and polymer injection. The many experiments conducted on boundary layer transition, separation, and control have demonstrated the powerful effects of boundary layer control on the lift and drag forces acting on a body, even after taking into account the accompanying weight, space, and power penalties.

Certain properties of turbulent boundary layers, including the *streak-sweep-eject* sequence in the flow structure near the wall and the large coherent structures in the mixing layer, can be potentially controlled. The connection between Reynolds stress and coherent motions in the near-wall region has been exploited previously for controlling the dominant stress-producing motions through approaches such as riblets and LEBUs, which are passive turbulence control approaches.

Electromagnetic forces have been shown to be effective in modifying both the mean flow and fluctuations in boundary layers (Tsinober, 1990; Watanabe, 1987; Nosenchuck and Brown, 1992-1995; Meng, 1995; Henoch and Stace, 1995). Salt water experiments using an array of magnets and electrodes consisting of alternating strips of magnets and electrodes aligned parallel to the mean flow on the surface of a flat plate produced a streamwise Lorentz force that resulted in significant changes in the mean flow and fluctuating components. These effects have been demonstrated in a sea water tunnel over a flat plate at speeds of up to 4 meters/second. A variety of diagnostic instrumentation was used, including flow visualization with dye, flush-mounted hot-film sensors, and laser Doppler velocimetry (LDV). The flow measurements proved to be challenging because of the presence of stray fields and electrolytic bubbles. The use of the Lorentz force to suppress the formation of coherent structures in turbulent boundary layers is an active approach and is a significant innovative concept in boundary layer control.

The premise underlying electromagnetic turbulence control is that a Lorentz pressure gradient actively generated by an electric current flowing in the conducting water in the presence of a magnetic field can be used to control (and suppress) the formation of coherent motions in the boundary layer. It is postulated that the Lorentz force provides a stabilizing effect on low-momentum fluid being lifted away from the wall. The magnitude of the effect is influenced by the electromagnetic field density near the wall and its coupling with fluid motion to minimize or eliminate turbulence production in a boundary layer.

Nosenchuck and Brown (1992-1994) used a plate with a "checkerboard" geometry consisting of opposing pairs of magnets and electrodes to produce a Lorentz pressure gradient toward the wall. This configuration, which will be described in detail later, produced a time-varying, complex, three-dimensional distribution of the Lorentz force, with a major component that is normal to the plate in the center of the array. Their experiments were performed in a water channel at relatively low Reynolds numbers (up to 100,000). In their first set of experiments, a thin layer of high-conductivity electrolyte was injected near the surface into essentially fresh water. As this electrolyte layer passed over the array, levels of turbulence and

drag reportedly decreased dramatically. In a second set of experiments (Nosenchuck and Brown, 1995), the array of checkerboard cells was pulsed periodically in a fixed pattern, also producing a reported reduction of drag and turbulence. In these latter experiments, there was no electrolyte injection, and the fluid was a weak electrolyte with a conductivity less than one-tenth that of sea water. Flow visualization, traversing hot-film sensors, and a drag balance were used for flow diagnostics. The results of these experiments demonstrated that electromagnetic forces can be effective in modifying salt water turbulent flows.

In 1994, McDonnell Douglas Technologies Inc. (MDTI) conducted electromagnetic turbulence control experiments in the NRad water tunnel, using a 3% solution of sodium hydroxide as the electrically conducting medium. For 68 full days over a 9-month period, MDTI tested numerous iterations of magnetohydrodynamics (MHD) panel and instrumentation designs at Reynolds numbers of up to 3,000,000. Instrumentation consisted of a drag balance, LDV, and hot-film sensors. LDV was used mainly for characterizing the boundary layer profiles, while the hot-film sensors were used for local measurements. No technical details of these experiments are available, although Eng (1995) and Culuer (1996) give some results for laminar, but not turbulent, boundary layers.

Both the MDTI experiments and the Nosenchuck and Brown experiments at Princeton were based on the *spanwise vortex resonance hypothesis*, which holds that spatially distributed flow vorticity, countering what is naturally concentrated near the wall, will reduce drag away from the wall. This hypothesis is discussed in section 2.

Some description of the experimental conditions and corresponding theoretical basis for the Princeton/MDTI tests is available in patent disclosures (Nosenchuck and Brown, 1994a,b-1995), but this information is not detailed enough to allow analysis of the accuracy and validity of the flow control methodology employed. Therefore, NUWC researchers conducted a series of tests to evaluate the Princeton/MDTI findings, using a matrix of the same test cases examined by Princeton/MDTI. In the NUWC tests, the electrodes were pulsed in a specific pattern using an electrical controller constructed by NUWC based on an algorithm provided by MDTI. The actual MDTI plate (instrumented with electrodes and magnets) was situated in the NUWC sea water tunnel and careful measurements of skin friction (using hot-film anemometry) and integrated drag were conducted. A drag balance was designed and constructed specifically for these experiments.

This report details the results of the NUWC experiments conducted to assess the Princeton/MDTI hypothesis and flow control scheme. In addition to presenting experimental findings and conclusions, it proposes a three-phase program for evaluating flow control by electromagnetic forces, including further assessment of both the spanwise vortex resonance hypothesis and Meng's microturbulence inhibition theory.\*

---

\*Meng (1995) has postulated an alternative to the spanwise vortex resonance hypothesis that is based on a turbulence production process characterized by identifiable, discrete microturbulent events. The complete sequence of events occurs in a Lagrangian reference frame and may be predicted to occur in a probabilistic sense. Based on experimentally observed probability density functions and the sequence of microturbulent events, Meng's conceptual probabilistic model of dependent random variables begins with *low-speed streaks*, proceeds to *liftups*, and then *sweeps*. Each microturbulent event contributes to the wall shear stress. When a Lorentz force is applied, the frequency of occurrence of these microturbulent events is changed in a manner that reduces the transition probability toward the shear-stress, or drag, generation end of discrete events, thereby interrupting the turbulence production cycle. A decrease in turbulence production and Reynolds stresses should result in an overall drag reduction. The objective is not to totally eliminate turbulence but only to inhibit turbulent ejection and sweep, allowing the low-speed streaks to exist and persist since they contribute to a more naturally stable mode of flow near the wall and are responsible for a low level of shear stress and therefore skin friction drag.

## 2. BACKGROUND

### 2.1 LITERATURE REVIEW

#### 2.1.1 *Streamwise Vorticity Inhibit Theory Based on Wall Layer Conductance by Electrolyte Injection and Counter-Vorticity Generated by Wallward Lorentz Pressure*

Nosenchuck and Brown (1993) were the first to introduce the concept of populating the boundary layer and associated turbulent flow with discrete, independent electromagnetic-controlled regions. Their hypothesis is based on the direct control of (1) the coherent motions responsible for turbulence production, (2) the normal velocity fluctuations, and (3) the Reynolds stresses in the near-wall region. In addition, their hypothesis requires that the relaxation time that results after removal of the Lorentz force exceed the time for the flow to respond to the force itself. They theorized that the counter-vorticity generated by the Lorentz force would inhibit the coupling between the inner and outer regions in the boundary and suppress the amplification of the streamwise vorticity. The details are provided in Nosenchuck and Brown's (1994a) patent for the single-tile concept. Their experiments were conducted in a fresh-water channel on a flat plate turbulent boundary layer ( $Re_\theta \approx 1100$ ), where the conductance  $\sigma$  of the boundary layer was enhanced by supplying a small flux of dilute sodium hydroxide electrolyte having an optimal conductivity-enhancing layer thickness of  $10 < y^+ < 30$ . For the single-tile experiment, the magnetic flux  $B_z$  was  $\approx 0.05$  tesla, the steady-state electrical current density  $j$  was  $\leq 20$  mA/cm<sup>2</sup> (over a dimension on the order of  $x^+ \approx 1000$ ,  $z^+ \approx 500$ ), and the laser sheet illumination was at a height of  $y^+ \approx 1$ . The flow visualization results indicated complete lack of vertical transport from the near-wall region with the electric field turned on, thereby substantiating the observation of reduced time-series axial velocity fluctuations. It was expected that the relaxation time after electric field was turned off would be long compared with the time for the flow to respond to the Lorentz force, and that the MHD-on time would be short compared with the relaxation time. Conversely, Nosenchuck and Brown (1994a) stated that by reversing the Lorentz pressure away from the wall one can destabilize the flow in the boundary layer and induce turbulence.

For their three-tile experiment, the electrodes were sequentially activated at 10 Hz, 1/3 duty cycle, flow speed at 0.15 meter/second, and  $Re_\theta \approx 1350$  in a test tank 1.5 meters wide, 0.5 meter high, and 6 meters long. The magnetic flux  $B_z$  was  $\approx 0.016$  tesla, and the maximum electrical current density  $j$  was  $\leq 10$  mA/cm<sup>2</sup>. Three tiles cover a total dimension of 0.24 meter streamwise by 0.18 meter spanwise (or in terms of viscous units  $x^+ \approx 1500$  by  $z^+ \approx 1150$ ), and the individual tile dimension is on the order of  $x^+ \approx 500$ ,  $z^+ \approx 1150$ . The laser sheet illumination was at a height of  $y^+ \approx 20$ . When the tiles were activated, little dye was seen in the laser sheet, indicating a decrease of vertical transport, with an expected attenuation of near-wall turbulent motions. A turbulent spot was also artificially generated upstream of the MHD region, and the turbulence disappeared once it entered the MHD region. The injection of conductivity-enhancing electrolyte was still believed to be necessary.

#### 2.1.2 *Spanwise Vortex Resonance Theory*

Nosenchuck and Brown (1995) received another patent for a multiple, sequentially activated MHD tile concept. In this concept, the capability of generating a Lorentz pressure gradient normal to the wall by the injection of a wall layer of electrolyte was replaced by pulse phasing control of the MHD cells. Conceptually, pulse phasing creates a series of rotational flow regions in the boundary layer, and these rotational flow regions continually reinforce the small



amount of vorticity created by the gradients of the Lorentz pressure vector. It was conceptualized that a “critical” velocity profile could be maintained that would reduce the drag to that between laminar flow and uninhibited turbulent flow. The spacing of the MHD cells was described to be 10 times the height of the usable field strength based on the Maxwell equations, although no derivation was given. The optimal frequency of the equal-phase tiles was determined experimentally. It was found that a critical frequency exists at which a condition analogous to resonance is attained; this frequency is expressed as  $f_{critical} \propto U_{\infty}/d_{cell}$ , where  $U_{\infty}$  is the freestream velocity and  $d_{cell}$  is the cell spacing. Without electrolyte injection, experiments were conducted over a different eight-cell array (having dimensions of 0.3 meter streamwise by 0.4 meter spanwise) with a magnetic flux  $B_z$  of 0.6 tesla and  $j \approx 100$  mA/cm<sup>2</sup>. Each equal-phase tile was actuated for 0.75 second at 1/4 duty cycle and at a flow velocity 0.3 meter/second, so that  $f_{critical} \approx 3$  Hz. The measured drag was reduced by 90%, from 0.1 N/m<sup>2</sup> to about 0.01 N/m<sup>2</sup>.

Subsequently, Nosenchuck (1995a) conducted more experiments without electrolyte injection in a small water tunnel using a sodium hydroxide solution having an electrical conductivity of  $\sigma \approx 2.5$  siemens/meter. The 8 x 8 array MHD plate was 8 inches x 15 inches in size, with center-to-center spacing of 0.7 inch between stainless electrodes and neodymium boron iron magnets. Altogether, there were 64 electrodes arranged with 8 spanwise electrodes in each of 8 streamwise rows. At speeds from 0.075 to 0.3 meter/second,  $Re_x \approx 5-7.5 \times 10^5$ , the flows ranged from the laminar to transitional regimes. By injecting dye from the leading edge and using laser-induced fluorescence of disodium fluorescein, they clearly visualized the ability of the Lorentz pressure gradient to create wave-like rotational flows near the wall.

Using a maximum magnetic induction of 0.7 tesla and applying 4 to 7 volts (0.5-2 amps) for laminar flow, 7-15 volts (2-4 amps) for transitional flows, and 15-38 volts (4-12 amps) in turbulent flows, they determined empirically the critical frequencies from 4 Hz (0.075 meter/second) to 900 Hz (4 meters/second). When MHD was activated, hot-film sensor output traces indicated 80% reduction at 0.525 meter/second and 25% to 55% reduction at 4 meters/second. The basic premise was that vorticity rotating counter to that naturally generated on the wall would push the maximum vorticity away from the wall. The maximum effect occurs when the vorticity source on wall generates a wave pattern that resonates with the natural vorticity source and therefore reduces the skin friction. They also demonstrated the so-called critical frequency (at about 300 Hz at 1 meter/second), above which no bubbles were generated.

Subsequently, Nosenchuck (1995b) reported refined experimental results from surface hot-film sensors that measured the spanwise variation of streamwise shear stress, from cylindrical hot-film sensors that traversed normal to the wall to measure streamwise velocity, and from pitot tubes that measured freestream characteristics. At low speeds (0.07 meter/second,  $Re_x \approx 6 \times 10^4$ ), with streamwise magnets and cross-stream electrodes operated at 3 volts, 0.2 amp, and from 2 to 3.5 Hz, results of streamwise velocity profiles revealed the expected near-wall jet-like feature. Coefficients of friction versus Reynolds number showed that these results were substantially lower than the well-established laminar flow lines, which raised issues of their tunnel flow ambient pressure gradient. By showing the drag reduction ratio versus the power ratio, defined as the ratio of MHD power to that naturally occurring, Nosenchuck expected that the maximum drag reduction ratio would be obtained at the point where the power ratio equals one. In laminar flows at speeds of 0.1 and 0.3 meter/second, the power drag ratio increases beyond one (meaning a drag increase), while in turbulent flows at speeds of 1.0 and 3.0 meters/second, the drag ratio remains below one (meaning a drag reduction even as the power ratio increases beyond one).

Nosenchuck (1996) presented test results from another novel axisymmetric model. A roughly 10-inch-diameter, 3-foot-long model with a teardrop tailcone and numerous tiles was released for buoyant rise in a 6-meter-tall pipe filled with salt water. The model broke through

the water surface and dropped back into the water. Using magnets affixed to the buoyant model and tracking the time history of the trajectory as the model rose, acceleration due to the activation of MHD can be interpreted as a 50% net drag reduction. As the difference in the time history is very small (0.1 second out of 3 seconds of transit time), more persuasive evidence is needed to substantiate the 50% drag reduction.

Observing that all reported MHD experiments have been based on open-loop control (i.e., all experimental investigators have basically explored trial-and-error matrices without a theoretical basis or a means for optimization), Bandyopadhyay and Castano (1996) explored the possibility of a higher payoff by using a more rational closed-loop control with feedback. They proposed that the Lorentz pressure over a tile would generate a Stokes layer of vorticity having a height on the order of  $\sqrt{2\nu/f}$ , which is equivalent to a thin wall layer with height of 1 mm. They derived a resonance frequency of 70 Hz, which is in reasonable agreement with their  $5 \times 5$  array of microtiles. This observation can actually be further extended to a more general relationship between the Stokes layer and the ideal height of the microturbulent events, or the height  $y^+ \approx 10$  where maximum turbulence production takes place. In other words,  $\sqrt{2\nu/\omega} \approx 10 \nu/u_\tau$ , or  $f \approx u_\tau^2/(100 \pi \nu)$ , so that a quadratic dependence of the resonance frequency on the speed is expected. This frequency is denoted as  $f_{Bandy}$  in the appendix.

### 2.1.3 Simulation Results

Watanabe (1978) analyzed the MHD stability of an incompressible, electrically conducting fluid, boundary layer flow along a flat plate in the presence of a transverse magnetic field without an imposed electric field. Later, he conducted a similar analysis but with uniform suction or injection (Watanabe, 1987). He calculated the neutral stability curves of Tollmien-Schlichting waves and the critical Reynolds numbers for various values of the MHD interaction parameter and the suction or injection parameter. He concluded that (1) stability increases with increasing MHD interaction and increasing suction parameters, (2) the friction coefficient decreases with increasing MHD interaction and increasing injection parameters, and (3) the displacement thickness increases with increasing MHD interaction and increasing injection parameters.

Kral (1996) carried out turbulence modeling over an MHD flat plate. Her results showed regions where the MHD interaction parameter was significant. Drag reduction vanished in these regions and reached levels of 50% drag reduction between these regions.

Crawford and Karniadakis (1996) conducted a direct Navier-Stokes equations simulation in a fully developed turbulent channel flow to simulate Nosenchuck's experiment on inclined waves and pulsed powering. Their calculations showed a drag reduction on the order of 5%, which is far below the claimed 50%. Such channel flow numerical simulations are becoming progressively more realistic and therefore significant, because it is practically very challenging to make a fine-resolution, MHD, experimental drag measurement.

### 2.1.4 Turbulent Boundary Layer Direct Resonance Theory

A convincing "resonance mechanism" for a natural turbulent boundary layer without MHD effects was derived by Jang, Benney, and Gran (1986). Benney and Gustavsson (1981) first introduced the "direct resonance concept" that a three-dimensional disturbance with certain wavenumbers can grow to a relatively large amplitude. This concept draws from the empirical observation by Morrison and Kronauer (1969) of wavelike streamwise fluctuations so that a weakly nonlinear perturbation around the mean velocity might be applicable to the turbulent

boundary layer bursting process and from the observation by Blackwelder (1983) of the similarity between bursting and the laminar-turbulent transition phenomenon. Guided by this insight, Jang et al. (1986) replaced the Blasius profile with the mean turbulent profile (including the sublayer, law of the wall, and logarithmic law of wake profiles) and examined the Orr-Sommerfeld and the vertical vorticity equations. The linearized vertical vorticity equation contains a forcing term, related to the vertical velocity, that provides the physical link. Wherever eigenvalues of both equations in the wavenumber space are identical, the resonant growth occurs at the streamwise wavenumber  $\alpha^* \approx 0.0093$ , spanwise wavenumber  $\beta^* \approx 0.035$ , and frequency  $\omega^+ \approx 0.09$ . Notice that  $\tan^{-1}(\beta^*/\alpha^*) \approx 15^\circ$  for the wedge pattern well known in the transition regime. These theoretical results agree well with the experimental data obtained by Morrison and Kronauer (1969). Further, by applying a nonlinear perturbation method, Jang et. al. (1986) showed that this resonance mechanism produced a mean flow of counterrotating streamwise vortices in a turbulent boundary layer.

Relating this well-established theoretical foundation to Nosenchuck and Brown's (1995) spanwise vorticity resonance hypothesis, there appears to be a valid scientific basis for expecting that, if the naturally occurring frequency and wave pattern are detected and countered by the applied MHD  $90^\circ$  out of phase, a significant reduction of turbulence and drag reduction can be achieved.

## 2.2 TECHNICAL ISSUES

While previous experiments have provided some answers regarding MHD phenomena, a number of general issues remain to be resolved in the future development of MHD technology. Some of these issues are:

- *Scaling Laws* - Relationships must be developed that will enable design of systems of various sizes capable of operating over a range of speeds.
- *Spatial Field Modulation* - Given the optimum size and pattern of cells in an array to maximize the persistence of the turbulence reduction, an MHD array must optimize performance with a minimal number of elements.
- *Temporal Field Modulation* - There are indications that MHD devices do not need to be operated continuously to be effective. It may be possible to define the pulsing duration at relatively short duty cycles that will minimize power consumption and to selectively activate elements in the MHD array to maximize effects while minimizing power requirements.
- *Persistence of Drag and Turbulence Reduction* - Experiments to date have demonstrated suppression of turbulence within the MHD cell. If this effect persists for a significant distance downstream of the cell, turbulence control may be effected with a relatively sparse array of cells, which would reduce fabrication cost and onboard power requirements.
- *Sea Water Electrochemistry* - As the electric current passes between the electrodes of the MHD device, complex reactions take place at the electrode/sea water interfaces. These reactions include changes in ion composition near the electrodes and the formation of bubbles. The electrochemistry of these reactions in sea water must be taken into account in an MHD system. Also, corrosion and durability of electrodes and magnets in the sea water environment need to be addressed.



- *Efficiency and Power Requirements* - The strength of the Lorentz force and its gradients is proportional to the supplied electric current. MHD configurations should normally be optimized to minimize the power consumption.
- *Overall System Integration* - Each MHD application represents a unique opportunity to capitalize on attributes of the overall system. For example, overboard discharges of electrolyte or heat exchanges for a flowing-electrolyte, high-power-battery electric drive also may provide opportunities for conductivity enhancement. System characteristics for drag reduction may be quite different from those for noise reduction (at a given wave number) and will certainly be different from those for controlling separation.

### ***2.2.1 Need for Basic Hydrodynamic Turbulence Measurements in Sea Water in Presence of EM Fields***

Turbulence measurement in salt water is a challenge by itself. Furthermore, it is even more difficult to make these measurements in the presence of EM fields. For example, it is well known that LDV measurements may not be accurate in the presence of bubbles; quantifying LDV bubble effects using electrodes without the magnets would isolate the effect of the bubbles without Lorentz forces and could be a simplifying and effective approach.

Similar challenges apply to hot-film measurements. In the MDTI/Princeton hot-film data, there appears to be a sensitivity to the electrode driver voltage (it is not known whether electrical insulation was adequate). The validity of hot-film data could be confirmed simply by generating a histogram, which should follow a Rayleigh distribution. Also, in the laminar flow regime, hot-film output should approximately follow an impulse function distribution. Without such confirming evidence, hot-film measurements are not trustworthy. Further, drag balance results are crucial for corroborating hot-film skin friction results. Precise drag balance measurements have not been made in the MDTI/Princeton tests.

No experimental investigation of phased pulsing MHD has been conducted in sea water or in salt water (sodium chloride). For MDTI's sodium hydroxide tests, the test team did not match the specific electrical conductivity level (2.5 siemens/meter) with the average sea water conductivity level (5 siemens/meter). In addition, the electrodes were reportedly made of stainless steel, which—even with precious metal coating—will not withstand sea water corrosion. Ignoring the corrosion factor and using a material that will not be durable in sea water severely limits test versatility and raises issues of test apparatus integrity. Since sea water electrochemistry is a major consideration for practical applications, all future tests should employ electrodes of a more durable material, such as rare earth oxides coated with a titanium substrate.

Electrolytic bubble generation and its effects on the hot-film sensors have not been addressed in depth. Huyer (1995) conducted a set of bubble formation experiments in sodium chloride and sodium hydroxide solutions of equivalent electrical conductivity. There appears to be a significant effect of solution at a 50% duty cycle. That is, sea water has a lower threshold for electrolytic bubble formation, so that the conclusions for the sodium hydroxide solution may not generally apply to the sea water medium. However, at a 25% duty cycle, sea water and the sodium hydroxide solution have comparable thresholds for bubble formation. Because most MHD algorithms can be employed at a less than 25% duty cycle, bubble formation may not be an issue in future applications, and the continued use of sodium hydroxide solutions for a laboratory test media may be acceptable. Since sea water is the intended application medium, the chemical

composition of sodium chloride and sea water itself need to be understood. Also, better understanding is needed of variations in reverse polarization voltage and of the time constant of bubble formation versus the active MHD-on time.

### *2.2.2 Need for Processed Hydrodynamic Data*

Turbulent drag and skin friction coefficient data for phased pulsing MHD versus Reynolds number with and without electric currents do not exist. While consistent skin friction reduction was reported by MDTI, no concomitant drag reduction was observed. Measured skin friction reduction at low speeds (0.3 meter/second) was reported by Nosenchuck and Brown (1992, 1994a), but no drag reduction data were provided. The results included only the voltage output of a hot-film sensor placed aft of the MHD test panel over the speed range from 1.0 to 3.5 meters/second. At each velocity, MHD was turned on and a drop in hot-film voltage was recorded, which was interpreted to be the result of a lower wall shear stress. However, a drop in local shear stress at the aft end of the plate could be a result of increasing boundary layer thickness, which would increase the form drag and, therefore, the total drag over an axisymmetric body. This potential problem is similar to the observed phenomenon for the LEBU devices, where large local shear stress reductions are measured in the vicinity of the device; however, when the form drag of the device is added, drag actually increases. From videotape at 0.075 meter/second, Nosenchuck and Brown's (1993) hypothesis is based on a thickened turbulent boundary that redistributes vorticity away from the wall. Thus, this hypothesis may be trading a reduction in skin friction for an increase in form drag—a condition that cannot be detected with a flat plate test apparatus. When this concept is applied to an axisymmetric body, the drag reduction would be offset by an increase in form drag. Drag balance measurements of the integrated effect are needed for demonstration of this technology. Corroboration of the drag data from a force balance and of the skin friction data from hot-film data is needed.

The array of hot-film sensors used in Nosenchuck and Brown's experiment was very sparse. Only three hot-film probes were located at the end of the MHD plate—an insufficient number to quantify the startup length upstream and persistence distance downstream. Nosenchuck and Brown's (1993) hot-film measurements exhibit large differences between sensors at different positions downstream of the magnets and electrodes. Certainly not enough hot-film sensors were employed to properly characterize the area where drag reduction, if any, takes place.

The actual Lorentz force distribution on the plate, resulting in global or local drag reduction, cannot be ascertained from a sparse array of hot-film sensors. With MHD applied, owing to the three dimensionality of the effects, there could be significant edge effects that make the drag balance data difficult to correlate with the hot-film data. A large flat plate test with a load cell would be one way to validate and correlate hot-film results. Other approaches include injecting dye from the leading edge corner of the MHD plate by sequentially turning off rows of the MHD plate, starting at the leading edge.

Finally, for an understanding of the physics, experimental data need to be presented over a range of Reynolds number  $Re_x$  and MHD interaction parameter  $N$ , as well as load factor  $L$ . These data do not exist at the present time.

### **2.2.3 Need for Understanding of Skin Friction Reduction Mechanisms and Scaling Relationships**

Nosenchuck and Brown's (1992, 1993) tests and flow visualization at extremely low Reynolds numbers (1000) do shed some light but are not useful in turbulent flows. Videotape data of channel flow at a speed of 0.075 meter/second showed that vortex reinforcement resulted when an MHD panel was operated at a "resonant" forcing frequency. Similarly in a low-speed turbulent flow, various wave-like phenomena were shown in the dye traces when the MHD panel was operated in a resonant mode. Concurrent with these findings, an oscilloscope trace of a hot-film sensor showed drag reduction at "on resonance" and a hot-film voltage increase at "off resonance." This resonance phenomenon was postulated by Nosenchuck and Brown (1994a) as the drag reduction mechanism.

As noted earlier, Nosenchuck and Brown (1993) also originated the hypothesis of the vertical redistribution of spanwise vorticity. Their model uses the curl of the Lorentz force to reduce the concentration near the wall and redistribute the spanwise component of vorticity throughout the boundary layer. The two components in the vorticity equation are the normal derivative of the streamwise Lorentz force and the streamwise derivative of the normal Lorentz force. It is not known which of these components dominates the vorticity transport. If it is the latter (i.e., the horizontal derivative), the transport should be relatively insensitive to magnet orientation. If it is the former (i.e., the vertical derivative), the transport would be greatly affected by magnet orientation because the horizontal components of Lorentz force, which derive from fringing fields, do change as a result of rotation of the array. Neither of these possibilities was tested in light of the existence of the experimental data. Analyses conducted by Hendricks (1996) suggest that the spanwise component of the vorticity transport is proportional to the normal derivative of the electric field.

The scaling relationship issue is not addressed. Since both the spatial and temporal scales vary with Reynolds number, the effectiveness of this methodology needs to be expressed in terms of dimensionless variables.

The proper way to address the above issues is to conduct a thorough experimental investigation and provide a detailed presentation of the test results, including a description of design principles; the postulated physics of turbulence reduction; descriptions of the test apparatus, test matrix, data processing methodology and uncertainty, and test results; quantification of the effectiveness of the postulated theory versus observed test results; and a recommended roadmap for future work. The recorded test data must include power level, drag versus speed, shear stress at several downstream stations, turbulence statistics (such as the Reynolds stress at a  $y^+$  station), and corresponding dye injection flow visualization photographs.

In summary, more detailed descriptions are needed of test matrixes, test media, plate geometry details such as the leading edge configuration, trip devices, minimum and maximum Reynolds numbers, flow conditions (speed and ambient turbulence levels), measurement instrumentation, and processing bandwidth.

### 3. DESCRIPTION OF EXPERIMENTAL INVESTIGATION

#### 3.1 OBJECTIVES

The objective of the tests described in this report was to assess the performance of the Princeton/MDTI electromagnetic flow control methodology.

For these tests, the MHD plate developed by MDTI and tested in the NRaD flow facility was incorporated into a flat plate drag balance constructed by NUWC (Castano, 1997). The tests, conducted over an extended parameter range in NUWC's sea water tunnel facility, directly measured the change in total drag that results from applying electromagnetic forces to the flow over the plate. Flow measurements of velocity and shear stress were also made. To simulate the salinity for a future test at the Langley Tow Tank, a 1.6% sodium chloride solution was used as the test medium. The earlier tests conducted by MDTI and Princeton had used a sodium hydroxide solution to reduce electrode corrosion.

#### 3.2 EXPERIMENTAL SETUP

##### 3.2.1 *Sea Water Tunnel*

Testing was conducted in the sea water tunnel facility (figure 1). This facility has a 1-foot<sup>2</sup> by 10-foot-long test section, and its variable-speed 30-hp motor provides a maximum flow velocity of 25 feet/second. The axial flow pump has four adjustable pitch blades, with blade twist designed to give uniform radial velocity profiles. All wetted parts are made of stainless steel or plastic, with external stiffeners made of mild steel. The inlet nozzle has a contraction ratio of 9:1, and its contour is determined by a ninth-order polynomial having five derivatives set to zero at the exit and three derivatives at the entrance; this arrangement promotes minimal disturbances during flow acceleration. A stainless steel honeycomb with 0.25-inch hexagonal cells, 6 inches thick (for an aspect ratio of 24) is located upstream of the inlet nozzle. All flow diffuser sections have included angles of 6° or less to minimize separation. The test section surface area is composed of 16 removable plexiglas windows or stainless steel panels that provide exceptional visual access into the test area; these windows or panels, each being 2 feet long and 10 inches high, make up more than 65% of the test section. To compensate for boundary layer growth, the test section cross-sectional area increases downstream—the bottom surface of the test section sloping downward 5/8 inch over its 10-foot length. Static pressure taps are provided at 4-inch intervals along the centerline of the test section. The MHD plate has a trailing edge fin that can be adjusted to control the pressure gradient in the test section over a wide range of speeds. In these tests the fin was set to achieve a zero pressure gradient in the test section.

The sea water tunnel is equipped with a speed control system that monitors and adjusts the tunnel flow rate via a variable-speed Eaton Dynamic Coupling device. The motor, which operates at a normal speed of 1725 rpm, is magnetically coupled to the pump with adjustable amounts of slip controlled by a relatively small dc energizing current. The facility has an online air removal or deaeration system that withdraws a portion of the circulating water (no more than 10% by volume) from the tunnel on a continuous basis. The bypassed water is then allowed to cascade down inclined plates located in a vacuum tank before being pumped back into the tunnel circuit. In addition, the tunnel has an automatic pressure control system that monitors and maintains test section pressure at a desired level. The pressure control device is an air-over-water system that corrects for mass transfer to and from the tunnel flow volume continuously.

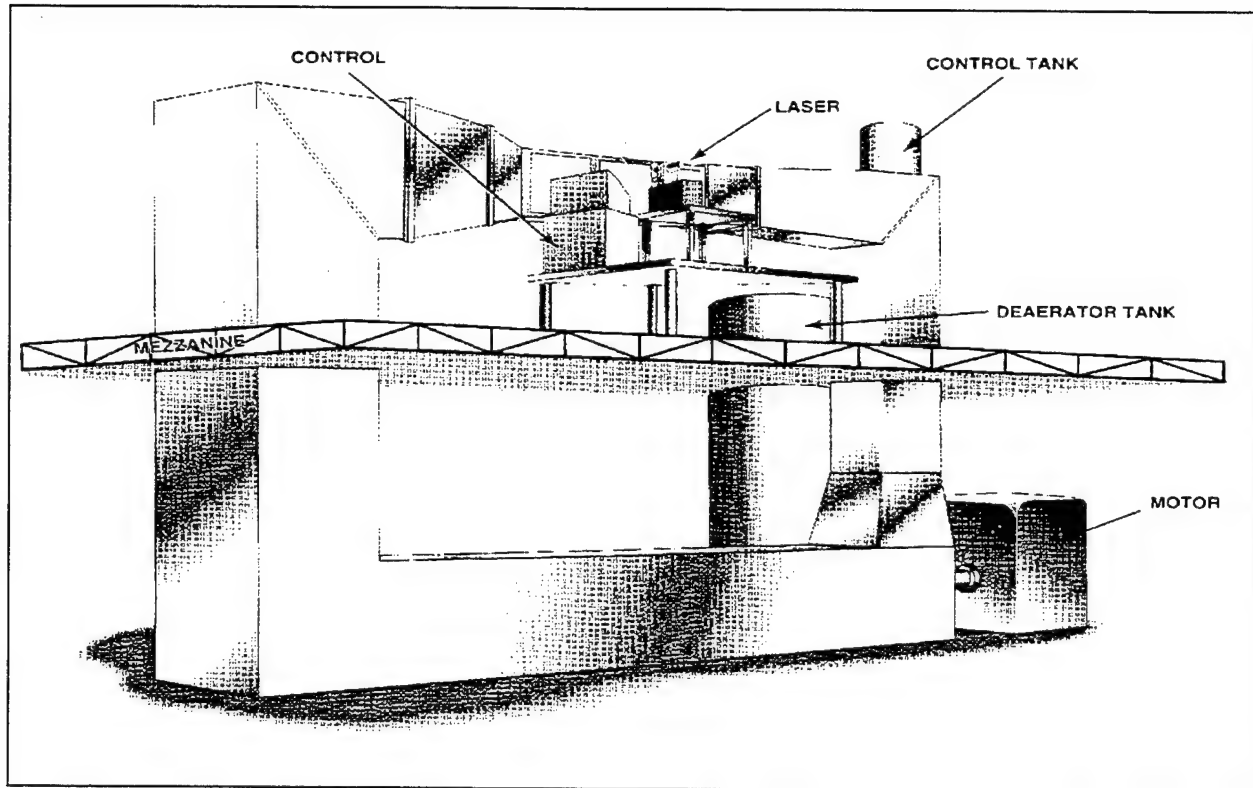


*Figure 1. NUWC's Sea Water Tunnel Facility*

The accuracy of the pressure control system is  $\pm 1.0$  psig. The flow circuit is designed for internal pressures ranging from -15 to +30 psig; the normal operating pressure is 20 psig.

Tunnel operation is monitored and controlled via a single instrument panel where tunnel speed, pressure, temperature, motor rpm, bypass flow parameters, and status lights are located. Throughout the MHD plate tests, consistent conductivity levels of the solution were maintained. Conductivity was measured using a YSI Model 35 conductance meter calibrated with a 0.1-siemen/meter conductivity standard. Water samples taken at the beginning and end of the testing were analyzed in the NUWC Chemistry Laboratory, where conductivity and salinity were measured to maintain calibration. Conductivity was found to be 2.66 siemens/meter at 22.45°C. Salinity was found to be 1.62% based on weight.

### **3.2.2 Test Apparatus**

**3.2.2.1 MHD Flat Plate.** The entire flat plate section consists of a 10-foot by 9-inch by 2-inch stainless steel flat plate with an elliptical leading edge and an adjustable fin on the trailing edge (figure 2). There are three 7-inch by 20-inch cutouts in the plate into which various test items may be inserted. The center insert, containing the modified MDTI MHD/drag balance assembly support material, had no effect on the active components of the plate. The front of the middle insert is located 43.5 inches from the leading edge of the flat plate. It was necessary to modify the external dimensions of the MDTI assembly so that it could fit in the cutout. This modification removed only excess support material and had no effect on the active components of the plate. A new set of platinum-coated niobium electrodes was installed before testing began so that the effects of salt water corrosion would be reduced.

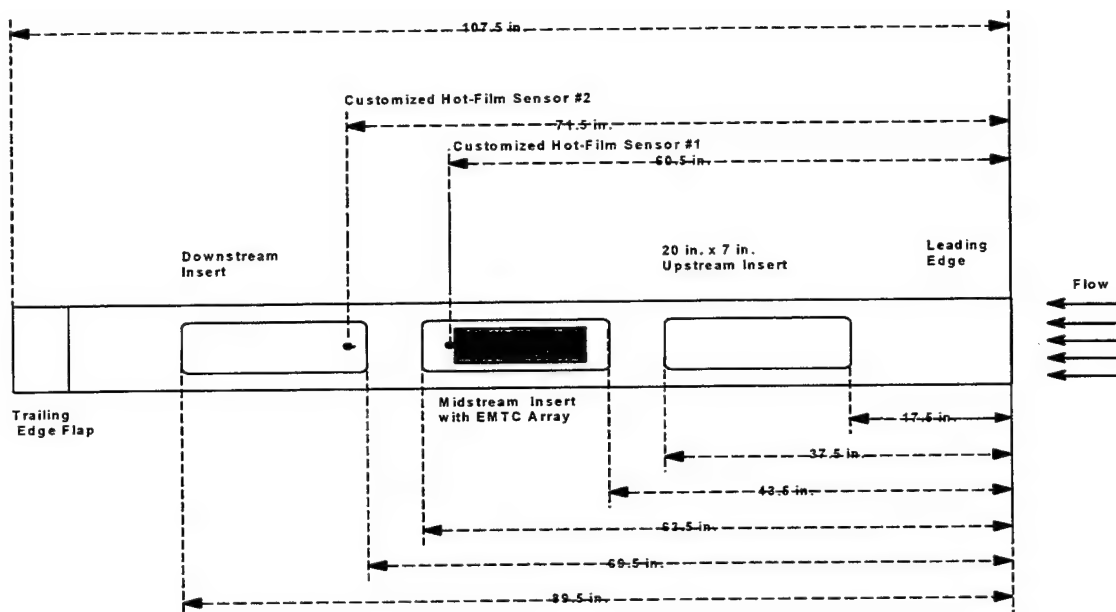


**Figure 2. MHD Flat Plate Test Bed Dimensions**

The MHD section consists of an array of magnets and electrodes secured to a stainless steel backing plate (figure 3). The array, comprising 64 cells, is configured with 16 alternating magnets (8 north and 8 south) oriented in the cross-stream direction. There are 128 electrodes arranged in 16 rows between the magnets, with 8 electrodes to the row. Each electrode is 0.3 inch x 0.2 inch with 0.5 inch between adjacent edges of electrodes in a row and 0.55 inch between rows, where the rows of electrodes are designated to be parallel to the magnets. This section was mounted into a piece of G-10 plastic. The entire section was designed to be inserted into flexure elements. Small (0.001-inch) gaps were present in the front, back, and sides of the insert, so that the floating section could deform the flexure elements.

**3.2.2.2 Electrode Pulsing Controller.** An electrode controller was designed and assembled for use in this series of tests. The controller powers up to 32 independent electrodes at any instant. Frequency and duty cycle are controlled by a PC host, and communication between the PC host and controller hardware is via a two-way RS422 (38.4-kbaud) link. Either unipolar or bipolar electrode voltage waveforms are available. The frequency is adjustable between 2 and 1000 Hz (range can be increased), and the duty cycle is adjustable but was set to 25% for the NUWC tests. The power switching devices (metal oxide semiconductor field effect transistors (MOSFETs)) are rated to 100 volts and 30 amps.



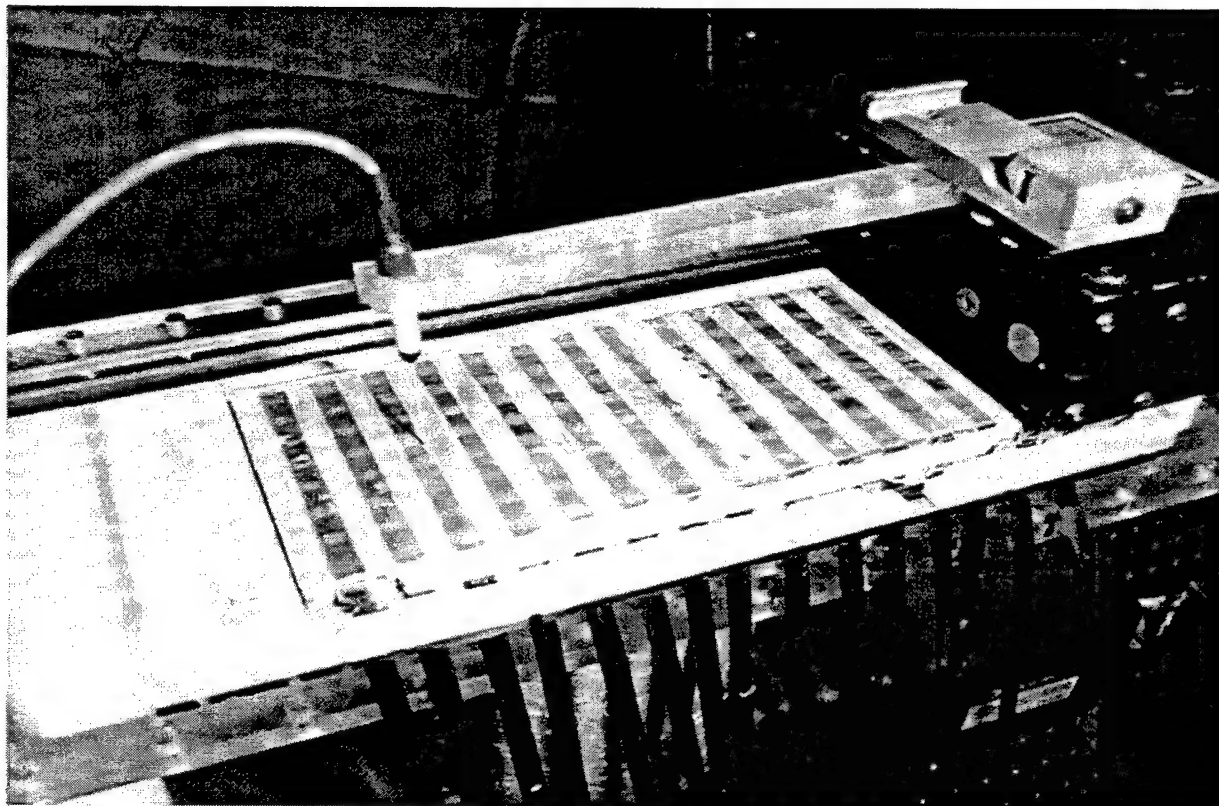


*Figure 3. MDTI Plate Situated in Floating Element Force Balance*

Additional controller features not used during this series of tests include RMS measurement and display of applied voltage and current waveforms, peak voltage and current measurement and display, potential for increasing the number of independent electrodes, and host data logging of all system parameters with feedback to hard drive data file for posttest processing.

The controller is made up of several subsystems as shown in figure 4. The main central processing unit (CPU) board contains an Intel 80C196KD (20 MHz) microcontroller that maintains an RS422 communication link with a host IBM-compatible PC. The controller also commands the switching sequences sent to the electrode power switching circuitry via a digital interface board. The digital interface board latches the switching sequence output from the CPU and holds these values constant until the CPU sends it the next switch sequence. The latched output of the digital interface board is input directly to the two power boards.

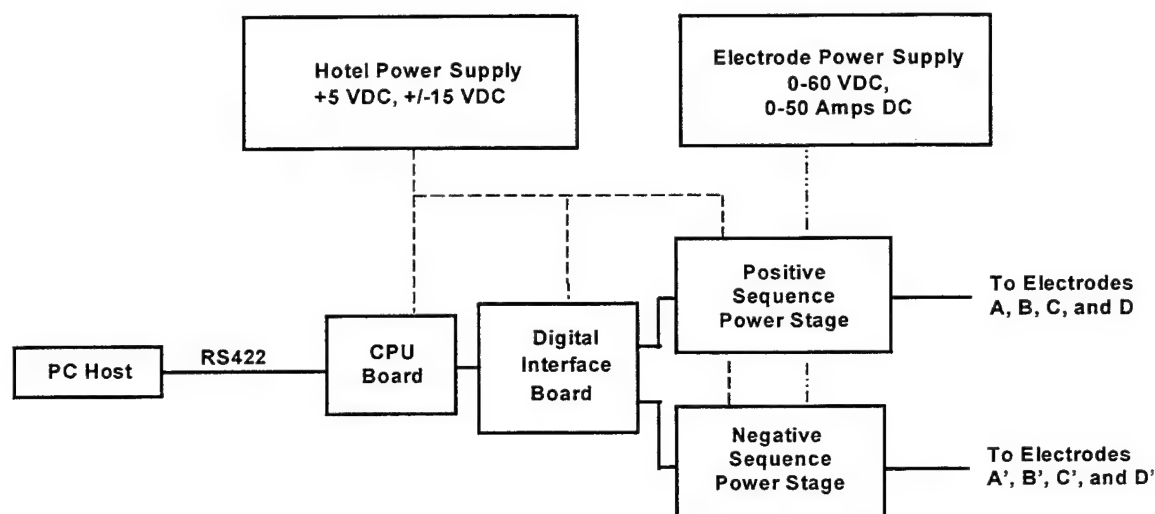


**Figure 4. Electrode Controller Block Diagram**

The switching sequences are fixed for a given set of tests, but frequency, voltage, and current can be regulated via the host or electrode power supply. The microcontroller code is written in C programming language, compiled, and programmed onto an EPROM (electrically programmable read only memory) located on the CPU board. To regulate the control sequence, the CPU maintains a variable-period internal frame rate. All internal calculations and control are synchronized to this frame and repeated every frame. The frame period, downloaded from the host PC, dictates the frequency or rate at which the switching sequence is to change.

The desired voltage waveforms between adjacent electrode pairs in a cell are illustrated in figure 5, which shows the potential that is applied across adjacent electrode pairs at times  $t = 0, 1, 2, 3, \dots$ . The waveforms repeat once every four fundamental time periods.

The CPU cycles through four separate states to generate the desired electrode voltages. The CPU does so by stepping through the sequence of four stored states at a rate of once per frame. Therefore, to generate the waveforms shown in figure 5 at 1 kHz, the CPU's frame rate is set at four times the desired frequency or 4 kHz.

Figure 6 shows a half-section of the physical layout of the MHD plate. The locations of electrodes A through D' are shown with respect to the magnets. The polarity of the electrodes during the four sequences is shown in each electrode block. A "+" indicates that the electrode is connected to the electrode power supply's positive output lead, and a "-" indicates that the electrode is connected to the power supply's output ground lead. A "0" indicates that the electrode is floating, i.e., it is not connected to either of the power supply leads. All electrodes with the same designator are tied together and powered in parallel from the same channel of the power stage. The individual cells located between adjacent electrode pairs (e.g., A and B) are drawn as parallel resistors in figure 7.



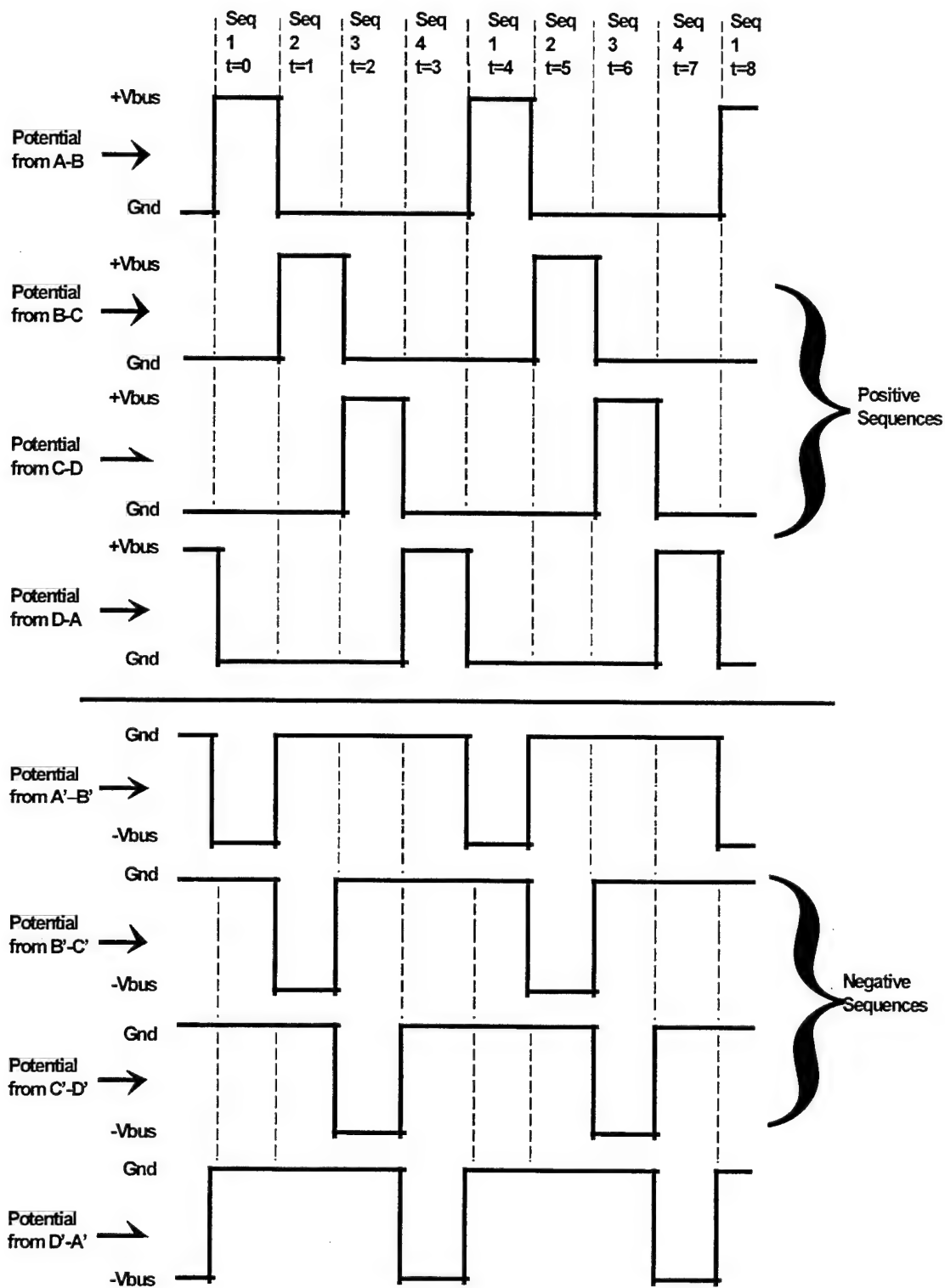
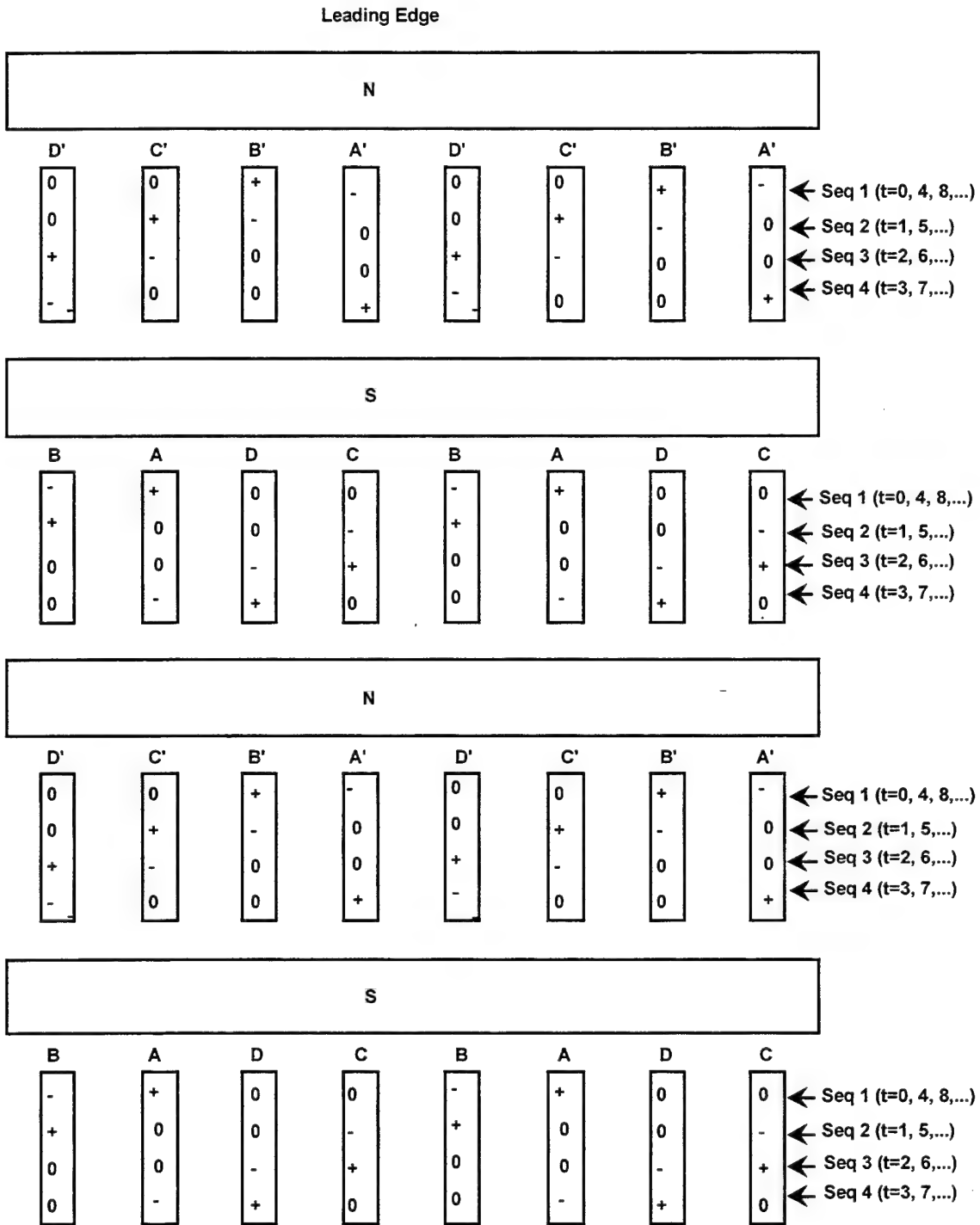
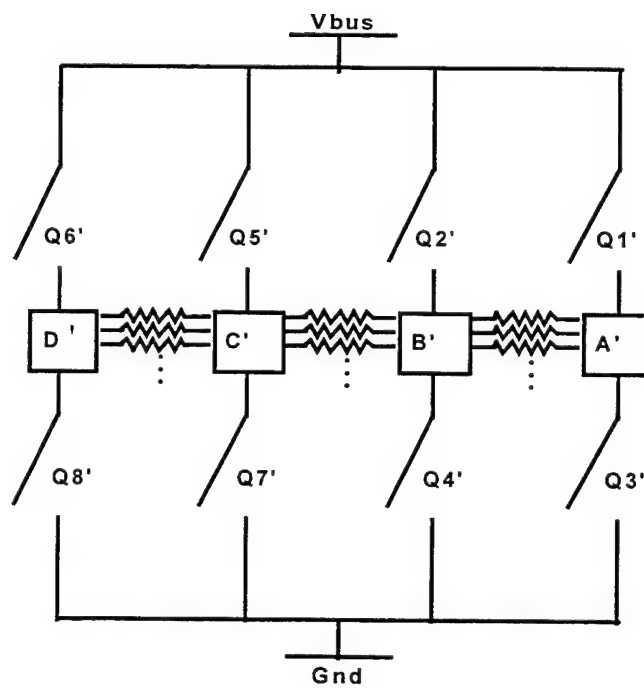
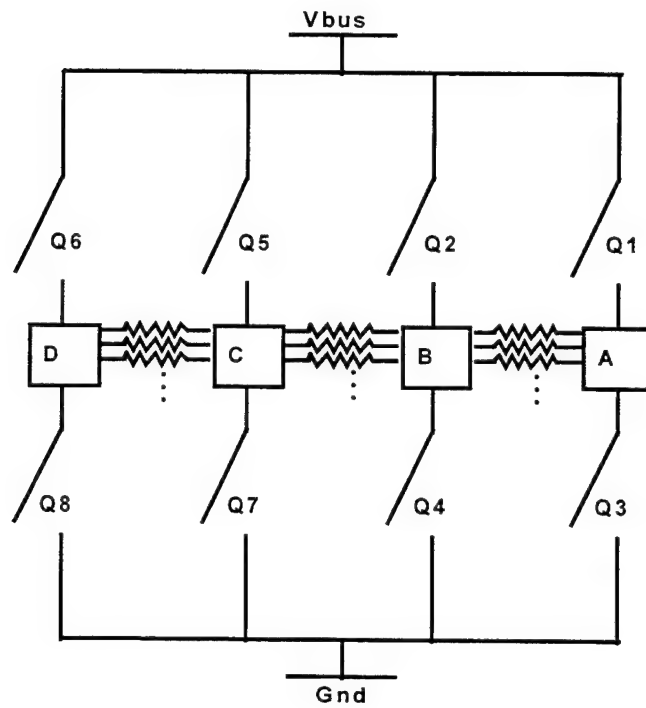


Figure 5. Desired Electrode Switching Waveforms (Ideal)



**Figure 6. Plate Layout and Corresponding Electrode Sequencing**



*Figure 7. MOSFET Power Stage*

At time = 0, 4, or 8, figure 5 shows that sequence 1 is enforced and current flow is from electrodes A to B and electrodes B' to A'. Electrodes A and B' are connected to the electrode power supply's positive output lead by closing switches Q1 and Q2' (see figure 7). Electrodes B and A' are connected to the electrode power supply's ground output lead by closing switches Q4 and Q3'. These switches are power MOSFETs (metal oxide semiconductor field effect transistors). The current magnitude supplied to the electrodes can be controlled by adjusting the output of the electrode power supply, referred to as Vbus in figures 5 and 7.

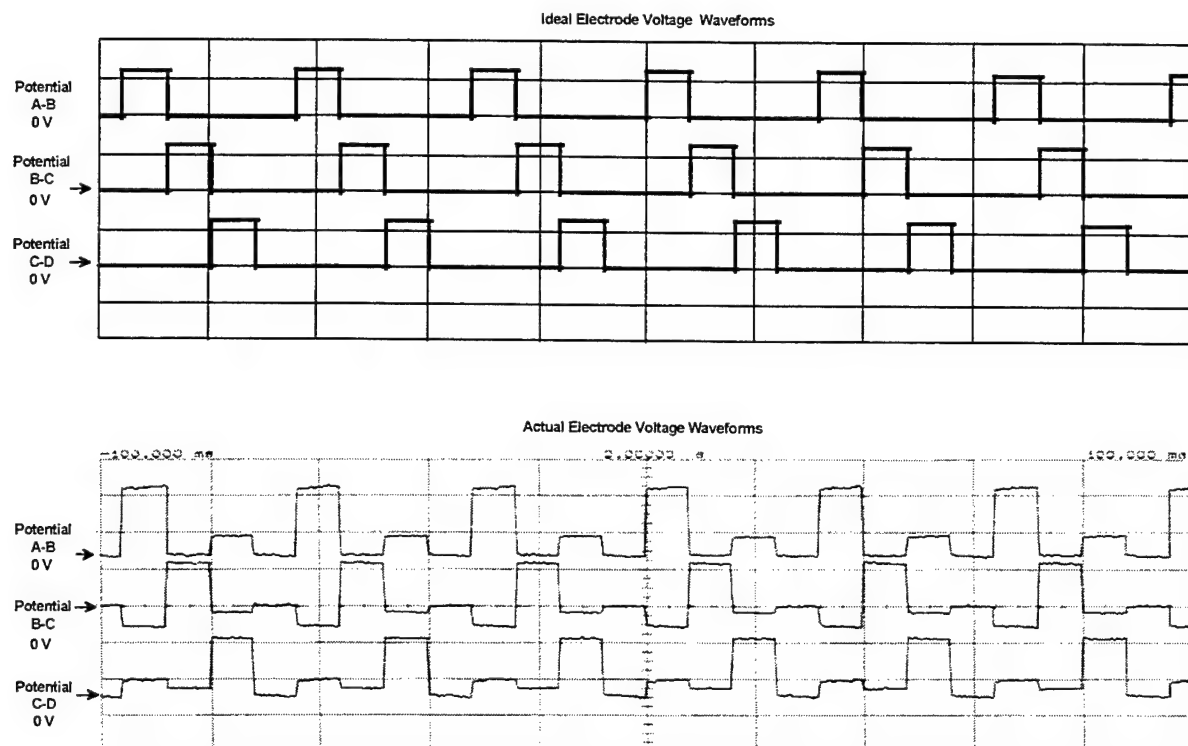
Figure 6 also indicates that current into electrodes A through D will be negative 25% of the time, then positive 25%, and 0 for the remaining 50%. A representative plot of the current waveform from the MHD plate's electrode A bundle is given in figure 8, with ideal current flow shown as well. These data were obtained using a Tektronix Model 503 hall effect current probe. The peak current was approximately 4.75 amps for an applied voltage of 17 volts. Figure 9 shows a plot of a current waveform from a single electrode. The peak current and voltage for the single electrode was found to be approximately 350 mA and 17 volts. Notice that the current is first positive then negative as compared to the previous plot.

Figure 10 is a plot of the voltages across three adjacent electrode bundles, with ideal voltages shown for comparison. Ideally, one wishes that the electrical current would flow only between adjacent electrodes. The deviation from the ideal case is due to currents straying to the next nearest electrodes. In sequence one, for example, current is desired from electrode A to adjacent electrode B. In reality, current will also flow to the next B electrode located three electrodes away in the same row. So, current flows across cells connected between A and D, D and C, and C and B, producing voltages that are opposite in polarity and one-third in magnitude across unenergized cells. To complicate this issue further, current also flows from electrode A to electrodes A', which are in fairly close proximity and connected to ground during this sequence, along with other B electrodes located in other rows.

At the end of the test matrix severe degradation in electrode performance was observed. Posttest diagnostics were performed to confirm that the controller was performing as designed and that the electrodes degraded rapidly near the end of the tests. During a posttest analysis, it was found that the current delivered by the dc power supply and into the electrode bundles decreased by a factor of two. This current drop indicated an increase in inter-electrode resistance. Since the conducting medium had not changed, this drop was attributed to an increase in electrode surface resistance. Continued testing caused the electrodes to degrade further. Figure 11 illustrates the current waveforms obtained during the final diagnostic tests along with a plot of the current waveforms with the power supply connected to a resistor load bank. The waveforms were significantly distorted and were about 1/50 the amplitude of those presented in figure 8. Figure 12 shows the time history of the degradation process. By the time repeat tests took place, electrode impedance was approximately twice the initial value. By the end of the test, the electrodes were effectively nonfunctional.

### **3.2.3 Visualization of Lorentz Pressure Pulsing**

A large increase in resistance (about a factor of 2) between electrodes was observed near the end of the testing in the water tunnel. To ascertain proper phased pulsing of the MHD electrodes, after completion of the NUWC test series, a visualization was conducted using the controller in a salt water tank. Ideally, the negative and positive voltages should be equal, which would then produce uniform bubble formation over all the electrodes. At low voltages, however, it was found that bubble formation over the electrodes was not uniform. Electrical currents from specific electrodes showed that the magnitude of negative current on a given switching sequence was not equal to the magnitude of the positive current at the same electrode on the following sequence. Asymmetry exists only at less than 10 Hz and therefore is irrelevant to the test objective. There is a threshold voltage (~30 volts) above which all electrodes have a similar



**Figure 8. Ideal and Actual Electrode Voltage Waveforms from a Bundle of Electrodes**

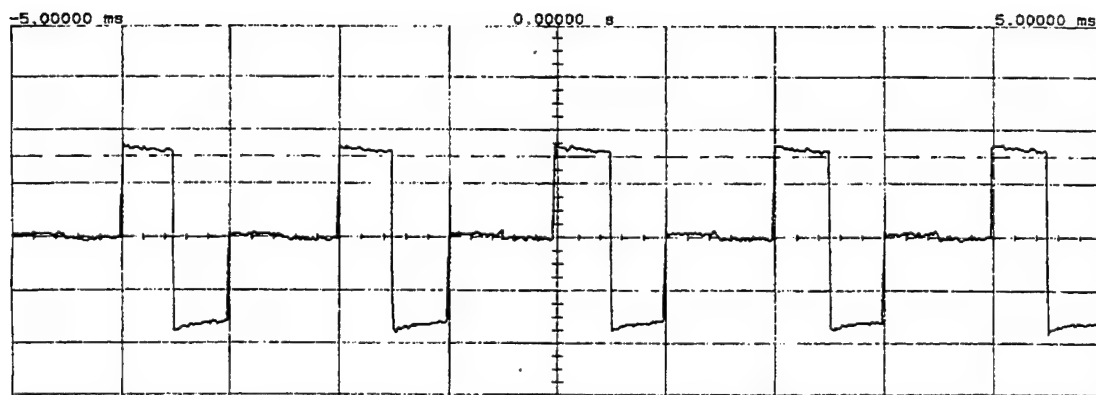


**Figure 9. Actual Electrode Current Waveforms Taken from a Single Electrode**

appearance. Below this threshold, different groups of electrodes have different characteristics. At low voltages, electrodes on the edges of the array behave in a different manner than the central electrodes. This difference in current magnitude and subsequent uneven bubble formation is hypothesized to be due to the presence of cross stray currents that modify the current waveforms. Recorded video images of the plate over a range of frequencies and voltages showed that the controller and MHD plate were operating as designed during the early tests until an

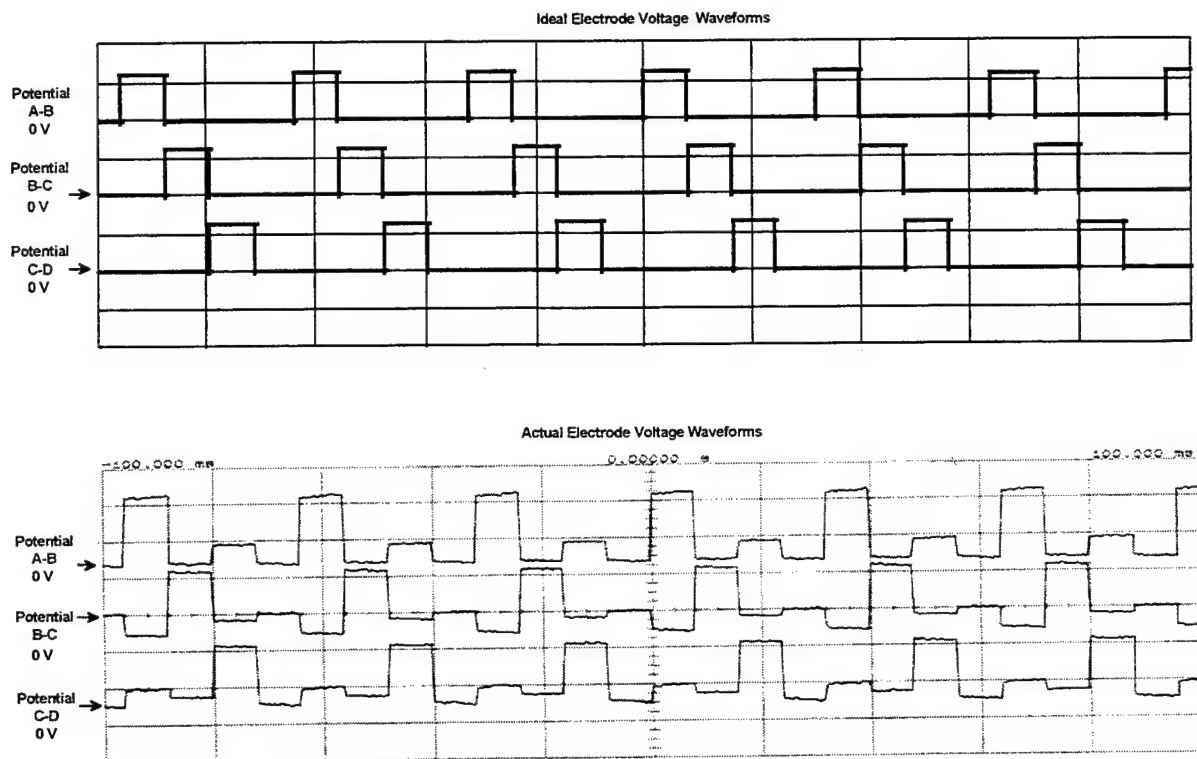


**Figure 10. Ideal and Actual Electrode Voltage Waveforms Taken from a Single Electrode**

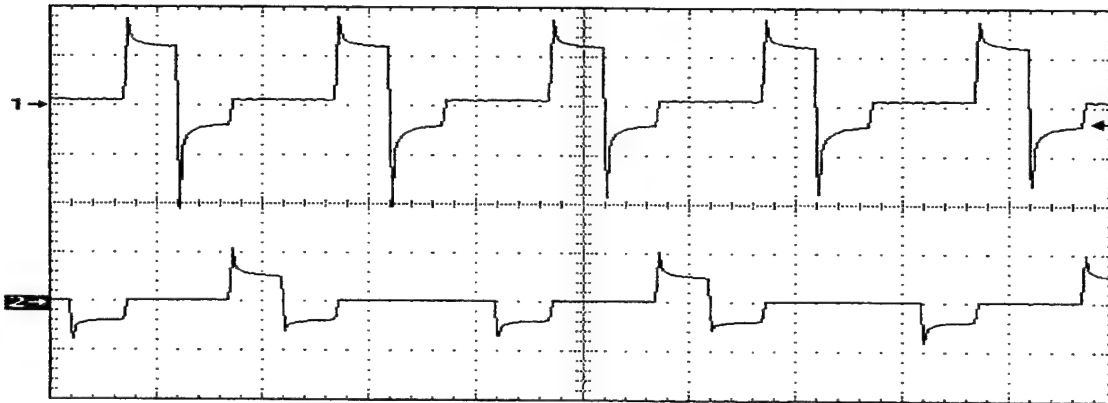
observed increase in resistance during the last day of testing. Such investigation continued until a massive short to sea water at one or more of the connections to the electrode ribbon cables. The resistance of the electrode system had then increased further, so that the current was only 1-2 amps at 30 volts.

The observations made suggest that the controller was performing within its designed range of operation for frequencies  $\geq 10$  Hz and for voltages  $> 7$  volts. The anomalous appearance of the electrodes is attributed to corrosion of the electrodes or connectors. It may also be attributable to differences in stray current patterns for edge electrodes. The controller does not operate correctly at frequencies  $< 10$  Hz because of limitations of the controller architecture.

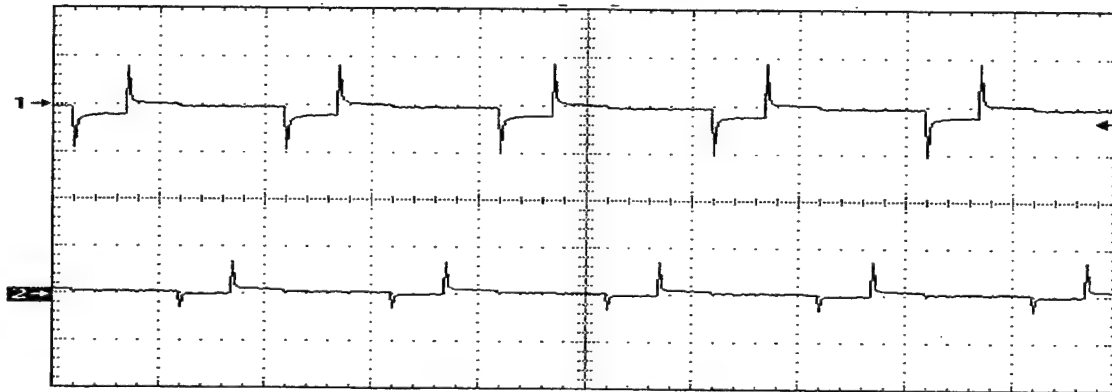
### 3.2.4 Instrumentation

Past difficulties in hot-film analysis include persistent, large spanwise variability in the fractional skin friction reduction  $\Delta \tau_w / \tau_w$  measured by the hot-film sensors. Because of this variability, inferring the total drag reduction from local shear stress measurement becomes highly questionable. For this reason, a force balance is used to measure global drag, so that if total drag reduction is realized, it will be measured directly. A related question is persistence of the drag reduction. If local drag reduction is measured, downstream persistence of the effect needs to be determined. In the NUWC test series, two hot-film sensors were placed in the streamwise direction; the first was located just downstream of the MHD array; the second, 11 inches downstream from the first (see figure 3). This arrangement allowed measurements of local and global drag reduction and of the downstream persistence of the effect.

**Deteriorated Electrode Bundle Input Current**  
(30 V, 10 Hz, 1 A/div)



**Deteriorated Electrode Bundle Input Current**  
(20 V, 10 Hz, 0.5 A/div)



**Resistive Load Input Current**  
(20 V, 10 Hz, 1 A/div)

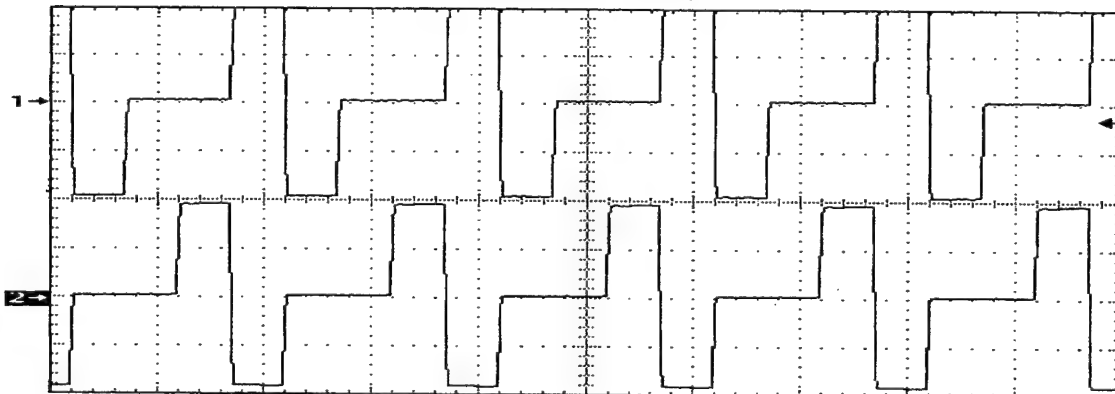


**Figure 11. Degraded Electrode Diagnostic Waveforms**

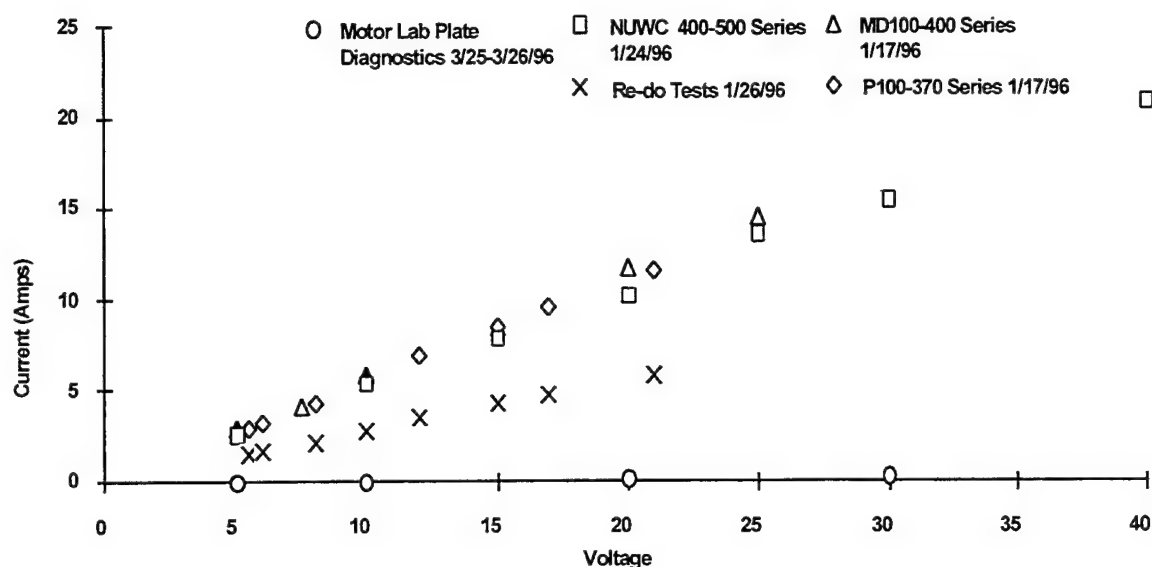


**Figure 12. Electrode Degradation Over Time in Salt Water**

**3.2.4.1 Force Balance.** A skin friction force balance was designed and fabricated to provide accurate measurements of spatially integrated shear stress. A schematic of the floating element skin friction balance employed during this test is shown in figure 13. The balance design incorporates a floating surface element held in place by four flexures, which are in turn cantilevered from the flat plate housing. The design is driven by the desire to have very narrow gaps between the floating element and the stationary flat plate over which the fluid flows. These narrow gaps require stiff flexures to minimize the displacement of the floating element when a shear stress is applied. The small gap dimensions reduce flow through the gaps, which would generate erroneous drag information. Gap-induced drag measurement errors can be further reduced by knife-edging the perimeter along both sides of the gap. Stiff flexures also increase the resonant frequency of the balance, providing for a higher quality signal for the sensing element (the strain gauge).

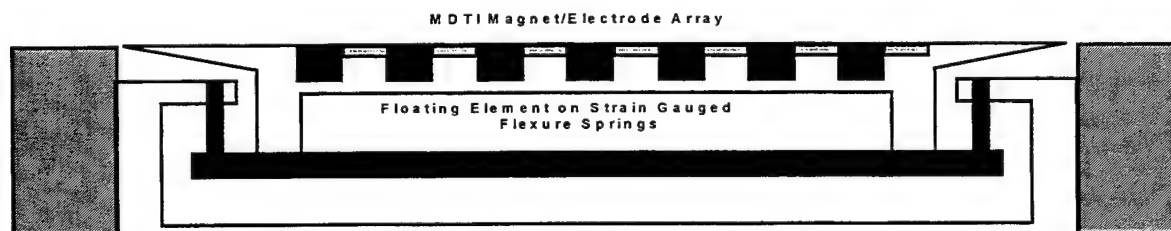


**Figure 13. Floating Element Force Balance**



The flexure design provides a straightforward linear relationship between the applied shear loading on the floating element and the amount of strain generated in the flexure. Once the material properties (i.e., Young's Modulus  $E$  and yield stress) and the physical dimensions (i.e., height  $l$ , width  $w$ , and thickness  $t$ ) are known, the horizontal or streamwise displacement  $Y$  of the floating element caused by a horizontal force  $F$  is given by

$$Y = (F / wE) * (l / t)^3 = (F * l^3) / (12 * E * I),$$

where  $I$  is the moment of inertia.  $Y$  is easily seen to be a linear function of the applied load  $F$ . This displacement is shown schematically in figure 14.

The bending stress  $\sigma_b$  in the flexure is also a linear function of the applied load and the vertical distance  $x$  along the flexure:

$$\sigma_b = 6(F / wt^2) * (x - l / 2),$$

thereby demonstrating that the maximum bending stresses occur at the ends of the flexure. There is no bending stress at the center of the flexure (i.e.,  $l/2$ ). If the flexure deformation is assumed to be elastic, the strain is proportional to the stress by

$$\varepsilon = \sigma / E$$

where  $\varepsilon$  is the dimensionless strain caused by the applied stress. The design optimization for this flexure concept centers around minimizing the displacement of the floating element while maintaining a sufficient amount of strain in the flexures for an accurate measurement to be possible.

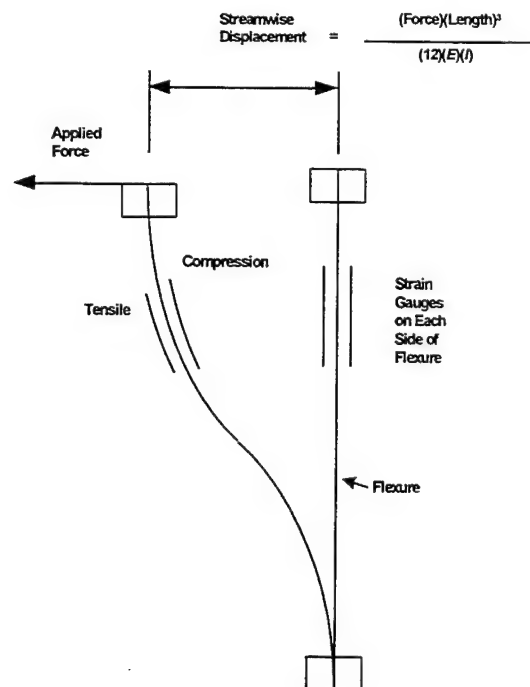


**Figure 14. Flexure Element Design**

A general rule of thumb for strain gauge measurements is that a range of 0 to 1000  $\mu\epsilon$  (microstrain) be generated for good signal-to-noise properties. The hardware employed for these experiments generated a maximum strain of 500  $\mu\epsilon$  at 9.8 newtons (1 kgf), which allowed for a maximum horizontal balance deflection of 1 mm.

The in-situ, wet calibration procedure consisted of positioning the balance hardware in the flat plate cavity, rigging all the wiring as needed, and submerging the entire apparatus under 1 inch of water. This procedure allowed for a pulley and string arrangement to be employed in a manner identical to the dry calibration procedure. These calibrations demonstrated that the ancillary wires needed to activate the electrodes and monitor a flush-mounted hot-film sensor did influence the response of the floating element. Balance calibrations were repeated often to update any changes in the balance response due to wiring movements or deflections. A sample calibration curve is shown in figure 15. In this case, the calibration was conducted in water to account for any fluid effects.

Furthermore, the time-dependent properties of the floating element were also measured in-situ, with the balance hardware submerged at a depth of 1 inch. A shaker device was then bolted to the floating element; this device would oscillate a known weight at controlled frequencies and amplitudes. Accelerometers were used to monitor the shaker and the floating element displacements in both the horizontal and vertical planes. The vertical motion of the balance proved to be insignificant, as would be expected by design. However, the streamwise component demonstrated that the balance had a resonance frequency of roughly 15 Hz, with a sharp dropoff in sensitivity (-20 dB dropoff at 40 Hz), as shown in figure 16. This finding shows that, unless

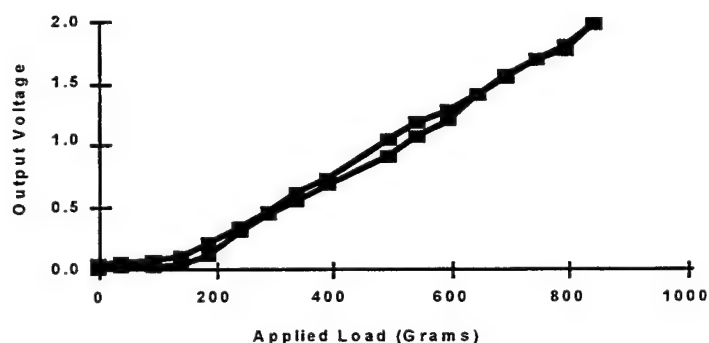


**Figure 15. Static Force Balance Calibration Curve**

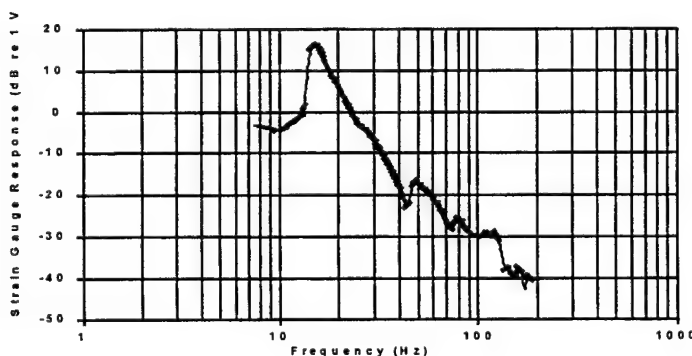


**Figure 16. Force Balance Dynamic Response**

the “resonance frequency” of the MHD effect is near 15 Hz, the force balance will not introduce any aberrations. These data also indicate that it is not feasible to use this balance to resolve the small scales that occur at high frequencies in the turbulent flow.

**3.2.4.2. Hot Films.** Surface-mounted hot-film sensors were used to measure the wall shear stress produced by turbulent flow over the flat plate. An important indicator of turbulent drag reduction, these sensors provided data on the wall shear stress reduction produced by the MHD element.

In the past, difficulties have been experienced with hot-film sensors in a sea water environment in the presence of an electric field. The electrical resistance of hot-film sensors has been seen to drop from 10 ohms before sea water testing to 1 ohm after testing, indicating the presence of a minute current path caused by the breakdown of the quartz coating and rendering the measurement data questionable. For this reason, customized hot-film sensors were manufactured by TSI specifically for the NUWC tests. Figure 17 shows a sketch of a standard hot-film sensor and a customized sensor. The customized sensor has a double quartz coating and a shielded coaxial cable. The shielded cable minimizes grounding problems and pickup of stray currents in the conducting medium. Figure 18 shows the customized hot-film sensor’s frequency response, which was measured in a standard square wave test. The frequency response of the

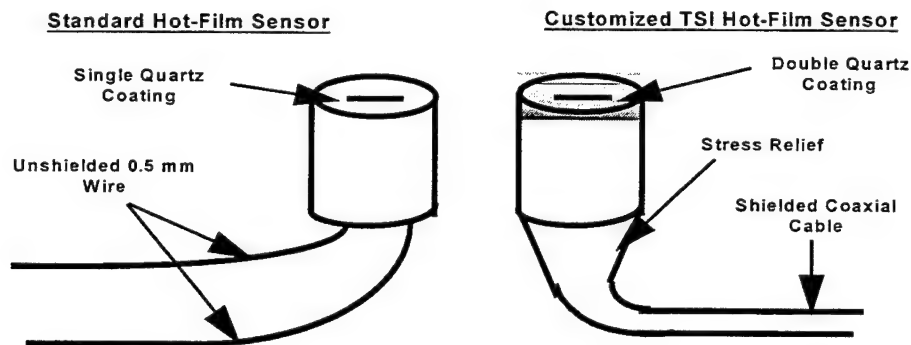


**Figure 17. Standard and Customized Hot-Film Sensors**

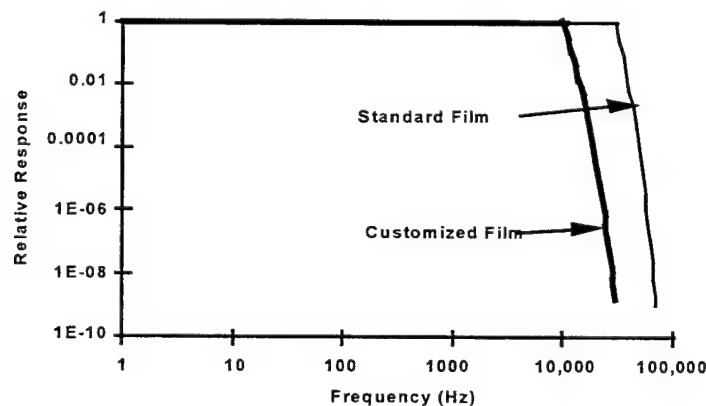


**Figure 18. Frequency Response of Customized Hot-Film Sensor**

customized hot-film sensor was flat out to 10 kHz, while the response of a standard, single-coated sensor is generally flat out to 30 kHz (depending on the resistance of the sensor). However, this difference is considered acceptable to trade off against the benefit of minimizing stray current effects due to film exposure.

To further extend the life of the hot-film sensors, the MHD array and hot film were operated simultaneously as little as possible; in other words, the MHD array was turned on only during the data recording. The data acquisition process is shown schematically in figure 19. The two TSI hot-film sensors were connected to a constant-temperature bridge circuit built by TSI Inc. Hot-film signals were recorded at various sampling frequencies and lowpass-filtered to prevent aliasing of the signal. Hot-film data were collected as follows:

<u>Flow Speed (meters/second)</u>	<u>Data Collected At</u>
Less than 1.4	500 Hz for 20 seconds
Between 1.8 and 2.5	1000 Hz for 10 seconds
Between 2.6 and 3.4	2000 Hz for 5 seconds
Greater than 3.4	5000 Hz for 4 seconds

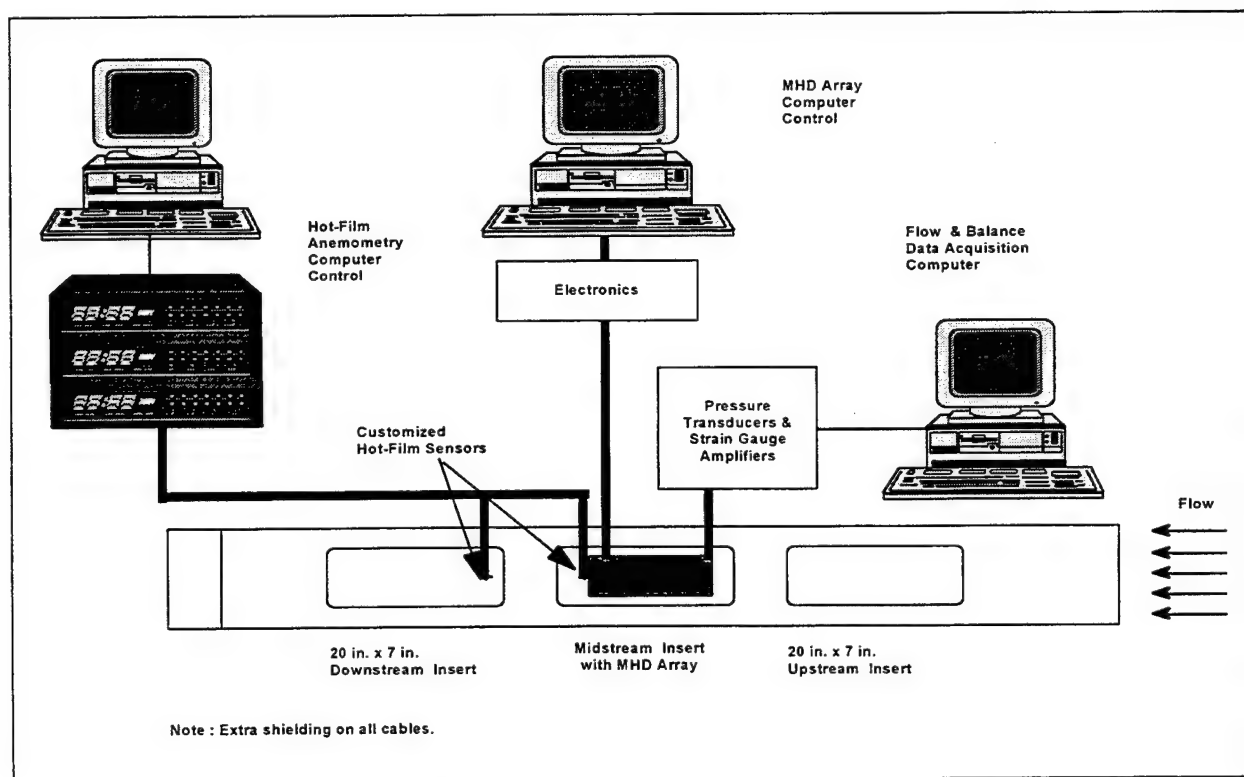


*Figure 19. Instrumentation Schematic*

Recently, Nosenchuck and his team at Princeton University experienced additional problems with TSI hot-film sensors. They found that the sensor's constant temperature is noisy and difficult to control, and that the ac power is noisy, which can cause current surges, creating significant local heating and minute cracks in the film coating. They made two changes to ensure that there was no degradation of the hot-film probe signal to noise ratio (the gain ratio is on the order of 50). First, they replaced the hot-film constant-temperature driver with a constant-current driver. Second, they used a dc battery for electrical power, so that the sensor was isolated from the ac power line.

Force balance and pressure transducer output were connected to a separate computer, sampled at 200 Hz, and lowpass filtered at 100 Hz. The MHD array was operated by a separate power supply and computer. Isolation of the instrumentation and MHD electrodes minimized cross-talk between the various electrical devices. To further minimize corruption of the collected data, all instrumentation and MHD cables were shielded by wrapping the cables in aluminum foil and grounding them.

High-frequency data from all sensors before the signal conditioner were recorded to allow reconstruction of the probability density function (PDF) for  $\tau_w$ . (High frequency is defined as the maximum of the two frequencies  $\{u_\tau^2/\nu, 5U_\infty/\delta\}$ ; the Nyquist frequency is twice this frequency.) The PDF obtained with MHD on and off could then be compared. It was expected that with MHD on the PDF ( $\tau_w$ ) would be shifted to a lower mean value of  $\tau_w$  and that the distribution would be narrower, i.e., it would have a smaller variance, indicating the reduced variability of  $\tau_w$ .

### 3.3 EXPERIMENTAL TEST CONDITIONS

Table 1 gives an overview of test conditions for the experiments conducted by Princeton (Nosenchuck and Brown, 1993-1995), MDTI, and NUWC. In the NUWC tests, every effort was made to duplicate the Princeton and MDTI test conditions, so that the experimental results could be fairly compared. Differences in the test facilities and test media do exist; but, for the most part, test conditions were substantially replicated.

For the NUWC tests, the use of a salt water (1.6% sodium chloride) medium resulted in a fluid electrical conductivity that was approximately twice as large as that in the MDTI tests and about four times as large as that in the Princeton tests.

Differences in Reynolds number are also shown in table 1. The MHD plate was located approximately 1.3 meters downstream of the leading edge of the flat plate in the NUWC tests but only 0.7 meter downstream in the MDTI and Princeton tests. This difference yields a Reynolds number for the NUWC tests twice as large as that in the Princeton and MDTI tests.

**Table 1. Summary of Test Conditions**

	<b>Princeton Tests</b>	<b>MDTI Tests</b>	<b>NUWC Tests</b>
Test Facility	Princeton flow loop (10 in. x 10 in. x 3 ft)	NRad water tunnel (12-in. open jet)	NUWC water tunnel (12 in. x 12 in. x 9 ft)
Medium	0.4% NaOH	0.8% NaOH	1.6% NaCl
Conductivity (mmhos/cm)	7.5	15	26.6
Pressure Gradient	Unknown	Unknown	3% of freestream
Flow State (Laminar/Turbulent)	Unknown	Turbulent	Turbulent
Test Velocity (m/s)	0.1-3.7	1.0-5.0	1.0-5.0
Reynolds Number	0.08-3.0 E+6	0.75-3.8 E+6	1.38-6.8 E+6
Frequency Range (Hz)	2-500	30-120	30-850
Voltage Range (V)	5.5-21	7.5-25	5.0-40
Current/Electrode (mA)	110-430	150-500	100-850
Test Hardware	MDTI plate, MDTI controller, stainless steel electrodes	MDTI Plate, MDTI controller, stainless steel electrodes	MDTI Plate, NUWC controller, platinum electrodes
Cable Shielding	Unknown	None	All cables shielded
Instrumentation	Hot-film sensors and flow visualization	Hot-film sensors, LDV, and load cell	Customized hot-film sensors, flow visualization, and flexure balance

The magnitude of the pressure gradient was monitored during the NUWC tests. A favorable pressure gradient of approximately 3% of freestream dynamic pressure was present over the MHD plate section. In other words, freestream dynamic pressure decreased by 3% from the leading edge to the trailing edge of the MHD plate. Information regarding the magnitude of the pressure gradient in the Princeton and MDTI tests is unavailable.

All tests at NUWC were conducted in a turbulent boundary tripped at the leading edge. Baseline, MHD-off, hot-film analysis of the NUWC test series clearly demonstrated (as will be shown later) that a fully developed turbulent boundary layer was established over the MHD plate for all test conditions examined. It is not known whether the tests conducted at Princeton and MDTI were carried out in a fully developed turbulent boundary layer.

### 3.3.1 MDTI/Princeton Test Matrices

In the MDTI and Princeton test matrixes (see appendix tables A-1 and A-2), files ending in an odd number were baseline tests in which MHD was off; these tests were run immediately prior to MHD-on tests, whose file names end in an even number. The controller was set at the voltage specified in the tables given in the appendix. The electrode's electrical current listed in the tables should be considered approximate. The MHD electrode array was pulsed at the frequency specified in the pattern described earlier.  $V_{bubble}$  is the bubble threshold voltage based on the input frequency;  $f_{bubble}$  is the bubble threshold frequency (in Hz) based on the input electrode voltage. To avoid bubble production,  $V_{bubble}$  must remain above the applied voltage and  $f_{bubble}$  must remain below the array pulsing frequency. If either of these conditions is not satisfied, bubble production is likely. The importance of bubble production is its effect on hot-film sensor performance. Huyer (1995) demonstrated that bubble advection over hot films resulted in bubble accumulation on the hot film. This bubble accumulation effectively decreases the heat transfer rate of the hot film, resulting in a false reading of reduced turbulence and reduced drag. Although the hot-film sensors were positioned out of the bubble wake, stray bubbles may still have affected their performance. Tables A-1 and A-2 in the appendix also show the voltage and frequency bubble thresholds.

### 3.3.2 NUWC Test Matrix

An analysis was performed on raw hot-film signals to characterize the dominant frequencies from the turbulent velocity data for flow velocities of 4.0 and 5.0 meters/second. This analysis was carried out to select appropriate MHD pulsing frequencies for the NUWC tests. Figure 20 shows a typical time-dependent trace of a raw hot-film signal at a 1-meter/second flow speed. The event periods are defined as follows:

- *Microturbulent Ejection Period ( $T_e$ )* - This event has the shortest duration of all microturbulent events and therefore occurs at the highest frequency. As the local turbulent boundary layer undergoes an ejection event, an increase in hot-film data fluctuation is observed.
- *Burst Duration ( $T_p$ )* - The period during which many high-frequency ejection and sweep events occur is called the burst duration. Hypothetically, to reduce drag, MHD control should be applied only during this period.
- *Time Between Bursts ( $T_B$ )* - The relaxation phase when few surface velocity fluctuations are observed is called the time between bursts. During this interval, the flow sustains the quasi-stable low-speed streaks with low skin friction and therefore does not require application of MHD pressure.

It is believed that the ratio of  $T_e/T_B$  to  $T_p/T_B$  can be an effective indicator of the required MHD duty cycle. As an example, experimental observations of  $T_e$ ,  $T_p$ , and  $T_B$  are provided below:

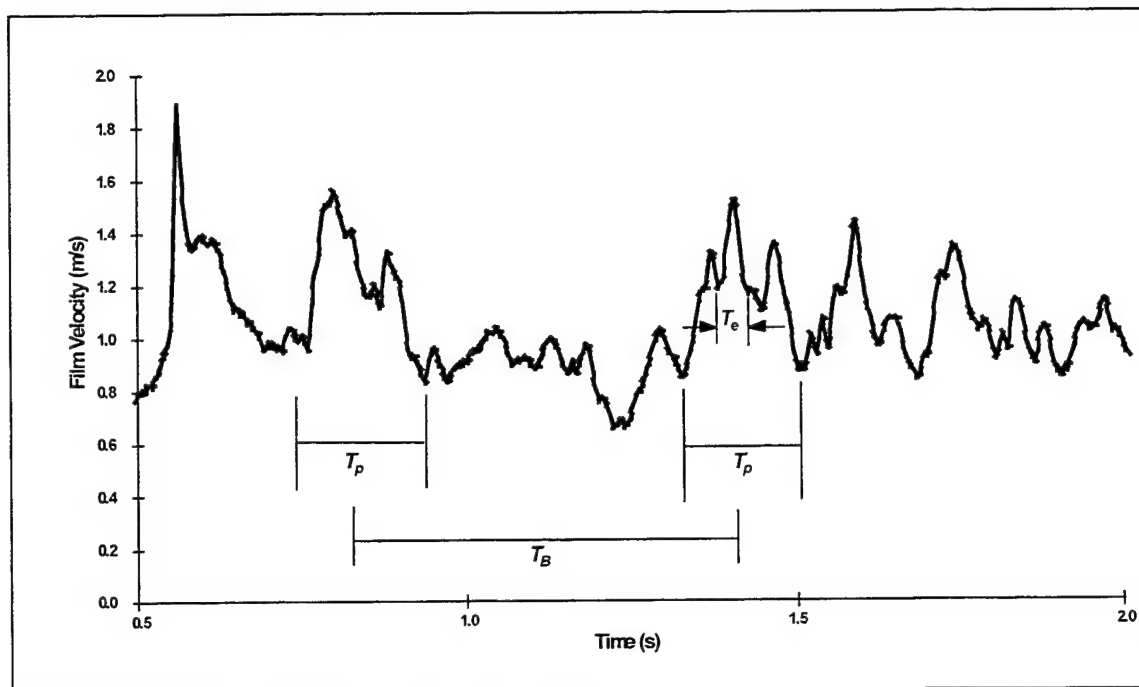


**Figure 20. Typical Trace of a Hot-Film Signal, Illustrating Relevant Turbulent Time Scales at 1-Meter/Second Freestream Velocity**

At flow velocity = 4 meters/second:

$$T_e = 1.5\text{-}2.5 \text{ msec}, f_e = 400\text{-}670 \text{ Hz}, T_p = 12\text{-}16 \text{ msec}, f_p = 60\text{-}85 \text{ Hz}, \\ T_B = 30\text{-}60 \text{ msec}, f_B = 15\text{-}35 \text{ Hz}, T_e/T_B \cong 5\%, T_p/T_B \cong 26\text{-}40\%.$$

At flow velocity = 5 meters/second:

$$T_e = 1.2\text{-}1.8 \text{ msec}, f_e = 550\text{-}850 \text{ Hz}, T_p = 10\text{-}12 \text{ msec}, f_p = 80\text{-}100 \text{ Hz}, \\ T_B = 22.5\text{-}45 \text{ msec}, f_B = 20\text{-}45 \text{ Hz}, T_e/T_B \cong 5\%, T_p/T_B \cong 26\text{-}40\%.$$



## 4. DATA ANALYSIS AND RESULTS

### 4.1 TIME-AVERAGED RESULTS

Time average and standard deviation values were computed for both force balance and hot-film data over the duration of the entire run. The skin friction coefficient was then computed based on the force measurements using

$$c_f = 2F / (\rho u_e^2 A),$$

where  $\rho$  is the fluid density (1000 kg/meter<sup>3</sup>),  $u_e$  is the boundary layer edge velocity,  $A$  is the area of the flat plate (0.09 meter<sup>2</sup>), and  $F$  is the total force obtained from balance measurements.

The skin friction velocity and skin friction coefficient were computed from the hot-film data. The skin friction velocity was computed as

$$u_\tau = \left[ 0.0296 (Re_x)^{-0.2} u_{film}^2 \right]^{0.5}.$$

The skin friction coefficient was computed as

$$c_{fv} = 2u_\tau^2 / u_e^2.$$

Baseline skin friction coefficient data with MHD off are shown in figure 21. Established smooth-plate, zero-pressure-gradient data are represented by the main curve, and two rough-plate skin friction curves are also shown for reference ( $k/x$  refers to the relative sand paper roughness). All test cases are shown, including available data from the MDTI and Princeton experiments. All NUWC data are either close to the smooth curve or above it, indicating that skin friction values were greater than the smooth-plate skin friction, as they should be since the MHD plate is not perfectly smooth. The MDTI and Princeton data are consistently below the smooth-plate skin friction curve, indicating skin friction values lower than those of a fully developed turbulent boundary layer in a zero pressure gradient. This finding suggests that the MDTI/Princeton data were collected in an adverse pressure gradient or in a transitional boundary layer.

The average force data for NUWC's repeat of the MDTI test cases are shown in figure 22. Absolute force is shown in newtons as a function of the flow velocity. Data are plotted sequentially according to the MDTI test matrix in table A-1 in the appendix. As can be seen, very little force is registered below 2.5 meters/second. Tests showed that the force balance could only measure forces greater than 0.5 newton, corresponding to the drag produced by a flow velocity of 3.0 meters/second. This is due to the added friction produced by the cables attached to the electrodes. For the 4-meter/second test cases, 1.8 newtons were measured. With MHD turned on, there was virtually no difference in drag force, as is more clearly presented in figure 23. Here, an absolute difference in force is shown, together with the standard deviation. For conclusive drag reduction to be suggested, the difference in drag must be greater than the standard deviation. In no case was the difference in force found to be greater than the standard deviation.

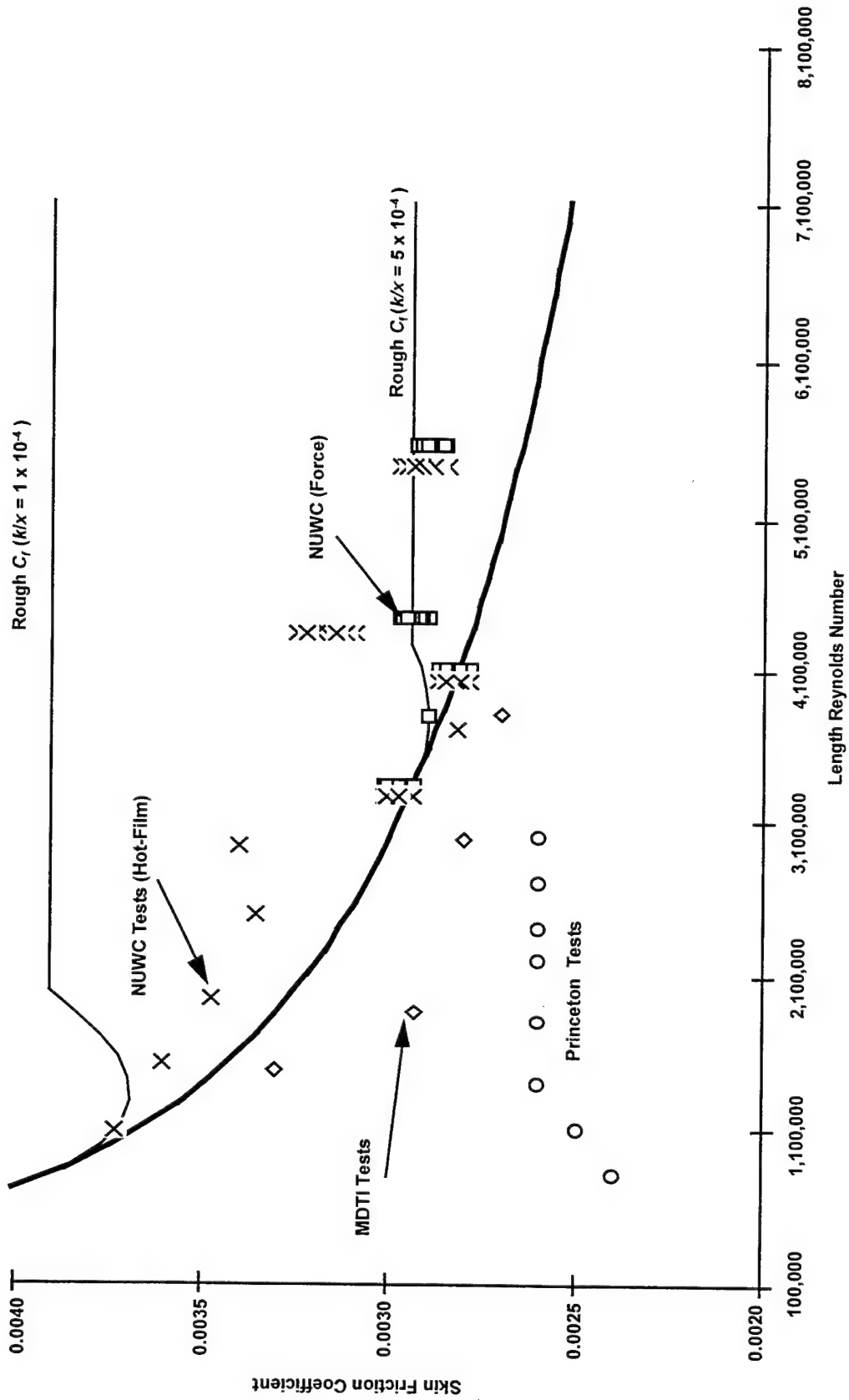
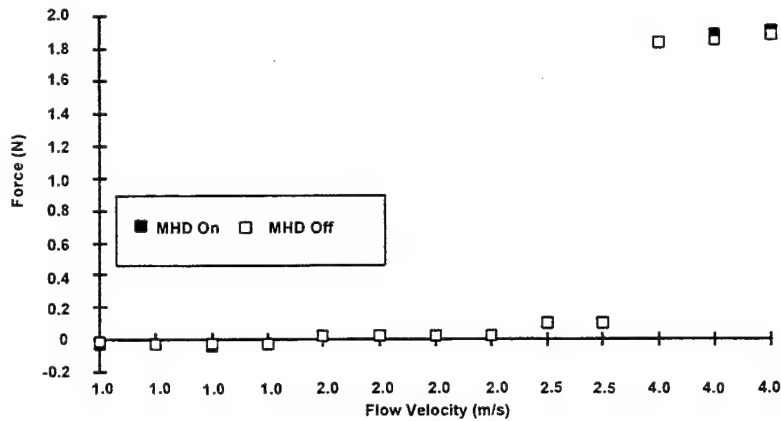
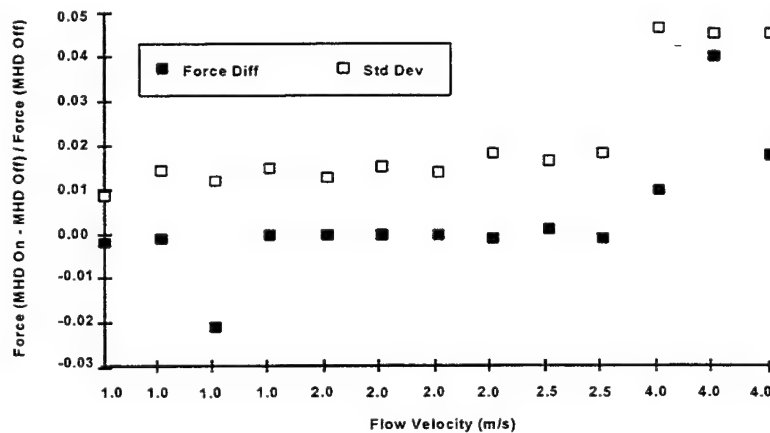


Figure 21. Baseline Skin Friction Coefficient Data for MHD-Off Test Cases  
(Princeton and MDTI baseline tests shown for comparison.)



**Figure 22. Average Drag Force for NUWC Repeat of the MDTI Tests**  
(Note: Abscissa is not linear.)



**Figure 23. Difference in Average Drag Force for NUWC Repeat of MDTI Tests**  
(Note: Abscissa is not linear.)

Figure 24 displays the hot-film friction velocities for the MHD-on and MHD-off test cases. Absolute average film velocities are shown sequentially according to the MDTI test matrix. As can be seen, average film velocities correlate very well with freestream tunnel velocity, indicating that the hot-films were properly calibrated. Again, with MHD turned on, there is virtually no difference between the two average hot-film velocities. The skin friction velocity and turbulence intensity are shown in figures 25 and 26, respectively. In all hot-film velocity test cases, there was no consistent difference between the MHD-on and MHD-off test cases.

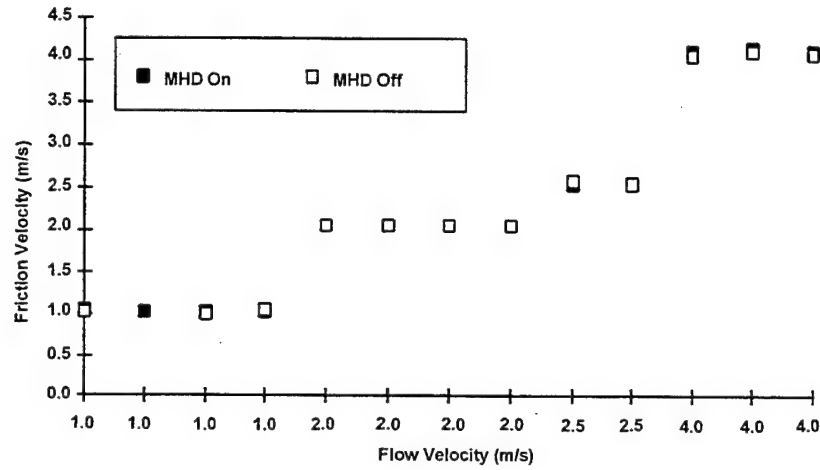


**Figure 24. Average Hot-Film Sensor Velocities for NUWC Repeat of MDTI Tests**  
(Note: Abscissa is not linear.)

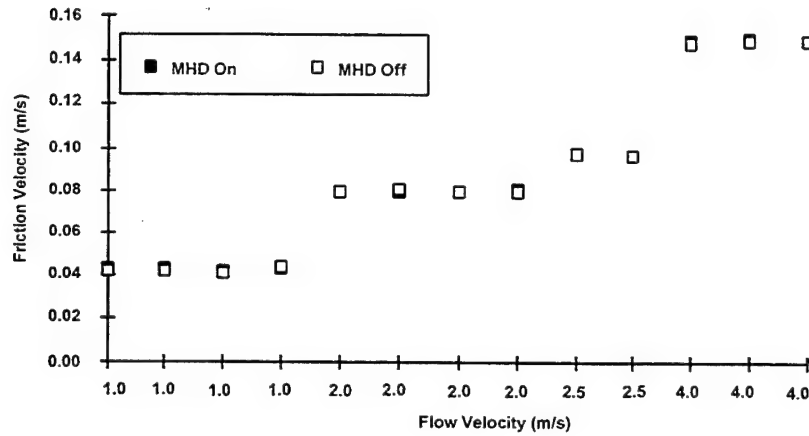


**Figure 25. Reduced Average Hot-Film Sensor Friction Velocities for NUWC Repeat of MDTI Tests**

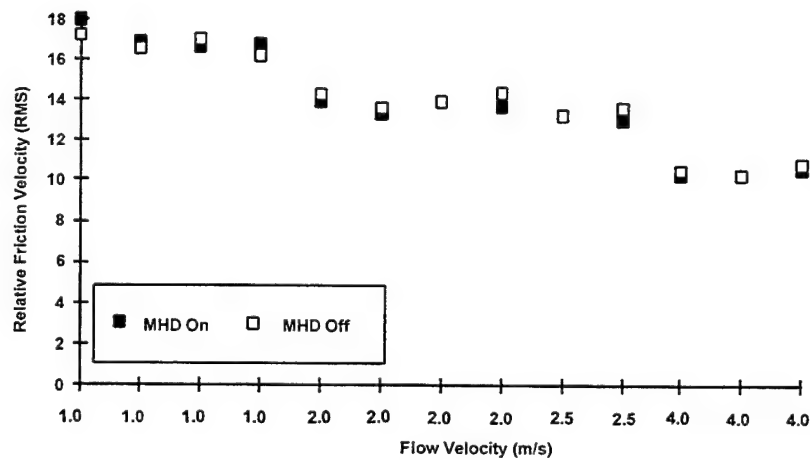


**Figure 26. Average Friction Velocity (RMS Values) for NUWC Repeat of MDTI Tests**

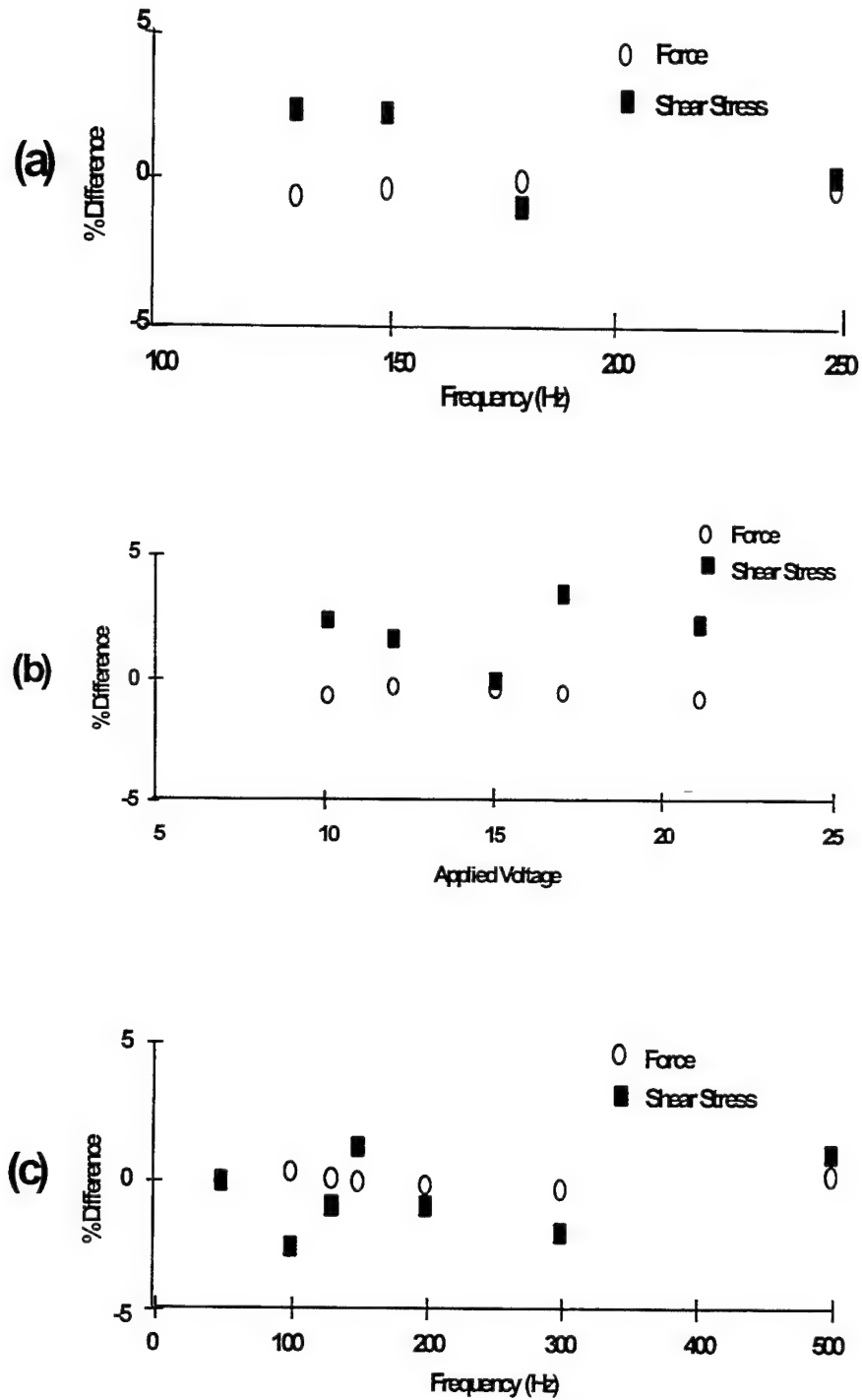
Figures 27a through 27c show the results of a NUWC repeat of a Princeton test case; figure 27a is for a constant flow velocity of 3 meters/second and a constant MHD voltage of 10 volts; figure 27b is for a constant flow velocity of 3 meters/second and constant pulsing frequency of 130 Hz; figure 27c is for a constant flow velocity of 3.7 meters/second and a constant MHD voltage of 17 volts. The percent differences in shear stress and drag force are shown relative to the MHD-off test cases to highlight any possible changes, regardless how small. As one can see in all three figures, standard error in the hot-film results was approximately 2%, and standard error in force balance data was on the order of 5%. The force data are consistently below the standard error, suggesting no overall drag reduction. Shear stress data are also on the order of the standard error, suggesting little to no local skin friction reduction.

Figures 28a through 28h show the percent difference in force and shear stress for several velocities and MHD voltages, and a constant pulsing frequency of 150 Hz. For all cases, the difference in the force data is consistently smaller than the standard error. Also, there does not appear to be any significant reduction in local shear stress except for the 3.4-meter/second, 21-volt case (figure 27g). For this case, initial results indicated a 16% decrease in local shear stress. To reconfirm this result, the test was rerun, and the rerun test showed an 8% reduction in local shear stress. Examination of the electrodes for the rerun test demonstrated significant electrode degradation, with current levels at half the initial-design current levels. This current loss accounts for the difference in the results. Regardless, even though a local skin friction reduction was observed, there was no indication of global drag reduction from the force balance data.

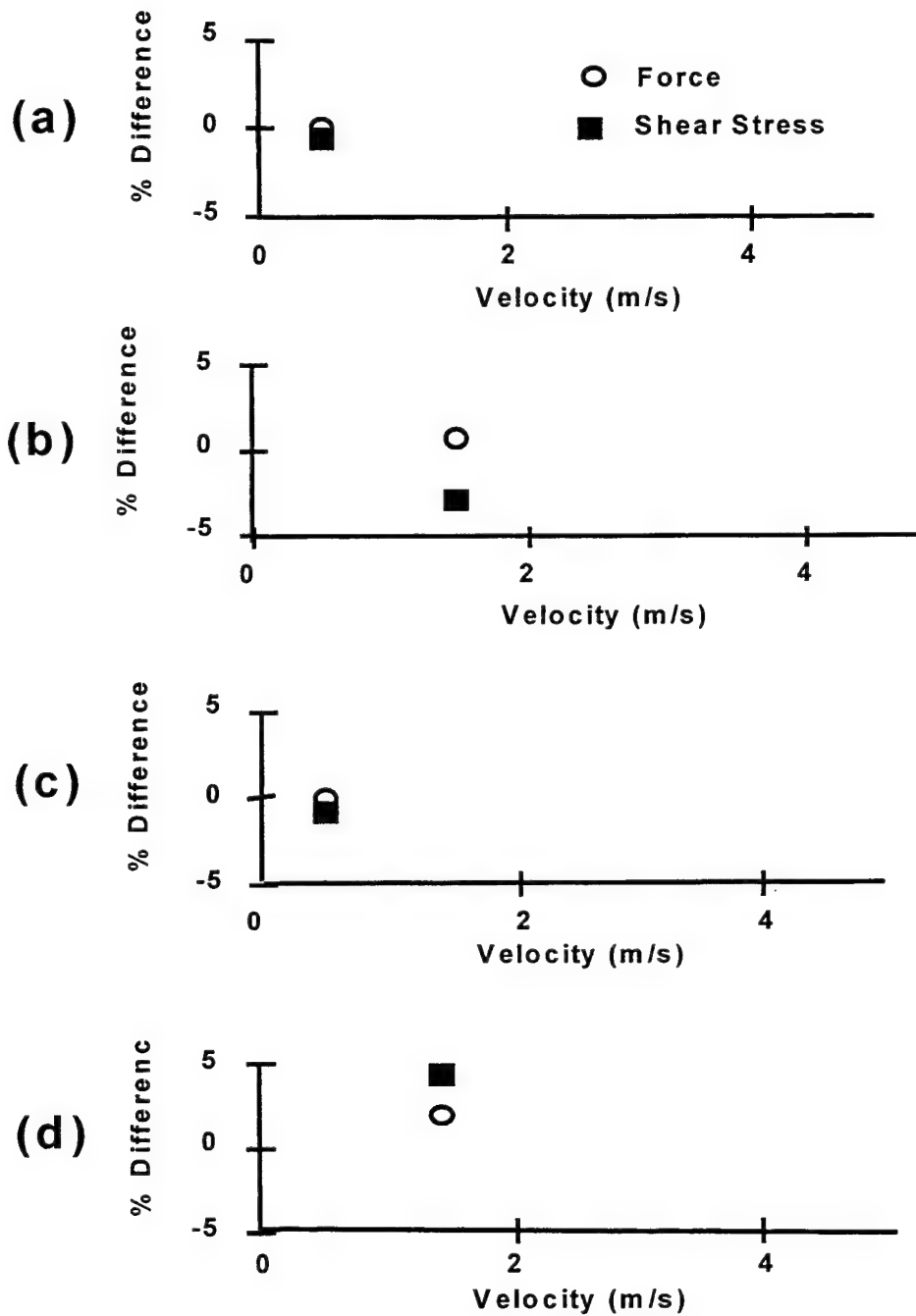
The skin friction coefficient was computed based on the local skin friction velocity and the force balance data. The results are shown in figure 29. For the entire test matrix, there is no difference in the force balance data for the MHD-on and MHD-off test cases. There is no consistent decrease in the local skin friction except for the 3.4-meter/second case. The skin friction coefficient computed from the force balance data is consistently 10% less than the skin friction coefficient computed from the local skin friction velocity. A possible explanation for this discrepancy is that the force balance data consist of globally integrated values over the entire plate, while the hot-film data are inherently a local measurement.

Figure 30 shows the turbulence intensity derived from the hot-film velocity data. As freestream velocity is increased, turbulence intensity decreased. Above 3 meters/second, the turbulence intensity was on the order of 12%. With MHD turned on, there was minimal effect on the turbulence intensity, and certainly no consistent effect was observed.

In the NUWC tests, additional test cases were run based on analysis of turbulent time scales for flow velocities of 4 and 5 meters/second. These higher velocities were examined to assess higher Reynolds number effects. Another objective of the tests was to attempt to pulse the MHD array at frequencies in the range of the bursting frequency (and higher), in order to explore any effect on the turbulent boundary layer. Average force values of 2.5 and 4.5 newtons were seen for flow velocities of 4 and 5 meters/second, respectively. Analysis of hot-film velocity data continued to show reliable calibration at these higher velocities. On average, standard error in the hot-film velocity data was on the order of 1.5%, and standard error in the force balance data was on the order of 2.5%.



**Figure 27. Average Local Shear Stress and Global Drag Reduction for NUWC Repeat of Princeton Tests: (a) 3 Meters/Second at 10 Volts vs Frequency; (b) 3 Meters/Second vs Voltage at Different Frequencies; (c) 3.7 Meters/Second at 17 Volts vs Frequency**



**Figure 28. Average Local Shear Stress and Global Drag Reduction for NUWC Repeat of Princeton Tests: (a) 1 Meter/Second at 5.5 Volts; (b) 1.4 Meters/Second at 6 Volts; (c) 1.8 Meters/Second at 6 Volts; (d) 2.3 Meters/Second at 8 Volts (For all cases,  $f = 150$  Hz.)**

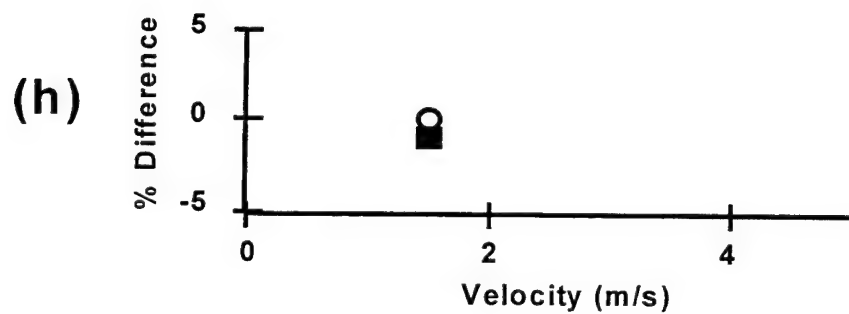
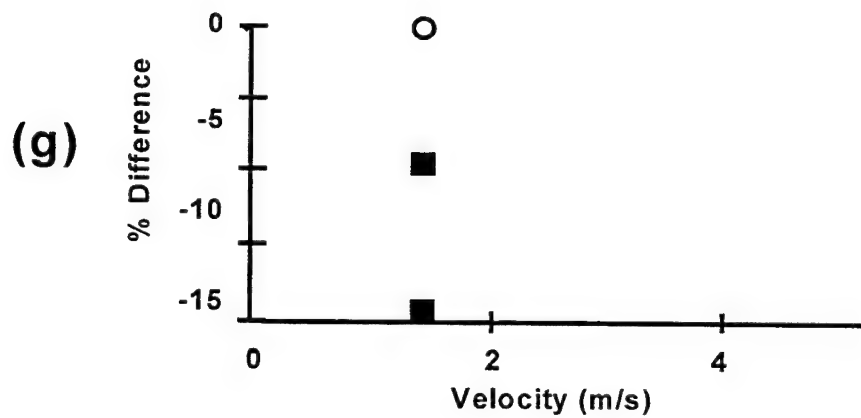
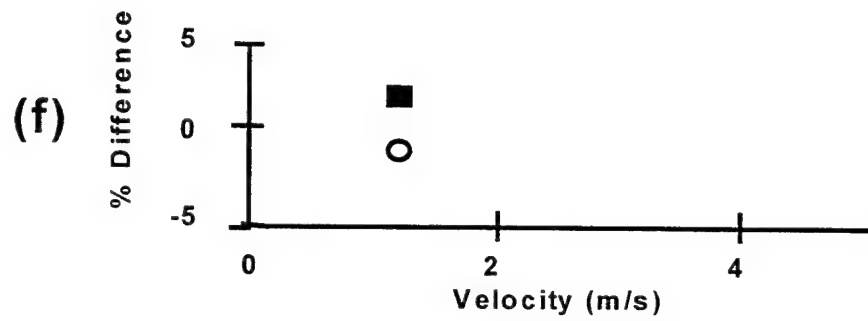
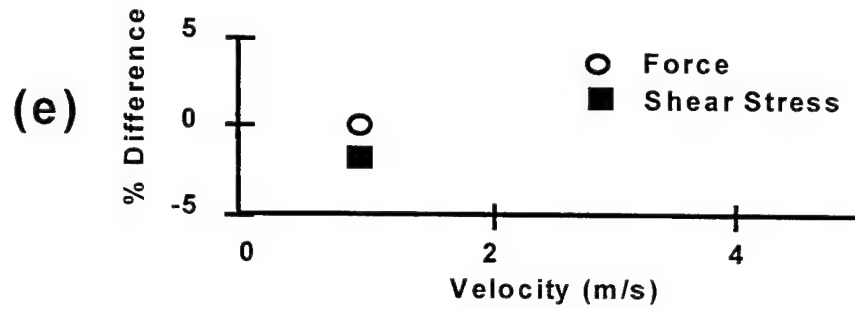


**Figure 28 (cont'd). Average Local Shear Stress and Global Drag Reduction for NUWC Repeat of Princeton Tests: (e) 2.7 Meters/Second at 10 Volts; (f) 3 Meters/Second at 21 Volts; (g) 3.4 Meters/Second at 21 Volts; (h) 3.7 Meters/Second at 21 Volts (For all cases,  $f = 150$  Hz.)**



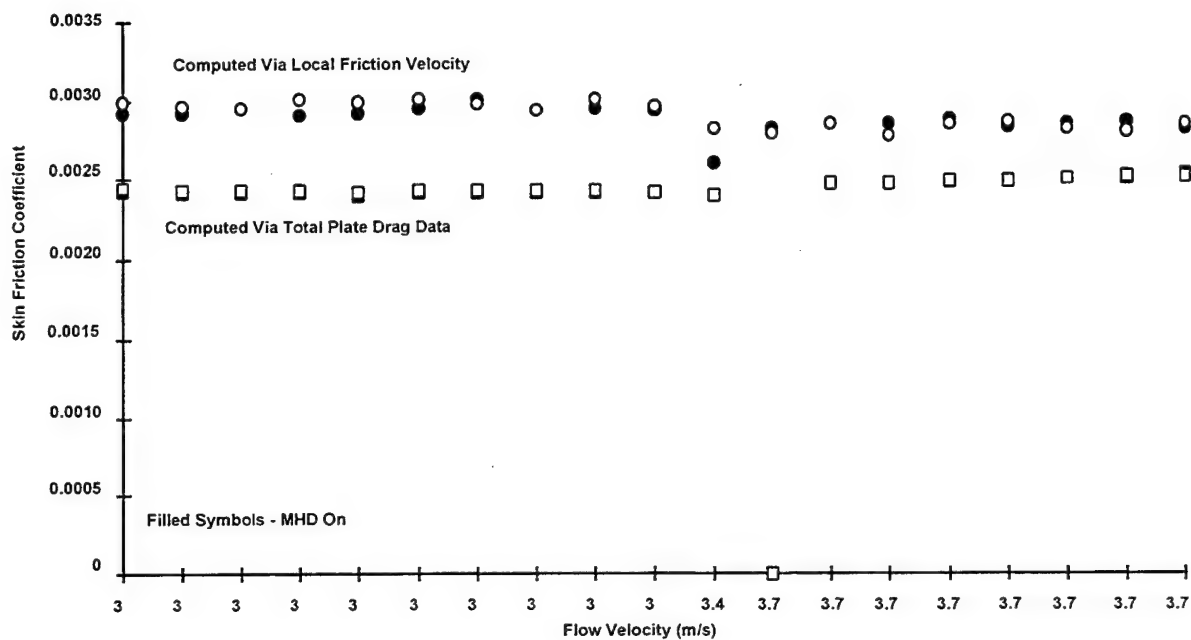


**Figure 29. Average Skin Friction Coefficient Data Compiled from Average Hot-Film Data and Global Drag Force Measurements for NUWC Repeat of Princeton Tests**

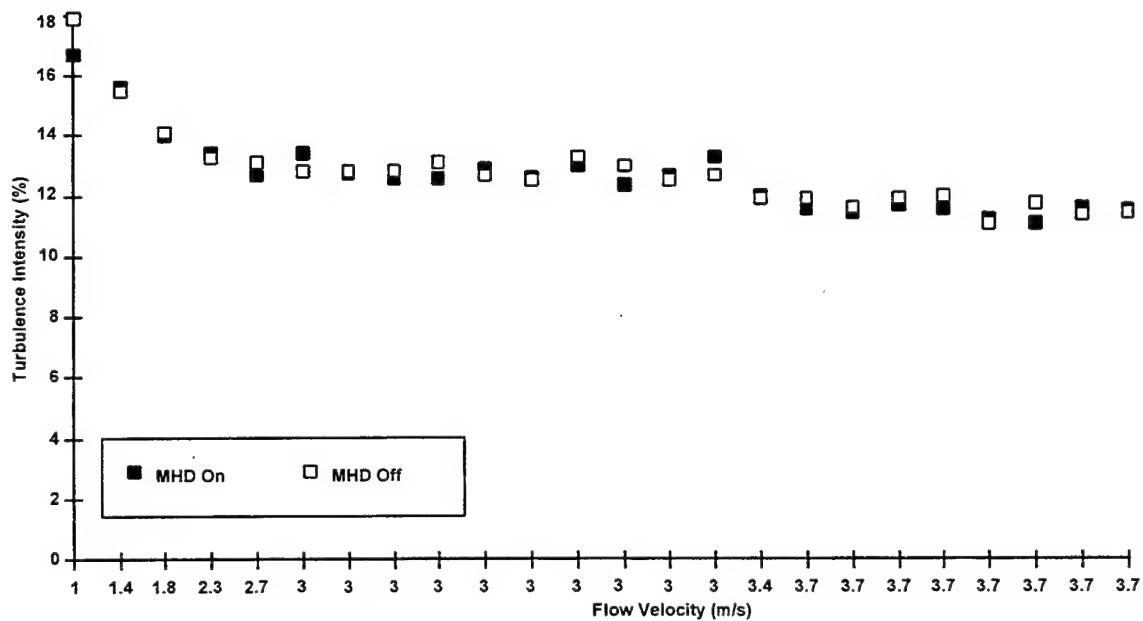


**Figure 30. Average Turbulence Intensity Results from NUWC Repeat of Princeton Tests**

Figure 31 shows the percent difference in drag force for the MHD-on and MHD-off test cases, as well as the standard deviation for each individual test case. A constant flow velocity of 4 meters/second was examined over a range of pulsing frequencies (figure 31a) at constant MHD voltage of 10 volts (figure 31a) and over a range of MHD array voltages for a constant 500-Hz pulsing frequency (figure 31b). These test cases were conducted to explore the sensitivity of any reduction to voltage and pulsing frequency. As can be seen, the standard deviation (indicative of the experimental uncertainty) is relatively constant at 2.5 to 3%. In all cases, differences in drag are below the standard deviation, suggesting no drag reduction effect over the range of the applied Lorentz force.

Figure 32 plots the percent difference in force and shear stress. The data show a maximum shear stress reduction of 6% for the 500-Hz, 40-volt test case. There also appears to be a 4.5% local shear stress reduction for the 30-Hz, 10-volt test case. These values are significantly lower than the 40-50% local shear stress reduction claimed by Princeton and MDTI.

The 5.0-meter/second test results are presented in figure 33. The average percent difference in force and shear stress is shown for a constant MHD voltage of 10 volts over a range of pulsing frequencies (figure 33a) and for a constant pulsing frequency of 500 Hz over a range of voltages (figure 33b). The differences in force are consistently below the standard experimental error, suggesting no drag difference due to the applied Lorentz force. Slight changes (both positive and negative) that lie outside the standard error can be seen in the shear stress. These differences are less than 3%, however, and do not approach the large reductions in shear stress claimed by Nosenchuck and Brown (1993, 1994).

Derived skin friction coefficients for the NUWC test series are shown in figure 34. These skin friction coefficients were computed via both drag force data and hot-film anemometry. For the 4-meter/second cases, skin friction coefficients from both approaches are within 10% of each other. For the 5-meter/second cases, the skin friction coefficient computed via drag force data is significantly greater. The hot-film results show a decrease in skin friction coefficient with increased velocity, while the coefficients computed via drag force data increase where previous results suggest they should decrease. This result may be due to nonlinearity in the force calibration curve. Nevertheless, there is no significant change in skin friction with MHD on.

Turbulence intensity is shown in figure 35 for the NUWC test series. A reduced scale is shown to accentuate any possible differences in turbulence. As can be seen, there is no consistent change in turbulence as the Lorentz force is applied. The spread of the data from test to test with MHD off clearly encompasses all of the MHD-on cases.

All skin friction coefficient data for the NUWC test cases, as well as for previously obtained Princeton and MDTI data, are shown in figure 36. Smooth (laminar) and turbulent skin friction curves are shown for reference. The Princeton and MDTI skin friction coefficient data were obtained from local shear stress measurements using hot-film anemometry. As stated earlier, all the NUWC data lie above the turbulent skin friction curve, as they should, suggesting that fully turbulent, approximately zero pressure gradient flow conditions were present during testing. The MHD-off test data collected by Princeton and MDTI suggest that either the flow was not fully turbulent or a significant adverse pressure gradient existed during testing. It is intriguing that the MDTI data show a local shear stress reduction on the order of 40% for Reynolds numbers below  $2 \times 10^6$  (corresponding to flow velocities below 2.5 meters/second). At higher Reynolds numbers (velocities above 4 meters/second), the MDTI measurements suggest little change in shear stress values, while the Princeton data show substantial local shear stress reduction, with maximum values approaching 50%. Neither of these reductions was found in the NUWC test cases.

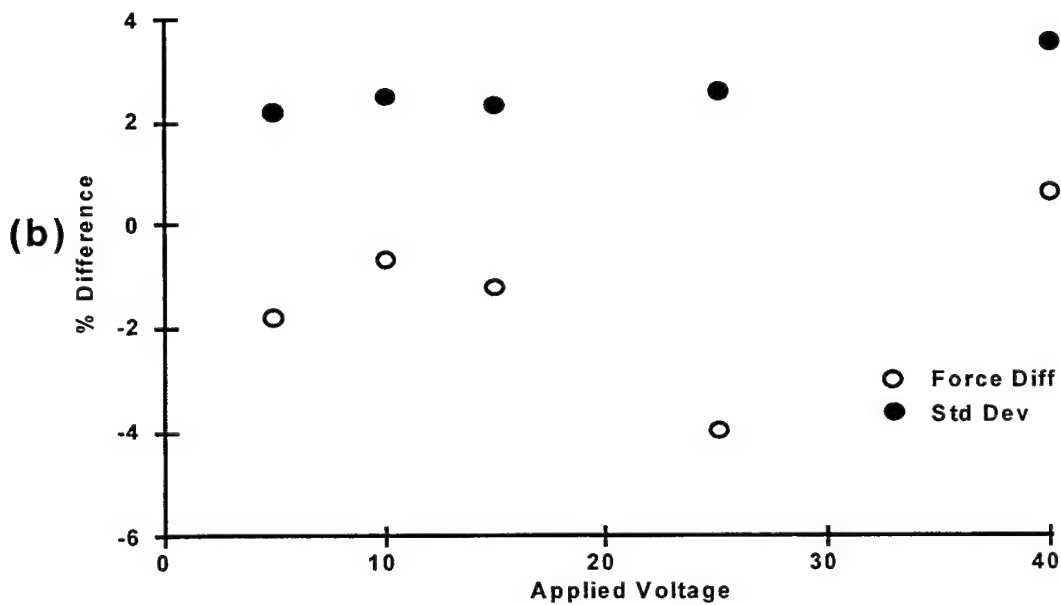
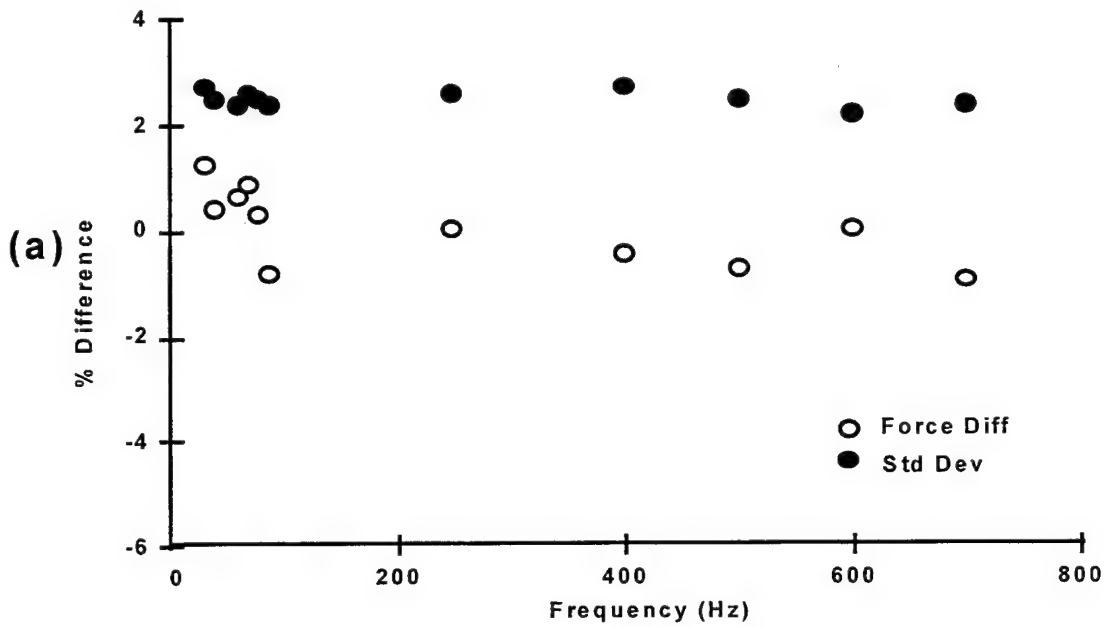


**Figure 31. Average Difference in Drag Force and Standard Deviation of Drag for NUWC Test Series: (a) 4 Meters/Second at 10 Volts; (b) 4 Meters/Second and 500-Hz Pulsing Frequency**

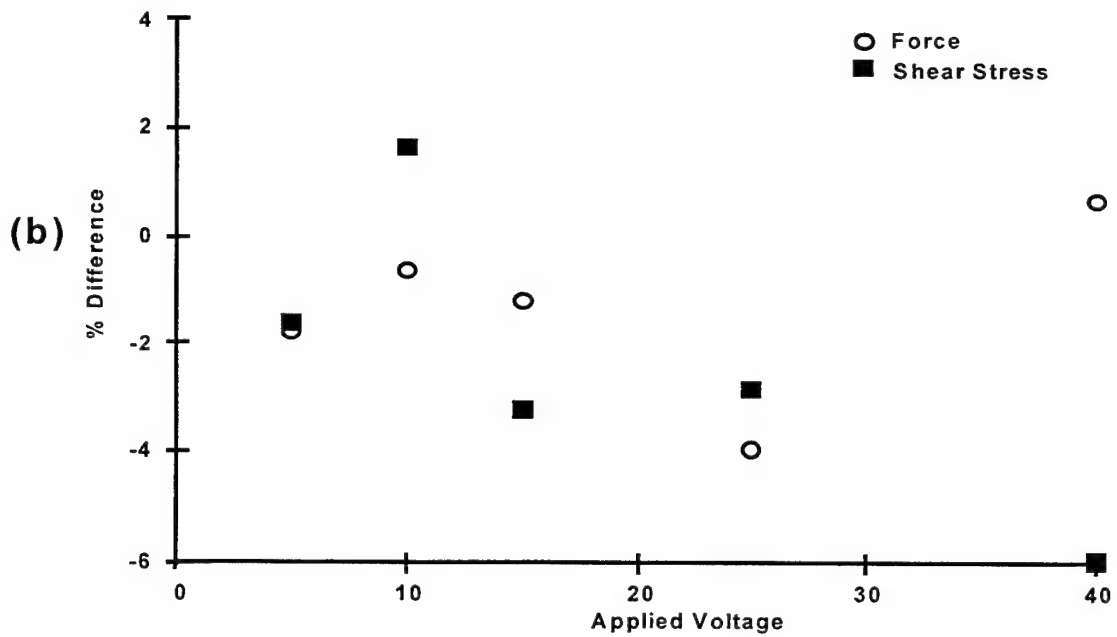
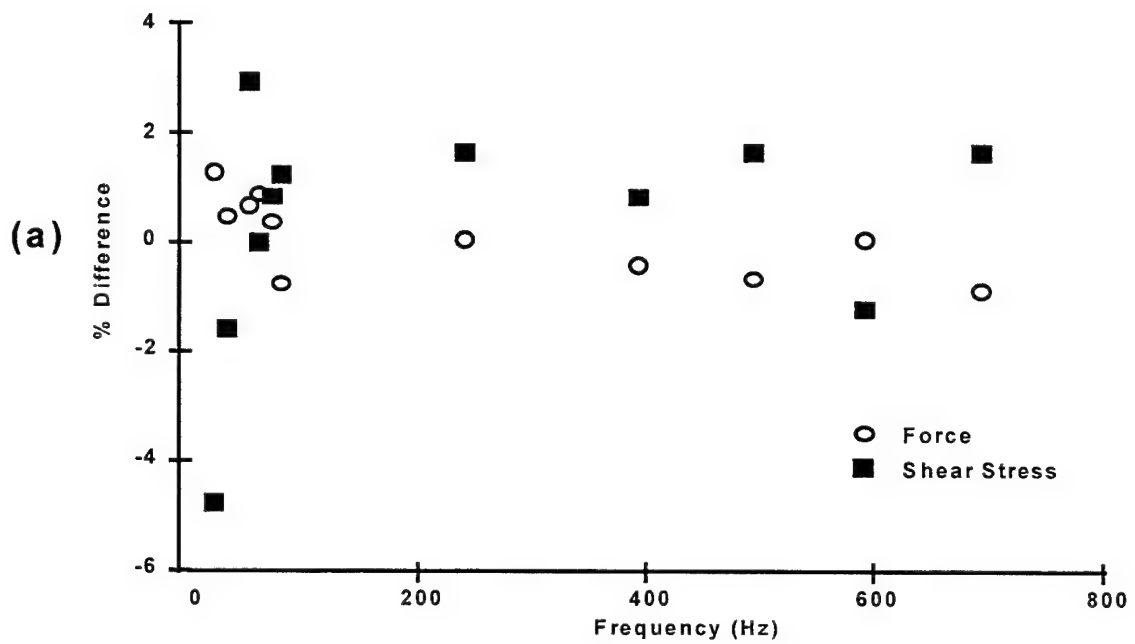


**Figure 32. Average Difference in Drag Force and Shear Stress for NUWC Test Series:**  
**(a) 4 Meters/Second at 10 Volts; (b) 4 Meters/Second and 500-Hz Pulsing Frequency**

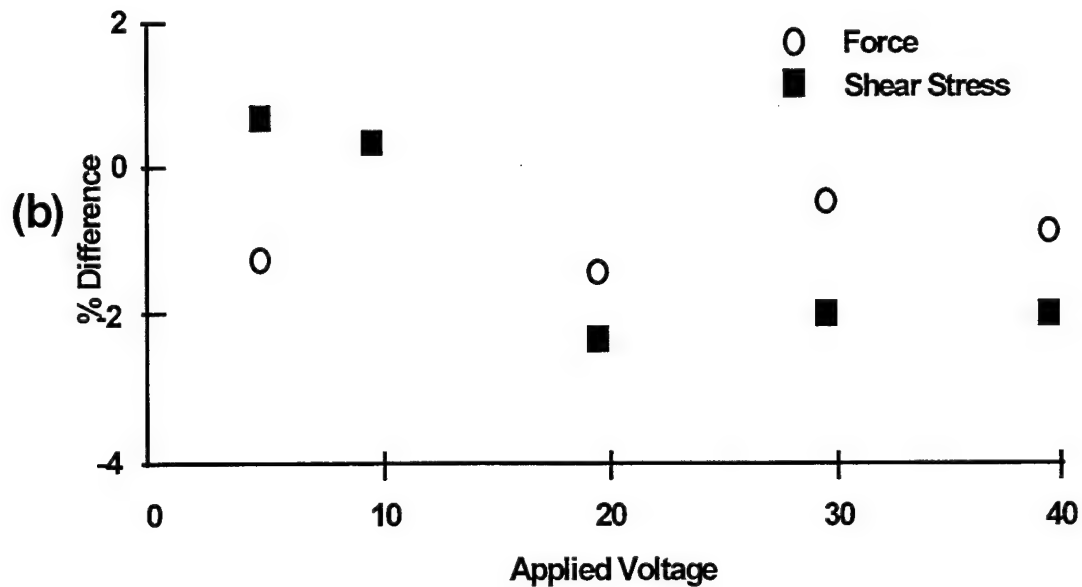
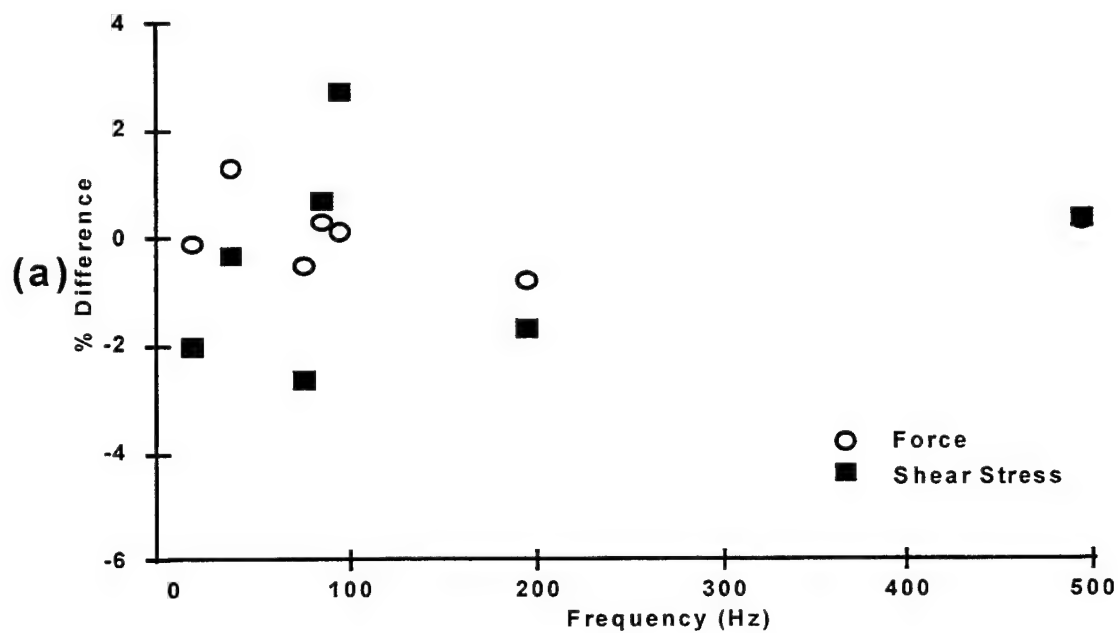


**Figure 33. Average Difference in Drag Force and Shear Stress for NUWC Test Series:**  
(a) 5 Meters/Second at 10 Volts; (b) 5 Meters/Second and 500-Hz Pulsing Frequency

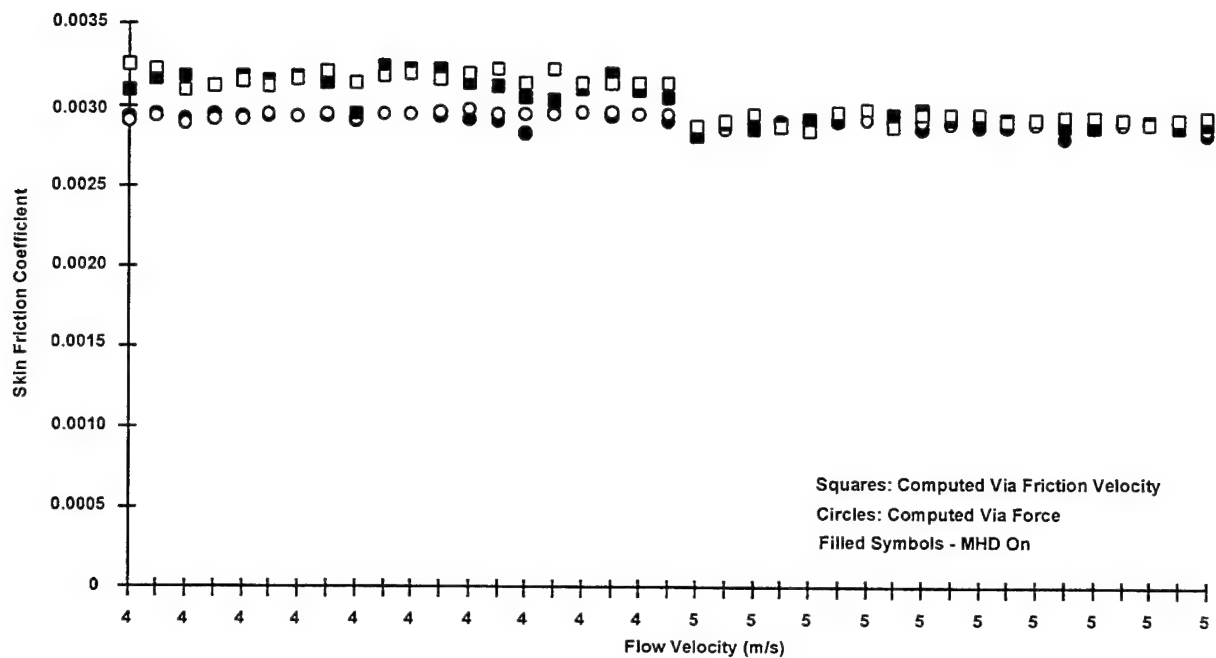


**Figure 34. Average Skin Friction Coefficient Data Compiled from Average Hot-Film Data and Global Drag Force Measurements for NUWC Test Series**  
 (Note: Abscissa displays specific test cases at a given velocity.)

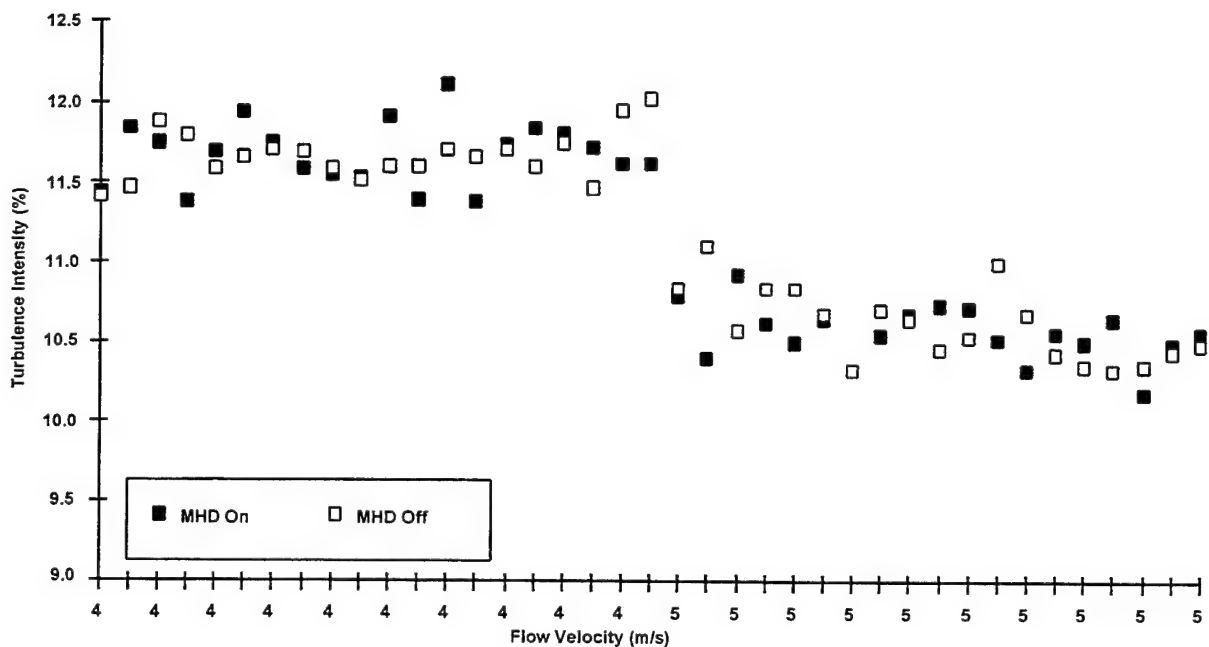


**Figure 35. Average Turbulence Intensity Results from Entire NUWC Test Series**  
 (Note: Abscissa displays specific test cases at a given velocity.)

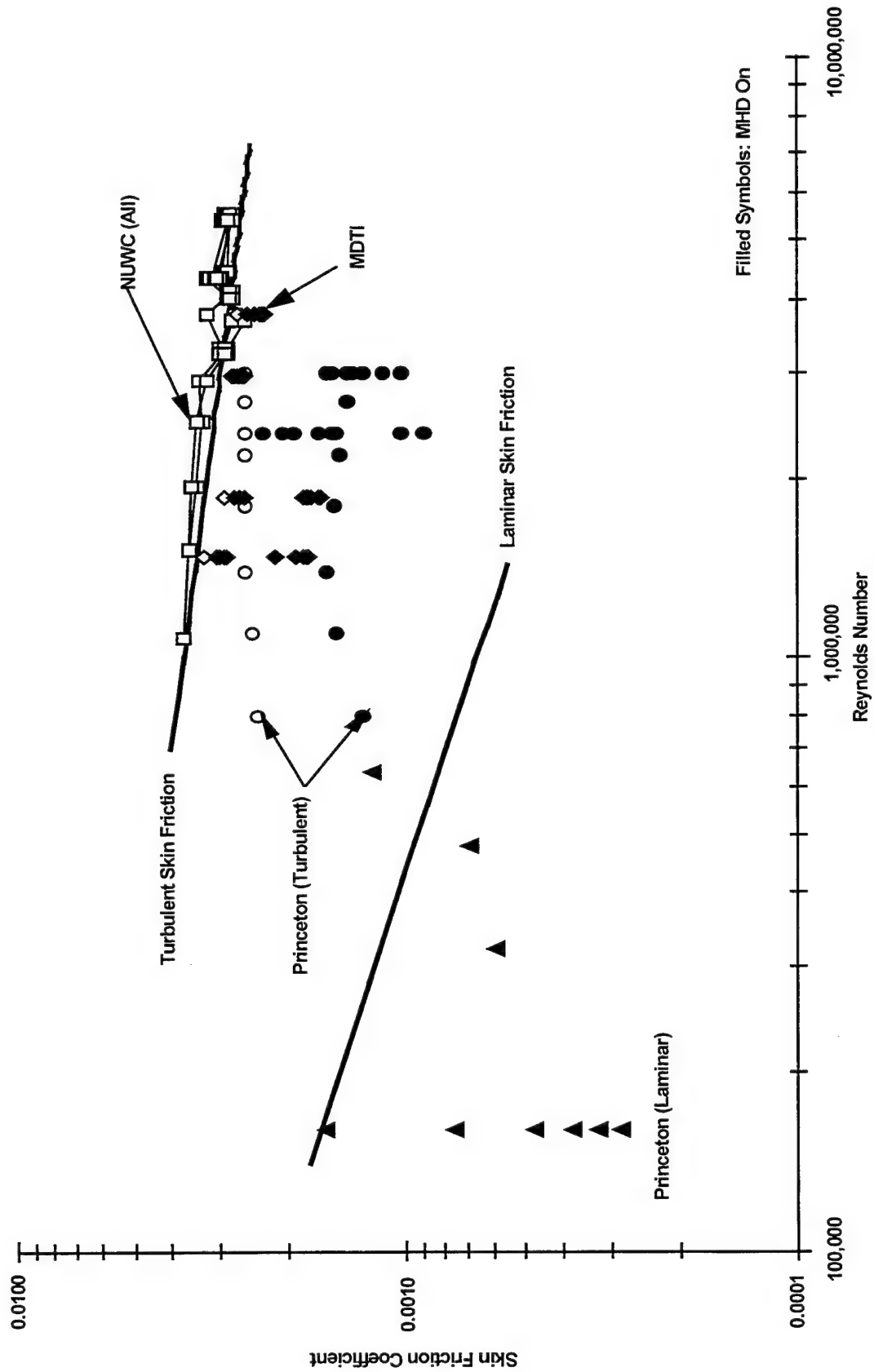


Figure 36. Skin Friction Coefficient Data for MHD-On and MHD-Off Test Cases  
(NUWC data include repeats of Princeton and MDTI test matrixes;  
Princeton and MDTI data taken from their respective experimental results.)

## 4.2 TURBULENCE DATA ANALYSIS

Hot-film data were converted to shear stress data in order to examine various turbulence statistics based on shear stress and to allow consistent checking with published data. The shear stress value was normalized by its standard deviation. The mean value of the shear stress was then subtracted to locate the mean value at zero. Mathematically, the ordinate axis is

$(\tau - \tau_{mean})/\sigma_\tau$ , where  $\tau$  is the shear stress and  $\sigma_\tau$  is the standard deviation. The probability was then computed using 50 evenly spaced points across the entire range of shear stress values computed versus the Rayleigh distribution. The Rayleigh probability distribution is given as

$$P(\tau) = \frac{\tau}{\sigma_\tau^2} e^{-\frac{\tau^2}{2\sigma_\tau^2}}.$$

For all histograms plotted,  $\tau/\sigma_\tau$  corresponds to the ordinate value, with  $\sigma_\tau$  defined as the square root of the shear stress standard deviation. Choosing  $\sigma = \sqrt{\sigma_\tau}$  provided a Rayleigh distribution similar to the one obtained from the experimental results.

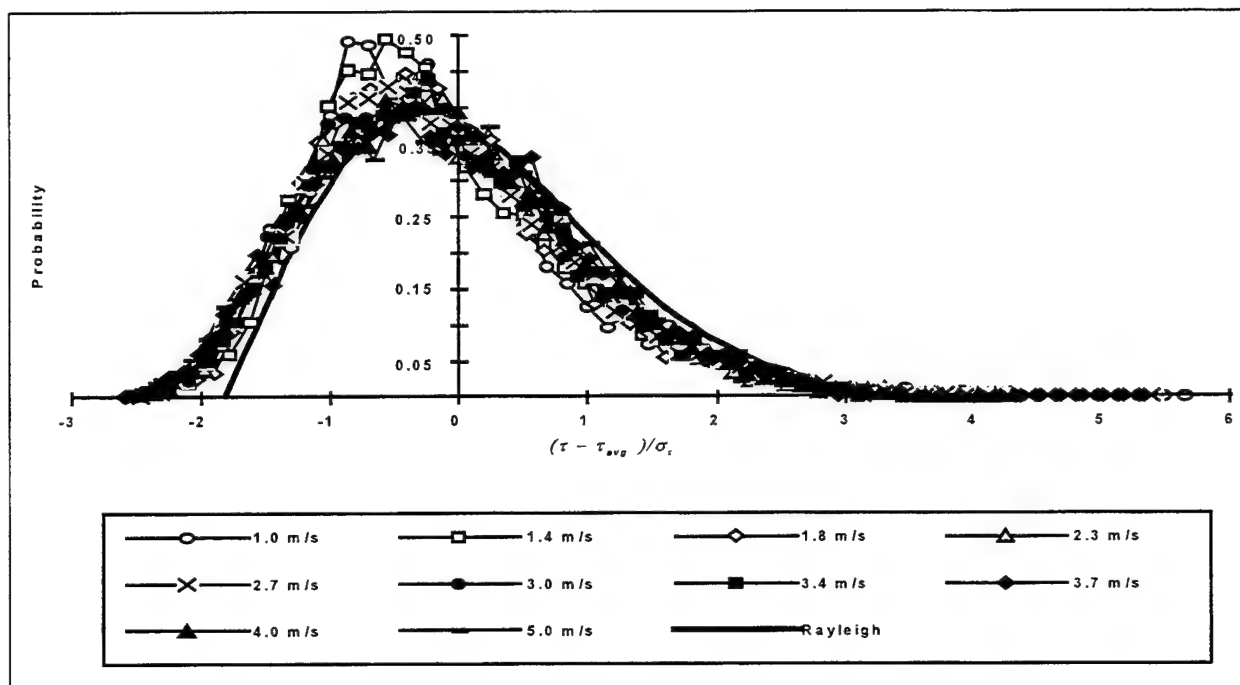
The PDFs of shear stress associated with a fully developed turbulent boundary have been demonstrated by Sreenivasan and Antonia (1977) to follow a Rayleigh distribution, and the curves are self-similar (i.e., the same regardless of Reynolds number). Figure 37 shows PDFs of the shear stress derived from the hot-film data from the MHD plate with MHD off. Data for the entire range of freestream velocities are shown along with the theoretical Rayleigh distribution. As can be seen, all of the data collapse approximately to a single distribution. This observation suggests that the test data presented here were indeed from a fully developed turbulent boundary layer over the entire range of flow velocities examined.

Figure 38 shows a histogram for the 3.4-meter/second, 21-volt, 150-Hz test case. As can be seen, when normalized by the mean and standard deviation with no current, the peak value of the distribution is approximately 0.45 and occurs at approximately -0.67 standard deviation (relative to the mean value). For the MHD-on case, the histogram is shifted to  $-1, 2\sigma_\tau$ . In addition, the Rayleigh distribution approximates the probability distribution of the shear stress data. Figure 39 shows the histogram for the same test case for the hot-film sensor located 11 inches downstream. As can be seen, the Rayleigh distribution overlays the distribution for the MHD-off test case. The histogram is again shifted to the left when MHD is on. In both cases, the shifting of the histogram suggests a redistribution of the turbulence by the MHD.

Figures 40 and 41 shows histograms for the 4-meter/second, 25-volt, 70-Hz test case for the two hot-film sensors, respectively. Again the Rayleigh distribution closely follows the MHD-off data, as it should. The distribution for MHD on is again slightly shifted to the left. For the downstream film, however, the histogram for MHD on is shifted to the right. This trend differs from the cases where a slight drag reduction was observed, and it suggests that the MHD may have had a downstream effect opposite to its upstream effect. In all of the remaining cases, however, the differences in PDF for the MHD-on and MHD-off cases were slight.

Power spectra were also computed and analyzed. To smooth the distributions, a Bartlett window function was used and a range of frequencies was discretized by 1024 points. The range depended on the sampling frequency (twice the Nyquist frequency), which governs the upper bound, and the duration of the sample, which governs the lower bound. In the results shown, power spectra of the shear stress were normalized by the square of the mean shear stress. The





**Figure 37. Probability Density Functions of Local Shear Stress  
Compiled from Hot-Film Data**

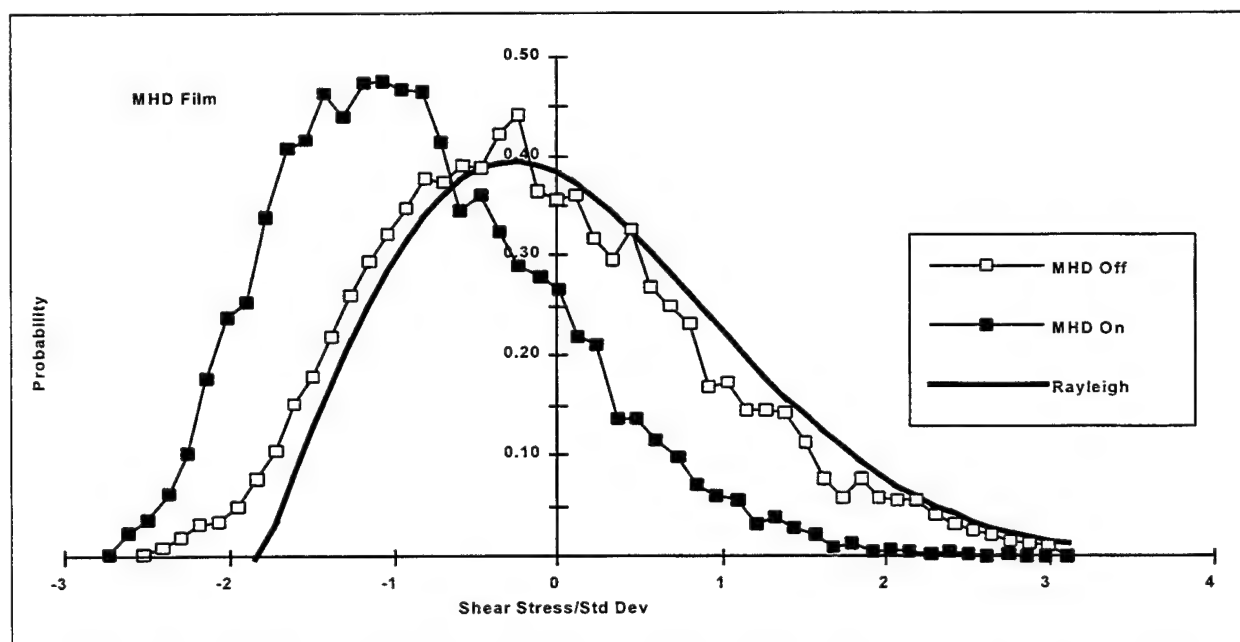


**Figure 38. Probability Density Function of Shear Stress from Hot-Film Sensor Located  
Adjacent to MHD Array (3.4 Meters/Second, 21 Volts, 150-Hz Pulsing Frequency)**

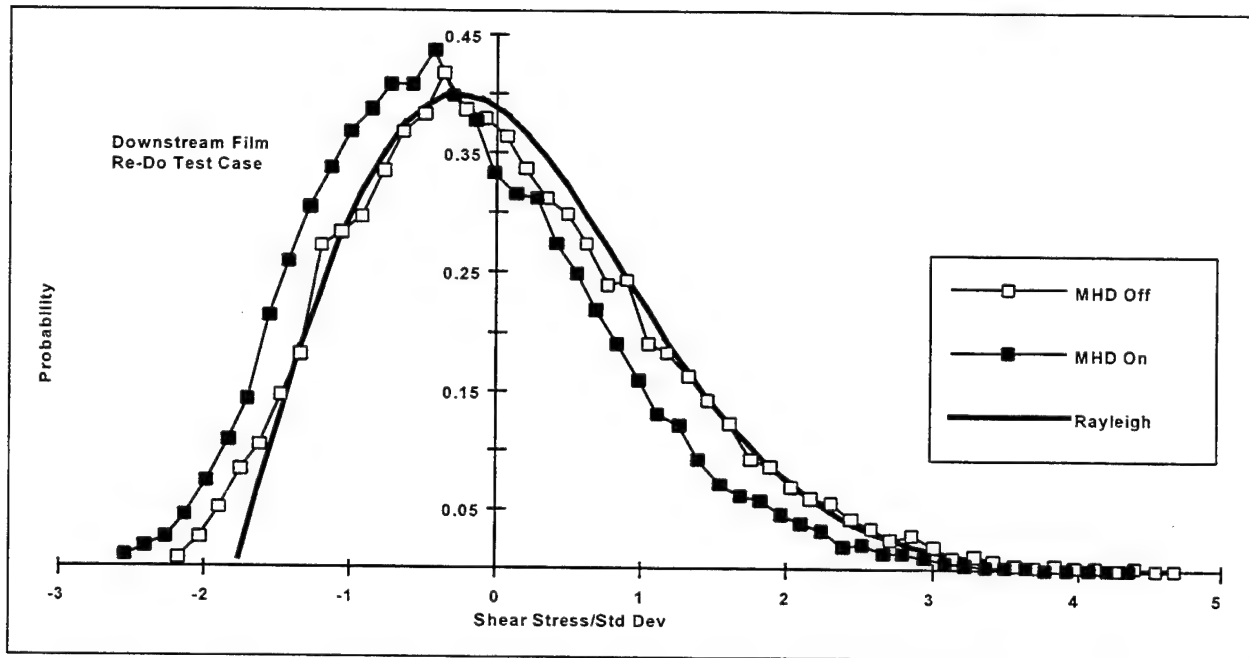


**Figure 39. Probability Density Function of Shear Stress from Downstream Hot-Film Sensor (3.4 Meters/Second, 21 Volts, 150-Hz Pulsing Frequency)**

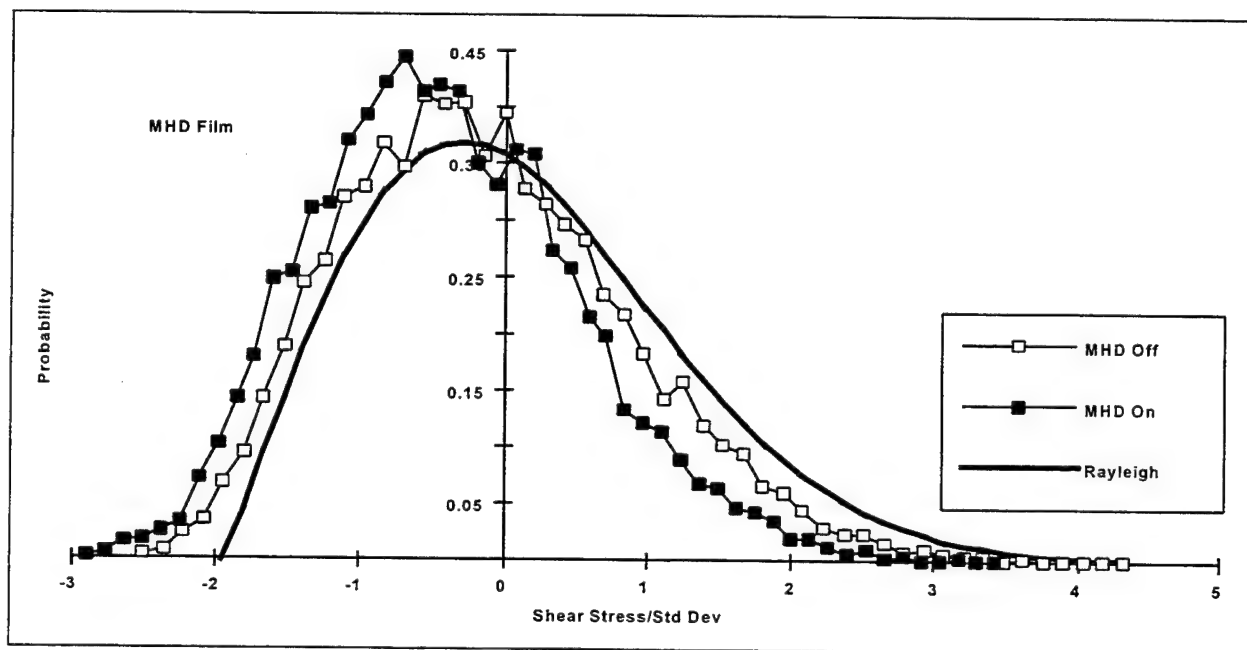


**Figure 40. Probability Density Function of Shear Stress from Hot-Film Sensor Located Adjacent to MHD Array (4 Meters/Second, 25 Volts, 70-Hz Pulsing Frequency)**

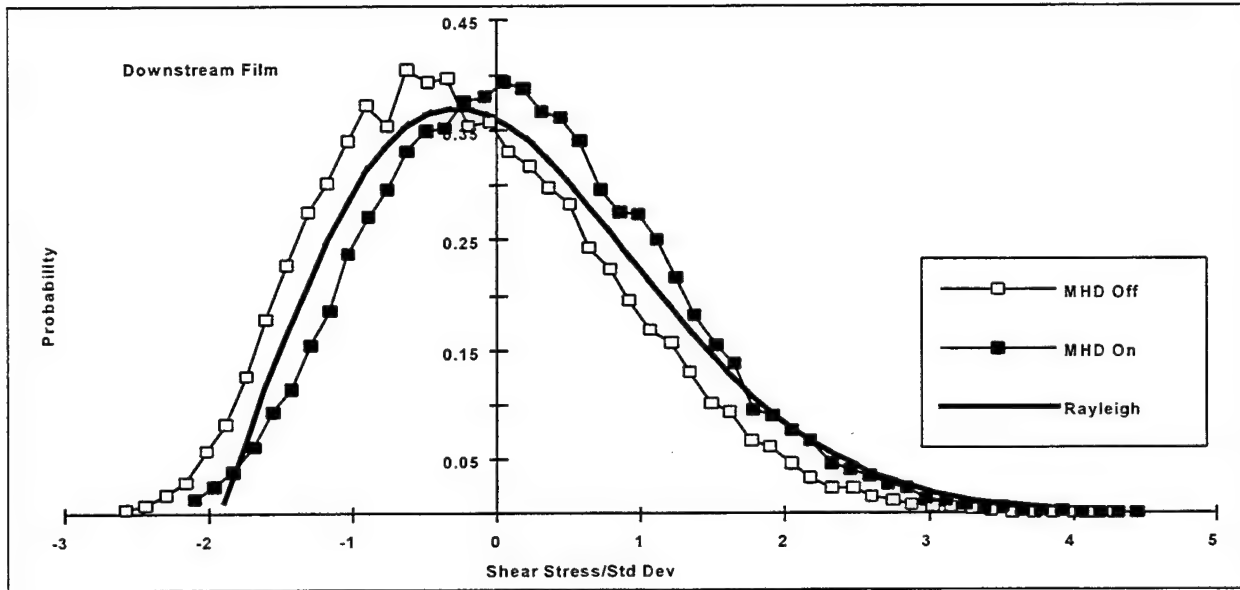


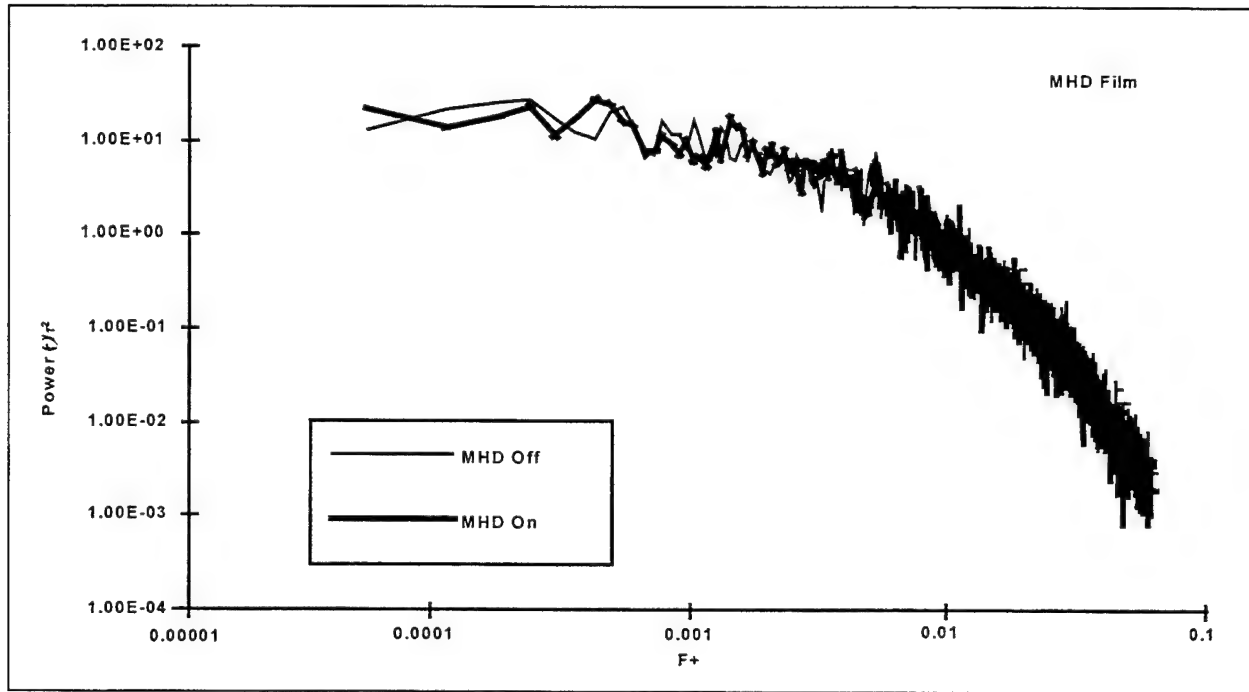
**Figure 41. Probability Density Function of Shear Stress from Downstream Hot-Film Sensor (4 Meters/Second, 25 Volts, 70-Hz Pulsing Frequency)**

power and frequency were scaled by the inner variables. Mathematically, the ordinate and abscissa are expressed as:

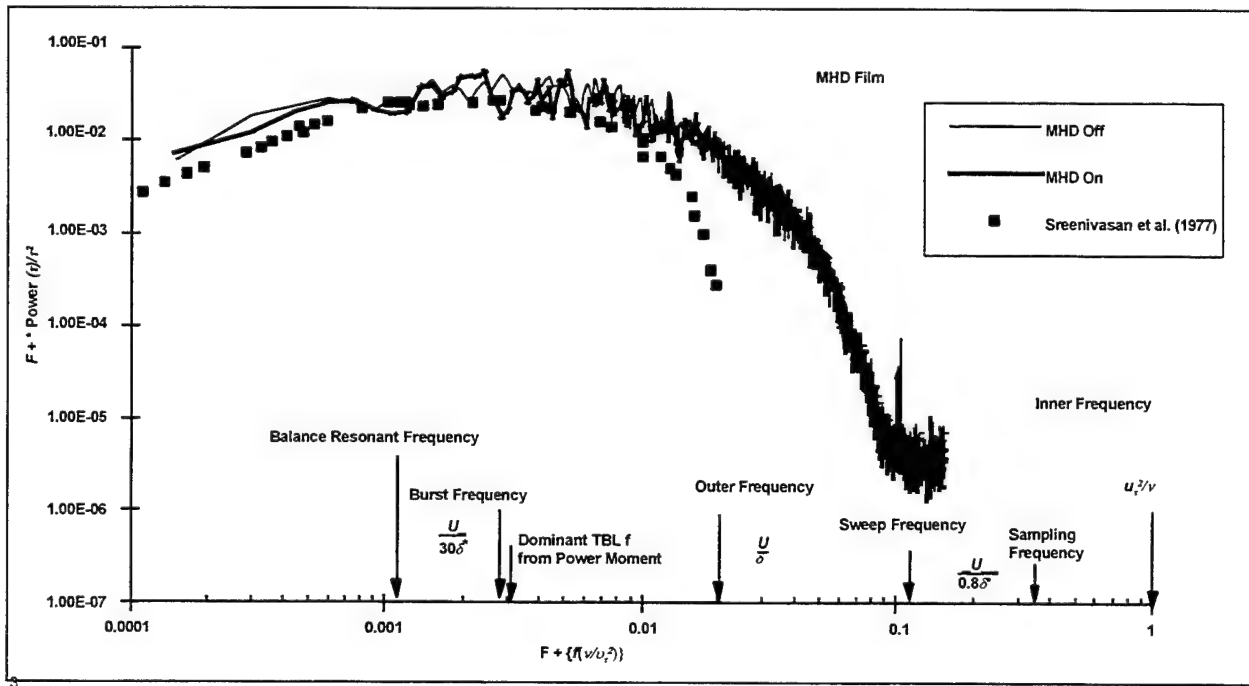
$$F^+ = f \frac{\nu}{u_\tau^2} \text{ (abscissa)} \quad \text{and} \quad \text{Power} = \frac{P(\tau) u_\tau^2}{\tau_{mean}^2 \nu} \text{ (ordinate)}.$$

Figure 42 shows the power spectrum for the 3.4-meter/second, 21-volt, 150-Hz test case on a logarithmic scale and scaled by the inner variables. This power spectrum is characteristic of spectra for turbulent boundary layers. The amplitude decreases slowly out to  $F^+ = 0.01$ ; thereafter, it decreases rapidly. Relatively, the power spectrum decreases five orders of magnitude from  $F^+ = 0.01$  to  $F^+ = 0.1$ . There is little noticeable difference between the MHD-on and MHD-off test cases. This result suggests that there was little or no change in the energy scale distribution of the turbulence. It appears then that the Rayleigh distribution is shifted as a result of a mean reduction in shear stress. However, the spectral content of the shear stress remains unchanged.

Figure 43 shows the first moment of the power spectrum, which was computed simply by multiplying the normalized power spectrum shown in figure 42 by the scaled frequency ( $F^+$ ). Peaks in the first moment distribution indicate the frequencies where dominant turbulent events occur. Since the hot-film sensor was located on the surface, it measured the dominant frequencies of inherently near-wall turbulent events. A peak in this distribution is observed at an  $F^+$  on the order of 0.003. In general, there is little difference between the MHD-on and MHD-off test cases. All first moment of power spectrum distributions also show peaks near an  $F^+$  of 0.003. For comparison, all boundary layer frequency characteristics, as well as instrumentation characteristic frequencies, are shown in figure 43. By definition,  $F^+ = 1.0$  corresponds to the inner scale frequency. A second spike in the power spectrum correlates well with the sweep frequency ( $F^+ = 0.12$ ). Finally, peaks in the power spectrum moment data correlate directly with the burst frequency (Kim et al., 1971), which is consistent with the known empirical finding that the dominant turbulent flow frequency is the burst frequency.



**Figure 42. Power Spectrum (Scaled by Inner Variables) of Wall Shear Stress (3.4 Meters/Second, 21 Volts, 150-Hz Pulsing Frequency)**



**Figure 43. First Moment of Power Spectrum (Scaled by Inner Variables) of Wall Shear Stress (3.4 Meters/Second, 21 Volts, 150-Hz Pulsing Frequency)**

### 4.3 PULSING FREQUENCY COMPARATIVE ANALYSIS

An analysis of the pulsing frequency versus the turbulent boundary layer characteristic frequencies was performed. Given the following water tunnel parameters:

distance from leading edge to center of MHD plate:  $x = 1.37$  meters,

density:  $1000 \text{ kg/meter}^3$ ,

kinematic viscosity:  $1.01 \times 10^{-6} \text{ meter}^2/\text{second}$ ,

friction velocity:  $u_\tau = \sqrt{\tau_0 / \rho} = \sqrt{0.0296(Re)^{-0.2}} U_0$ ,

boundary layer thickness:  $\delta = 0.37 \times Re_x^{-0.2}$ ,

displacement thickness:  $\delta^* = 0.04625 \times Re_x^{-0.2}$ ,

characteristic flow frequencies were computed. Microturbulent event duration was computed as  $T_e u_\tau^2 / \nu = 100$ , suggesting that the sampling frequency for microturbulent event duration should be  $f_1 = 1/T_p$ . The burst period (Kim et al., 1971) is  $U_0 T_B / \delta = 5.0$ , suggesting that the frequency of bursting is approximately  $f_2 = 1/T_B$ . The optimum frequency of actuation of the equal-phase MHD cells was suggested by Nosenchuck and Brown (1995). These frequencies were based on freestream velocity and separation distance of the MHD electrodes; i.e.,

$$f_3 = U_0 / l_1,$$

$$f_4 = U_0 / l_2,$$

where  $l_1 = 23 \text{ mm}$  (separation distance between rows of electrodes), and  $l_2 = 9 \text{ mm}$  (streamwise length of a single electrode).

Table 2 and figure 44 show the results of this analysis. All solid symbols in figure 44 not connected by lines display the range of pulsing frequency for all test conditions. Theoretically derived boundary layer frequencies (burst, ejection/sweep, inner and outer) are shown by the connected symbols. The primary power moment frequency was obtained for all flow velocities and is shown by the solid diamonds. Balance resonance is shown for reference. In addition, the maximum frequency where bubble formation was found to cease is also shown. Figure 44 shows that the primary frequency obtained from the power spectrum moment data consistently correlates with the theoretical burst frequency across all flow velocities. The Princeton and MDTI test cases were conducted above the burst frequency and below the outer frequency, while the NUWC test cases were conducted just below the burst frequency and approached the outer frequency.

The velocity dependence of the forcing frequency for a resonant condition can be derived as follows. The relevant dimensionless number is the ratio of Lorentz pressure to dynamic pressure, known as the MHD interaction parameter  $N = \sigma E B L / (1/2 \rho u_\tau^2)$ , where  $E$  is the electric field,  $\sigma$  is the fluid conductivity,  $B$  is the magnetic induction,  $L$  is the electromagnetic cell dimension,  $\rho$  is the fluid density, and  $u_\tau$  is the friction velocity. For MHD flows to be dynamically similar,  $N$  must remain constant. Given constant cell geometry, fluid properties, and magnetic induction, only the variable  $E$  must increase as  $u_\tau^2$ , or the electric power must increase as  $u_\tau^4$ . The dependence of the forcing voltage on velocity, which can be extracted from the hot-film data at the resonance condition, should be examined.

Table 2. Dominant Flow Frequencies for MHD Plate

Velocity (meters/ second)	$Re(U_x/\nu)$ $\times 10^6$	$u_\tau$ (meters/ second) $\times$ $10^{-3}$	$\delta$ (meters) $\times 10^{-3}$	$\delta^*$ (meters) $\times 10^{-3}$	$T_p$ (sec) $\times 10^{-3}$	$T_B$ (sec) $\times 10^{-3}$	$f_1$ (Hz) (micro- event freq)	$f_2$ (Hz) (burst freq)	$f_3$ (Hz) (cell freq)	$f_4$ (Hz) (elec- trode freq)
0.5	0.679	22.461	34.6	4.325	200.2	346	5	2.9	21.7	55.6
1.0	1.358	41.914	30.12	3.765	57.5	150.6	17.4	6.64	43	111.1
2.0	2.716	78.214	26.221	3.2776	16.51	65.55	61	15.25	87	222.2
3.0	4.0741	112.66	24.18	3.0223	7.96	40.3	126	25	130	333.3
4.0	4.4321	145.95	22.83	2.8533	4.74	28.54	211	35	174	444.4
5.0	6.7901	178.41	21.83	2.73	3.17	21.83	315	46	217	555.5

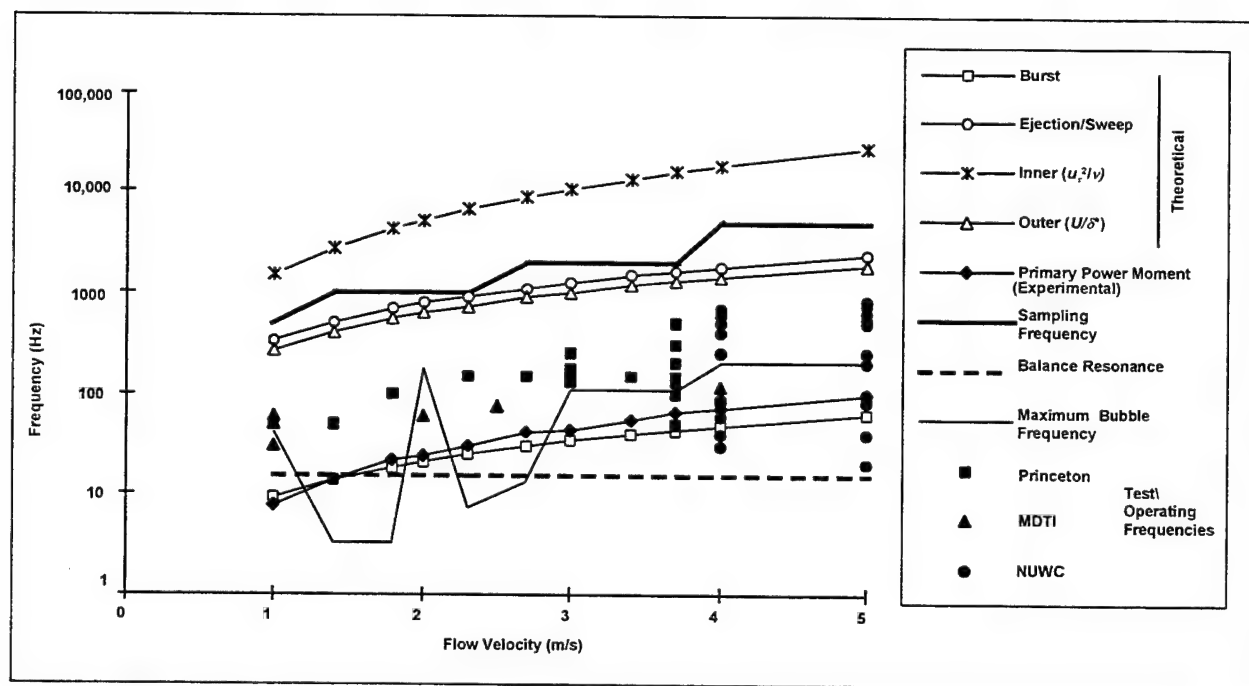


Figure 44. Dominant Turbulent Boundary Layer and MHD Pulsing Frequencies of the Entire Current Test Series

#### 4.4 RELEVANCE TO RESONANCE PHYSICS

Starting with the Navier-Stokes equations,

$$\rho \frac{D\bar{u}}{Dt} = -\nabla p + D \cdot \underline{\underline{\tau}} + \bar{J} \times \bar{B} = -\nabla p + D \cdot \underline{\underline{\tau}} + \sigma(\bar{E} \times \bar{B} + \bar{B}(\bar{u} \cdot \bar{B}) - B^2 \bar{u}),$$

where  $\underline{\underline{\tau}}$  is the viscous stress tensor, and assuming that  $\bar{B} \perp \bar{u}$  (i.e., the magnetic field is perpendicular to the primary flow stream, so that  $\bar{u} \cdot \bar{B} \equiv 0$ ), one has

$$\rho \frac{D\bar{u}}{Dt} = -\nabla p + D \cdot \underline{\underline{\tau}} + \sigma(\bar{E} \times \bar{B} - B^2 \bar{u}).$$

Let the flow be decomposed into two parts  $\bar{u}_0$  and  $\bar{u}'$ ;  $\bar{u}_0$  is the primary part in the absence of the  $\bar{E}$  and  $\bar{B}$  fields, and  $\bar{u}'$  is the part due to the imposed electric and magnetic fields:

$$\rho \frac{D}{Dt}(\bar{u}_0 + \bar{u}') = -\nabla p + D \cdot \underline{\underline{\tau}} + \sigma(\bar{E} \times \bar{B} - B^2(\bar{u}_0 + \bar{u}')).$$

Since  $\bar{u}_0$  satisfies the Navier-Stokes equations in the absence of  $\bar{E}$  and  $\bar{B}$ , one has

$$\rho \frac{D}{Dt} \bar{u}' = \sigma(\bar{E} \times \bar{B} - B^2(\bar{u}_0 + \bar{u}')).$$

Further, assuming that  $\bar{u}' \ll \bar{u}_0$  and  $\bar{E} \times \bar{B}$  is normal to the wall, linearizing the equations gives

$$\rho \frac{\partial}{\partial t} \begin{pmatrix} u' \\ v' \\ w' \end{pmatrix} = \sigma \begin{pmatrix} 0 \\ E \cdot B \\ 0 \end{pmatrix} - \sigma B^2 \begin{pmatrix} u \\ v + v' \\ w \end{pmatrix}.$$

Because of the assumption that the Lorentz pressure gradient is normal to the wall, the normal flow velocity  $v'$  is retained. Solutions to the  $u'$  and  $w'$  are straightforward:

$$u' \approx \frac{\sigma B^2}{\rho} u \tilde{t} \quad \text{and} \quad w' \approx \frac{\sigma B^2}{\rho} w \tilde{t},$$

where  $\tilde{t}$  is the time during which  $\bar{E}(t)$  is active. The normal velocity component equation is

$$\frac{\partial v'}{\partial t} + \frac{\sigma B^2}{\rho} v' - \frac{\sigma E B}{\rho} + \frac{\sigma B^2 v}{\rho} = 0.$$

Assuming that

$$E(t) = E_0 \left( H(0) - H(\tilde{t}) - H\left(\frac{T}{2}\right) + H\left(\frac{T}{2} + \tilde{t}\right) \right),$$

where  $H$  is the one-sided Heaviside function and  $T$  is the period during which  $\bar{E}$  is active, the  $E$  field prescribed is a positive top-hat function from  $t = 0$  to  $\tilde{t}$ , a negative top-hat function from  $t = \frac{T}{2}$  to  $\frac{T}{2} + \tilde{t}$ , and zero elsewhere. Given the microturbulent event phenomenology, the naturally occurring turbulent flow vertical velocity  $v'$  can be expressed as

$$v'(t) = u_\tau e^{i\omega_0 t},$$

where  $\omega_0$  is the burst frequency ( $\omega^+ \cong 0.06$ ). Rewriting the  $v'$  equation, one has

$$\frac{\partial v'}{\partial t} + \frac{\sigma B^2}{\rho} v' - \frac{\sigma B}{\rho} (E_0(t) - Bu_\tau e^{i\omega_0 t}) = 0,$$

so that

$$v' = \frac{\sigma B}{\rho} e^{-\frac{\sigma B^2 t}{\rho}} \int_0^t (E(t) - Bu_\tau e^{i\omega_0 t}) e^{\frac{\sigma B^2 t}{\rho}} dt.$$

Or, over one  $E(t)$  cycle from  $t = 0$  to  $T$ ,

$$\begin{aligned} v' &= \frac{\sigma B}{\rho} e^{-\frac{\sigma B^2 t}{\rho}} \left[ \int_0^{\tilde{t}} E_0 e^{\frac{\sigma B^2 t}{\rho}} dt + \int_{\frac{T}{2}}^{\frac{T}{2} + \tilde{t}} E_0 e^{\frac{\sigma B^2 t}{\rho}} dt - Bu_\tau \int_0^t e^{i\omega_0 t + \frac{\sigma B^2 t}{\rho}} dt \right], \\ &\cong \frac{\sigma B}{\rho} e^{-\frac{\sigma B^2 t}{\rho}} \left[ \frac{\rho E_0}{\sigma B^2} \left( e^{\frac{\sigma B^2 \tilde{t}}{\rho}} - 1 \right) \left( e^{\frac{\sigma B^2 T}{2\rho}} + 1 \right) - \frac{Bu_\tau}{\left( \left( \frac{\sigma B^2}{\rho} \right)^2 - \omega_0^2 \right)} \left( \frac{\sigma B^2}{\rho} e^{\frac{\sigma B^2 t}{\rho}} \cos(\omega_0 t) + \omega_0 \sin(\omega_0 t) - \frac{\sigma B^2}{\rho} \right) \right]. \end{aligned}$$



The typical, practically possible sea water value of  $\sigma B^2 / \rho$  is about 0.001 Hz;  $\omega_0$ , however, is on the order of 100 to 1000 Hz, so that no resonant condition is possible unless both  $\sigma$  and  $B$  are significantly enhanced. Therefore,

$$v' \cong \frac{E_0}{B} e^{-\frac{\sigma B^2 t}{\rho}} \left( e^{\frac{\sigma B^2 \tilde{t}}{\rho-1}} \right) \left( e^{\frac{\sigma B^2 T}{\rho+1}} \right) + \frac{\sigma B^2 u_\tau}{\rho \omega_0^2} e^{-\frac{\sigma B^2 t}{\rho}} \left( \omega_0 \sin(\omega_0 t) + \frac{\sigma B^2}{\rho} e^{-\frac{\sigma B^2 t}{\rho}} \cos(\omega_0 t) - \frac{\sigma B^2}{\rho} \right).$$

Since  $\frac{\sigma B^2 \tilde{t}}{\rho} \ll 1$ ,  $\frac{\sigma B^2 T}{\rho} \ll 1$ , and  $\omega_0 \gg \frac{\sigma B^2}{\rho}$ , so that

$$v' \cong \frac{2E_0}{B} \left( 1 - \frac{\sigma B^2 t}{\rho} \right) \left( \frac{\sigma B^2 \tilde{t}}{\rho} \right) + \frac{\sigma B^2 u_\tau}{\rho \omega_0^2} \left( 1 - \frac{\sigma B^2 t}{\rho} \right) \left( \omega_0 \sin(\omega_0 t) + \frac{\sigma B^2}{\rho} \left( 1 + \frac{\sigma B^2 t}{\rho} \right) \cos(\omega_0 t) - \frac{\sigma B^2}{\rho} \right),$$

or

$$v' \cong \frac{2\sigma E_0 B \tilde{t}}{\rho} + \frac{\sigma B^2 u_\tau}{\rho \omega_0} \sin(\omega_0 t).$$

The coefficient of the second term can be expressed as

$$u_\tau \cdot \frac{\sigma B^2 \ell}{\rho u_\tau} \cdot \left( \frac{u_\tau}{\omega_0 \ell} \right),$$

where  $\ell$  can be considered as the microturbulent scale or, ideally, the MHD dimension. The ratio of these two terms gives

$$\left( \frac{2E_0}{u_\tau B} \right) \cdot (\omega_0 \tilde{t}).$$

Since, typically, the load factor  $\frac{E_0}{u_\tau B} \gg 1$ , and  $\omega_0 \tilde{t} \cong 1$ ,  $v' \cong \frac{2\sigma E_0 B}{\rho} t$ . Unless the flow is

laminar and with injection of electrolyte so that  $\frac{\sigma B^2}{\rho} \cong \omega_0$ , no oscillatory behavior of  $v'$  would be visible in practical applications.

## 5. DISCUSSION OF TEST SERIES DIFFERENCES

Attentive care was taken to ensure that the NUWC controller was operating in exactly the same way as the one constructed by MDTI. Output current levels were found to directly correlate with theoretical values. In addition, visual checks were made and, although not presented in this report, visual verification of the pulsing pattern showed that it correlated exactly with the desired waveform.

Electrode deterioration was also monitored throughout the experiment. For all tests conducted, electrode current output indicated that the electrodes were functioning perfectly. During a repeat series of tests, after the completion of all data acquisition, electrodes were found to have deteriorated, as indicated by a 50% reduction in current levels for equivalent voltages. Five edge electrodes (out of 128) were found to be not functioning. It is inconceivable that these conditions could have adversely affected the vortex wave (produced due to the pulsing of the electrodes).

Additional differences in experimental conditions between the Princeton, MDTI, and NUWC tests have been summarized in table 1. In the Princeton and MDTI tests, the electrical conductivity of the sodium hydroxide solution was approximately one-fourth and one-half, respectively, that of the sodium chloride solution used in the NUWC tests. The MDTI plate in the NUWC tests was located approximately twice the distance downstream that it was in the Princeton/MDTI tests, resulting in Reynolds numbers half the size of those in the Princeton/MDTI test cases for equivalent flow velocities. Unless the vortex wave is extremely sensitive to the boundary layer scaling parameters, it would not be adversely affected for small differences in boundary layer thickness and turbulence.

One major difference between the NUWC and the Princeton/MDTI tests may be the flow quality. Skin friction coefficient data suggested either that the flow conditions in the Princeton and MDTI tests were not fully turbulent or that a significant adverse pressure gradient existed. Either of these factors is likely to be significant for vortex wave production. Enhanced turbulence levels would likely cause the vortex wave to dissipate or become turbulent. With sufficiently high levels of boundary layer turbulence, the vortex wave may not even stay organized.

Another possible major difference between the test series is the presence of adverse pressure gradients. Generally, adverse pressure gradients accelerate phenomena such as vortex breakdown and, therefore, would likely increase diffusion of the vortex wave. These issues need to be examined in future tests.

## 6. CONCLUSIONS

A series of experiments has been conducted in NUWC's sea water tunnel to assess the validity of turbulent drag reduction via magnetohydrodynamics. The drag reduction MHD array plate developed by researchers at Princeton University was provided by McDonnell Douglas Technologies Inc. (MDTI). The controller and an algorithm were constructed by NUWC. Care was taken to collect high-quality skin friction data via hot-film anemometry, and drag data using a sensitive force balance. To improve the quality of the results, data were acquired at sufficiently high sampling frequencies so that any possible drag reduction events would be detected.

Skin friction data showed an 8 to 15% local skin friction reduction for only two cases out of 40. Force balance data consistently showed little, if any, drag reduction—possibly on the order of 5%. It was concluded that the Princeton electromagnetic turbulence control technique demonstrated no definitive global drag reduction based on force balance data, but did produce a consistent 8% local skin friction reduction at 3.4 meters/second that was repeatedly detected. These results were in sharp contrast with the claims of 90% drag reduction made by researchers at Princeton (Nosenchuck, 1992-1996).

NUWC conducted additional tests to ensure that the instrumentation was functioning properly. Force balance data were checked and rechecked with average values wholly consistent with turbulent shear stress calculations. Turbulence histograms of the shear stress showed a Rayleigh distribution consistent with known, documented results (Meng, 1995). As expected, these histograms were self-similar across the entire velocity regime examined. Power spectra were also computed and found to be consistent with known spectra for turbulent flow, and the first moment of the power spectrum showed peak velocity fluctuations consistent with microturbulent event scales—specifically, the burst frequency.

## 7. FUTURE DEVELOPMENT

A focused program of testing and evaluation of electromagnetic flow control is proposed. Previous work has shown that electromagnetic forces can be effective in modifying both the mean flow and fluctuations in boundary layer flows, but fundamental questions concerning net drag reduction and the physical mechanism and behavior of these complex MHD flows remain unanswered. The three-phase program proposed here includes near-term, proof-of-the-concept demonstration tests intended to be a complementary assessment and experimental confirmation of electromagnetic flow control technology. An assessment of competing hypotheses will reduce the risk in present ARPA/MDTI program and compress the schedule by providing a parallel path for technical progress. The tests will measure the change in total drag that results from the application of electromagnetic forces directly with a load cell in NUWC's sea water test facility using sea water as the test medium. Using real sea water is critical to MHD testing. MHD propulsion experiments at NUWC and other laboratories have shown that hydrodynamic behavior, particularly electrode surface chemistry and bubble dynamics, is markedly different in real sea water versus in manmade salt water, even when the salt water is made from the same salts found in natural sea water. The proposed drag measurements will incorporate all of the lessons learned so far in MHD investigations, with additional flow measurements of turbulent and microturbulent events, to provide a low-cost, timely demonstration.

Some basic issues must be resolved before any credibility can be established; therefore, in the first phase of the proposed program, basic physics and detailed turbulence physics will be examined with and without MHD. An MHD plate will be built by exploiting the recent Princeton test results but using durable, rare earth-coated titanium electrodes (rather than stainless steel ones) to allow testing in real sea water (instead of sodium hydroxide solution) at the NUWC water tunnel under more realistic and controlled flow conditions and at higher speeds. In addition, a novel porous silica glass oxygen electrode, developed in Japan (Muroya, 1991) will be evaluated for its potential in MHD applications, where gas management is a major concern. Initial testing will use the electrode current control scheme based on Princeton's roller vortex (or spanwise vortex resonance) theory. The principal objective of this phase of the testing will be to confirm the drag and turbulence reduction observed at low speed in the Princeton flume and extend the parameter range to higher speed in real sea water. These tests will take full advantage of MDTI's recent lessons learned and Princeton's shear stress database. Use of the full MDTI/Princeton/NUWC team will maximize synergy.

Recent theoretical work at NUWC has attempted to explain electromagnetic turbulence reduction using a model based on the microturbulence production cycle (Meng, 1995). A stochastic model of the vortex formation-ejection-sweep cycle as a Markov process reveals simple geometric relationships that can be used to design a phased array for turbulence suppression. The essence of the theory is the hypothesis that there are detectable changes in the surface shear stress, or other measurable quantities, that can be used to estimate the local phase of the microturbulence production cycle. Based on this phase and the turbulence probability distributions, an appropriate Lorentz force can be time-phase locked and applied to counter or limit turbulence production. The geometric properties of turbulence production are used to predict the Lorentz force distribution over the entire MHD array. The Markov model will be developed and used to design an optimized MHD array and controller. The new array and its controller will then be evaluated in a series of tests in the NUWC sea water flow tunnel, and its performance will be compared with that of the plate and controller based on the Princeton's spanwise vortex resonance hypothesis. These activities are the main thrusts of the second phase of the proposed program.

From the results of the hypothesis evaluation program, the performance MHD devices will be confirmed and optimized. Advanced designs, using the results of the physical modeling work outlined above, will then be used to explore the utilization of several Lorentz force configurations in realistic naval operating conditions. Once the proposed confirmation tests are successfully concluded, a series of demonstrations will be conducted on other test configurations. Follow-on tests will use the Navy's Buoyant Test Vehicle (BTV) and Torpedo Silencing Research Vehicle (TSRV) to support measurements of the benefits of MHD technology in the reduction of drag forces and in acoustic quieting. Then, an application program will be formulated using the knowledge gained in the confirmation physics work to identify undersea applications for prototype evaluation. The third phase of the program will focus on BTV/TSRV tests of the most effective turbulence control configuration options.

Each phase of the proposed program is described in greater detail below.

**Phase 1: Basic Turbulence Statistics Measurements in Sea Water with Electromagnetics.** The first step in this phase is to build two plates—one with axial magnets and segmented electrodes, and another without the magnets. The plates will then be mounted in a drag balance to measure overall drag without the effects of MHD. Next, the effect of electrolytic bubbles and Lorentz forces on mean/fluctuating flow and wall quantities in sea water will be measured for both plates. These measurements should resolve the effect of bubbles on the flow. NUWC's sea water electrochemistry experiments investigating bubble formation on electrode surfaces and the durability of electrode materials will be a part of this test. Alternative electrodes will be evaluated, with samples of porous silica glass electrodes recently developed in Japan, in sodium chloride and sea water to evaluate their performance and potential for mitigating gas generation.

An experiment will be conducted to test the hypothesis that application of a wall-normal Lorentz force can modify the probability density functions of wall shear stress and subsequently reduce turbulence. The proposed experiment will be conducted in the NUWC sea water tunnel using an MHD plate to be constructed by NUWC. The plate (Hendricks, 1996) has 16 rows of electrodes in the streamwise direction and 8 rows of electrodes in the spanwise direction. Permanent magnets located between each row of electrodes alternate north to south. Therefore, a vertical Lorentz force is produced directly between two adjacent electrodes. To minimize the effects of cross-currents, alternate rows of electrodes will be powered by separate power supplies. The entire array of electrodes will be pulsed in the form of a square wave at a 25% duty cycle. A given row consists of one pair of four electrodes (eight electrodes). The pulsing sequence will be such that a given electrode will be of positive polarity for 25% of the cycle, negative polarity for 25% of the cycle, and turned off for 50% of the cycle. The pulsing patterns of subsequent rows of electrodes will be staggered so that a  $12^\circ$  angle is produced in the downstream direction. This pattern matches the well-established probabilistic occurrence of microturbulent events. Positive and negative polarity will be applied to inhibit ejection and sweep events and results will be compared.

$u, u', v, v', p'_{wall}$ , Reynolds stress, and total drag will be measured using LDV, hot-film sensors, hot-wire sensors, pitot tubes, a drag balance, and flow visualization. These measurements will be compared to determine which techniques are most suitable for making measurements with this technology. Measurements will be made over a wide range of MHD interaction numbers, and the persistence downstream for the constant EM field will be determined.

Key flow variables can be measured only by LDV. However, the limiting factor in using LDV to measure the mean and fluctuating velocity very near the wall stems from the

focal volume. This volume is fixed, but as the flow speed increases, the focal volume in terms of wall units increases linearly in direct proportion to the flow speed. The focal volume, the boundary layer thickness, and the expected height of maximum turbulence production will be plotted against flow speed to optimize the utility of the LDV instrumentation. An additional beam expander will be applied to reduce the focal volume further, and it is expected that LDV data will be useful for flow speeds of about 1 meter/second.

The velocity profile in the log law region of a turbulent boundary layer is described by

$$u/u_\tau = 1/\kappa \ln(u_\tau y/\nu) + B,$$

where  $\kappa = 0.4$ , and  $B = 5.5$  for all Reynolds number flows. For rough surfaces, the above equation is modified with the addition of a function  $F$  of the surface roughness parameter (Nikuradse, 1926; Schlichting, 1936). For flow with drag reduction devices, it has been found by Sawyer and Winter (1987), Gaudet (1987), and Tani (1988) that the velocity profile can still be expressed in the same way, i.e.,

$$u/u_\tau^* = 1/\kappa \ln(u_\tau^* y/\nu) + B + F,$$

but the  $y$  must be shifted and  $u_\tau^*$  is the apparent friction velocity with drag reduction. It has been found in flows with polymer injection and flows over riblets that the virtual origin of the log-law is pushed away from the wall by a shift. This shift is related to the drag reduction achieved. All existing methods for evaluating the virtual origin are based on changes in the mean streamwise velocity rather than on changes in turbulence structure. Since MHD drag reduction is premised on modifying turbulence production, analysis of LDV data should relate the drag reduction to modified turbulence production. Such a concept has been proposed previously by Choi et al. (1993), whose approach is summarized below.

Since the maximum turbulence production and the maximum intensity of the streamwise velocity fluctuations coincide at  $y^+ \approx 13$ , Choi et al. (1993) defined

$$13 = (y_m - y_0) u_\tau^*/\nu,$$

or

$$y_0 = y_m - 13 \nu/u_\tau^*,$$

where  $u_\tau^*$  is the apparent friction velocity with drag reduction, and  $y_m$  is the location of the measured maximum streamwise velocity fluctuations. Once  $u_\tau^*$  and  $y_0$  are defined, the parameter  $F$ , which can relate to drag reduction, can be determined. This calculation provides another method for inferring drag reduction should the drag balance not function properly. Based on past databases, Gaudet (1987) indicated that positive  $F$  values imply a drag reduction, while negative ones imply a drag increase. Specifically, the LDV analysis steps are as follows: (1) Obtain both the mean streamwise velocity and velocity fluctuation to as close to  $y^+ < 10$  as possible. (2) Obtain the friction velocity  $u_\tau^*/\nu$ . (3) Plot the streamwise velocity fluctuation versus  $y$ . (4) Obtain  $y_m$  and  $y_0$ . (5) Plot the mean streamwise velocity versus  $y$ . (6) Obtain  $F$ ,  $\delta^+$ ,  $\theta$ , and  $H$  factor. (7) Correlate  $F$ ,  $H$  versus drag reduction empirical data obtained by Tani (1988).

Several experimental data acquisition methods will be applied to ensure the quality and reliability of the results. Hot-film anemometry will be used to obtain the local skin friction. Three hot-film sensors will be located immediately downstream of the array and will be spaced from the center of the plate to one edge. This spacing will demonstrate any spanwise variation in force and will help determine whether local skin friction reduction at one section results in a skin friction increase in another. Two additional hot-film sensors will be located downstream of the array along the centerline to measure the persistence of the Lorentz force. Particle image velocimeters (PIVs) will be used to measure boundary layer velocity distribution and the local skin friction, as well as for flow visualization and to obtain boundary layer vorticity distributions. Hot-wire anemometry will be used to approximate the boundary layer turbulence near the wall, and force balance data will be used to determine global drag reduction.

Analysis of the experimental data will focus on the statistical quantities of the hot-wire and hot-film data. Mean boundary layer and near-wall turbulence can be approximated with the hot-wire sensors. PDFs of the wall shear stress can be obtained from the hot-film data. Unsteady hot-film data will provide PDFs of the microturbulent events. Data collected at various pulsing frequencies and voltages will be compared with baseline measurements to gauge the influence of applying the Lorentz force.

**Phase 2a: Assessment of Spanwise Vortex Resonance Hypothesis.** In this phase, the wall layer microturbulent events and scales will be thoroughly reviewed, paying particular attention to the microturbulence phenomenology and the scaling relationships of microturbulent events in light of more recent reporting of additional Reynolds number dependence. The dynamic relationships of these events will be reexamined, and the consistency of published results of other drag and noise reduction investigations will be verified. The MHD plate will then be constructed accordingly, including rare earth-coated titanium electrodes for sea water durability with improved diagnostics. A thorough set of parametric experiments with the MHD plate will be conducted to demonstrate its performance in salt water or sea water over a range of conditions, including testing on a 3-inch-diameter torpedo on a sting in NUWC's tow tank. The parameter range will be designed to obtain supportable performance predictions for the planned torpedo-scale tests in the Langley Tow Tank.

**Phase 2b: Assessment of Markov Control of the Streak-Sweep-Eject Hypothesis.** The first step in this phase is to refurbish NUWC's 0.5- by 0.5-foot MHD turbulence control plate with 1/8-inch magnets and electrodes. Assuming that the wall-normal mode will be used for the proof-of-concept experiment for Markov control of the streak-sweep-eject process, the plate will be rewired so that the electrode spacing in the streamwise and spanwise directions will match, as closely as possible, the streak-sweep-eject scaling for flow found in the turbulence data literature. A frequency pulsing to produce wall-normal body forces with repeated patterns at subsequent downstream locations approximately  $12^\circ$  apart in the streamwise direction will be the goal. The design will be analyzed for electric and magnetic field shapes, Lorentz force, and field strengths. Additional predictions of device test performance such as estimated skin friction reduction and power requirements will be made. Photographs will be taken at several intermediate stages of refurbishment and rewiring to document the process. The final configuration will be fitted and demonstrated in the test fixture.

Next, the probabilistic model of naturally occurring microturbulent events will be further refined by rederiving the Markov transitional probability equations—using Poisson arrival rates to develop further details of the Markov process—and by relating the transitional probability to the experimentally obtained database of microturbulent events for either the shear stress histograms or the spectral density in terms of the inner scaling parameters. In light of the mathematical results, the feasibility of the Markov concept as a real-time technique for



characterizing and controlling microturbulent events will be reexamined. A Markov controller will then be fabricated for use in the MHD plate. A detailed test plan for performing the proof-of-concept experiment will be developed, and confirmation tests of Markov control of the streak-sweep-eject process will be conducted. The Markov control MHD plate will be integrated with the drag balance in the water tunnel flat plate. The plate will be instrumented with flush-mounted hot-film sensors and flush-mounted wall pressure transducers. These sensors will provide feedback for the Markov controller, as well as turbulent flow diagnostics. The planned instrumentation will include a drag balance, LDV, hot-film sensor rake, and flow visualization. Checkout runs will be conducted to verify operation of the test apparatus, instrumentation, and data recording and processing systems.

A report will be produced that includes design of the plate, results of the review of the turbulent event analysis, a complete discussion of the theory underlying Markov control for control of the streak-sweep-eject process, and an analysis and interpretation of the experimental data in conjunction with the theoretical underpinnings of the Markov process. An uncertainty analysis of the data will also be performed. Estimates of device performance for naval applications will be made with regard to skin friction reduction, power requirements, and flow properties. These results will be compared with predicted performance. If these tests are successful, the Langley tow tank test will be conducted.

Based on the Phase 2a and 2b assessments of both approaches, variable Lorentz pressure gradient vector optimization will be carried out via spaced electrode and periodic axial measurements. Segmented electrode aspects of the best control algorithm will be used by wiring a sparse array of electrodes together so that the spacing between electrodes is on the order of the persistence length found above. Measurements will be made to minimize the power and volume of the system while still retaining  $C_f$  levels as in the baseline experiment. The same parameters as before will be measured and the temporal persistence effect will be quantified. Given the spatial and temporal persistence scales found previously, along with guidance by three-dimensional and time-dependent computational fluid dynamics codes, an optimal MHD plate will be designed.

**Phase 3: Self-Noise and Radiated Noise Reduction Measurements.** For any ultimate application of MHD to tactical underwater vehicles, noise issues must be addressed. There are two major noise sources for such vehicles—self-noise and radiated noise. Self-noise, which affects the ability of the vehicle's sonar system to detect distant signals, is the noise associated with the turbulent boundary layer and hull vibrations transmitted by hull conductance. Radiated noise is the noise conducted to the sea water environment and propagated to distant points. Many sources contribute to a vehicle's radiated noise, but the primary contributor is the propulsion system, including the engine and its associated rotating machinery parts.

For MHD testing, the self-noise and radiated noise issues can be negated by using the BTV as the application test bed. The self-noise of the BTV has been reduced to a minimum by hull design and damping. For self-noise, it is proposed that a ring of pressure transducers be mounted on the BTV's nose to measure local pressure fluctuations. Tests would then be conducted with and without MHD operating. The measured self-noise level could then be translated into sonar performance predictions using established analytical models.

The BTV has no propulsion system or moving machinery and, thus, this primary contributor to radiated noise is not a factor. The direct radiated noise produced by flow over the hull of the BTV has been measured and is a known quantity. For other sources of radiated noise, hull transfer function measurements with and without MHD panels installed should be made. These measurements could then be used in conjunction with available analytical models to predict total flow noise with and without MHD.

## 8. BIBLIOGRAPHY

- Bandyopadhyay, P.R., and J.M. Castano (1996), "Micro-tiles for Electromagnetic Turbulence Control in Saltwater, Preliminary Investigations," *Proceedings of Symposium on Turbulence Modification and Drag Reduction, ASME Summer Meeting, San Diego, CA, July 7-11, 1996*, FED Volume 237, vol. 2, pp. 415-421.
- Benney, D.J., and L.H. Gustavsson (1981), "Direct Resonance in Turbulent Boundary Layers," *Studies in Applied Mathematics*, vol. 64, p. 185.
- Blackwelder, R.F. (1983), "Similarity Between the Laminar-Turbulent Transition and Turbulent Boundary Layer Bursting," *Physics of Fluids*, vol. 26, p. 2807.
- Castano, John (1997), "Flexural Drag Balance," NUWC-NPT Technical Memorandum (in preparation), Naval Undersea Warfare Center Division, Newport, RI.
- Choi, H., P. Moin, and J. Kim (1993), "Direct Numerical Simulation of Turbulent Flow Over Riblets," *Journal of Fluid Mechanics*, vol. 255, pp. 503-539.
- Crawford, C., and G. Karniadakis (1966), "Reynolds Stress Analysis of EMHD-Controlled Wall Turbulence, Part I: Streamwise Forcing," Center for Fluid Mechanics, Turbulence, and Computation, Brown University, Providence, RI.
- Culver, H.C.M. (1996), "An Experimental Investigation of a Laminar Boundary Layer Subject to an Applied Lorentz Force," Master's Thesis, Princeton University.
- Gaudet, L. (1987), "An Assessment of the Drag Reduction Properties of Riblets and the Penalties of Off-Design Conditions," RAE TM Aero 2113, Royal Aircraft Establishment.
- Eng, T.I. (1995), "A Laminar Boundary Layer Response to an Electromagnetic Forcing," Master's Thesis, Princeton University.
- Hendricks, Peter J. (1996), "An Electromagnetic Array for Turbulence Control," NUWC-NPT Technical Memorandum 962137, Naval Undersea Warfare Center Division, Newport, RI.
- Henoch, C., and J. Stace (1995), "Experimental Investigation of a Salt Water Turbulent Boundary Layer Modified by an Applied Streamwise Magnetohydrodynamic Body Force," *Physics of Fluids*, vol. 6, pp 1371-1383.
- Huyer, S.A. (1995), "Current Pulsing as a Means to Reduce Bubble Production by MHD Electrodes," NUWC-NPT Technical Report 10,534, Naval Undersea Warfare Center Division, Newport, RI.
- Jang, P.S., D.J. Benney, and R.L. Gran (1986), "On the Origin of Streamwise Vortices in a Turbulent Boundary Layer," *Journal of Fluid Mechanics*, vol. 169, pp. 109-123.
- Kim, H.T.S., S.J. Kline, and W.C. Reynolds (1971), "The Production of Turbulence Near a Smooth Wall in a Turbulent Boundary Layer," *Journal of Fluid Mechanics*, vol. 50, part 1, pp. 133-160.
- Kral L. (1996), "Numerical Simulations of Electromagnetic Control of Turbulence," Abstract of a paper presented at the *ASME Fluids Engineering Meeting, Active Control Section*, Ithaca, NY, November.

- Meng, J.C.S. (1995), "Wall Layer Microturbulence Phenomenology and a Markov Probability Model for Active Electromagnetic Control of Turbulent Boundary Layers in an Electrically Conducting Medium," NUWC-NPT Technical Report 10,434, Naval Undersea Warfare Center Division, Newport, RI.
- Morrison, W.R.B., K.J. Bullock, and R.E. Kronauer (1971), "Experimental Evidence of Waves in the Sublayer, *Journal of Fluid Mechanics*, vol. 47, pt. 4, pp. 639-656.
- Muroya, M. (1991), "Anode for Superconducting MHDs, Materials and Efficiency," *Proceedings of the International Symposium on Superconducting Magnetohydrodynamic Ship Propulsion, MHDS 91*, Kobe, Japan, p. 359.
- Nikuradse, J. (1926), "Untersuchungen über die Geschwindigkeitsverteilung in Turbulenten Strömungen," Thesis Göttingen, VDI-Forschungsheft 281, Berlin.
- Nosenchuck, D.M. (1995a), Technical discussion on 24 March 1995 at Princeton University.
- Nosenchuck, D.M. (1995b), Technical discussion on 27 July 1995 at San Diego, CA.
- Nosenchuck, D. (1996), "Boundary Layer Control Using the Lorentz Force on an Axisymmetric Body," Abstract of a paper presented at the *ASME Fluids Engineering Meeting, Active Control Section*, Ithaca, NY, November.
- Nosenchuck, D.M., and G.L. Brown (1992), "The Direct Control of Wall Shear Stress in a Turbulent Boundary Layer in Single and Multiple Domains," MAE Report T1954, Princeton University.
- Nosenchuck, D.M., and G.L. Brown (1993), "Discrete Spatial Control of Wall Shear Stress in a Turbulent Boundary Layer," in *Proceedings of International Conference on Near-Wall Turbulent Flows*, C.G. Speziale and B.E. Launder, eds., Arizona State University, 15-17 March.
- Nosenchuck, D., and Garry L. Brown (1994a), "Electromagnetic Device and Method for Boundary Layer Control," U.S. Patent 5,320,309.
- Nosenchuck, D., and G. Brown (1994b), "Electromagnetic Turbulent Boundary Layer Control," *Bulletin of the American Physical Society*, vol. 39, no. 4, p. 1938.
- Nosenchuck, D., and Garry L. Brown (1995), "Multiple Electromagnetic Tiles for Boundary Layer Control," U.S. Patent 5,437,421.
- Sawyer, W.G., and K.G. Winter (1987), "An Investigation of the Effect on Turbulent Skin Friction of Surfaces with Streamwise Grooves," RAE TM Aero 2112, Royal Aircraft Establishment.
- Schlichting, H. (1979), *Boundary Layer Theory*, Seventh Edition, McGraw-Hill, New York.
- Sreenivasan, K.R., and R.A. Antonia (1977), "Properties of Wall Shear Stress Fluctuations in a Turbulent Duct Flow," *Journal of Applied Mechanics, Transactions of the ASME*, vol. 44, p. 389.
- Stimson (1995), Private Communications.

- Tani, I. (1988), "Drag Reduction by Riblet Viewed as Roughness Problem, *Proceedings of Japan Academy*, B vol. 64, p. 21.
- Tsinober, A. (1990), "MHD-Drag Reduction," in *Viscous Drag Reduction in Boundary Layers*, *AIAA Progress in Aeronautics and Astronautics Series*, vol. 123, D.M. Bushnell and J.N. Hefner, eds, pp. 327-349.
- Watanabe, T. (1978), "Magnetohydrodynamic Stability of Boundary Layers Along a Flat Plate in the Presence of a Transverse Magnetic Field," *Zeitschrift fuer Angewandte Mathematik und Mechanik*, vol. 58, pp. 555-560.
- Watanabe, T. (1987), "Magnetohydrodynamic Stability of Boundary Layer Flow with Suction or Injection Along a Flat Plate," *Zeitschrift fuer Angewandte Mechanik*, vol. 67, no. 1, pp. 27-30.

## APPENDIX EXPERIMENT TEST MATRIXES

Tables A-1 and A-2 list the MDTI and Princeton test matrixes, respectively. Based on the values in tables A-1 and A-2, the NUWC test plan in table A-3 was developed.

*Table A-1. MDTI Test Matrix*

Data File Name	Velocity (m/s)	Volts Applied	Amps Measured	Frequency Applied	$f_{\text{Nosenchuck}}$	$f_{\text{Bandy}}$	$V_{\text{bubble}}$	$f_{\text{bubble}}$	Electrical Conductivity	MHD Interaction Parameter	Load Factor
MD101	1	0	0		400	5			15	0.00	0
MD102	1	15	8.3	30	400	5	13	42	15	101.25	27231
MD103	1	0	0		400	5			15	0.00	0
MD104	1	7.5	4.14	30	400	5	13	6	15	50.63	13583
MD105	1	0	0		400	5			15	0.00	0
MD106	1	15	8.3	60	400	5	17	42	15	101.25	27231
MD107	1	0	0		400	5			15	0.00	0
MD108	1	15	8.3	50	400	5	16	42	15	101.25	27231
MD201	2	0	0		1600	20			15	0.00	0
MD202	2	15	8.4	60	1600	20	17	42	15	25.31	13780
MD203	2	0	0		1600	20			15	0.00	0
MD204	2	10.00	5.86	60	1600	20	17	13.5	15	16.88	9612.9
MD205	2	0			1600	20			15	0.00	0
MD206	2	5	2.91	60	1600	20	17	1.95	15	8.44	4773.6
MD207	2	0			1600	20			15	0.00	0
MD208	2	25	14.7	60	1600	20	17	176	15	42.19	24114
MD251	2.5	0			2500	32			15	0.00	0
MD252	2.5	10	5.88	75	2500	32	18.5	13.5	15	10.80	7716.5
MD253	2.5	0			2500	32			15	0.00	0
MD254	2.5	25	14.71	75	2500	32	18.5	176	15	27.00	19304
MD401	4	0			6400	81			15	0.00	0
MD402	4	25	14.71	120	6400	81	22	176	15	10.55	12065
MD403	4	0			6400	81			15	0.00	0
MD404	4	15	8.48	120	6400	81	22	42	15	6.33	6955.4
MD405	4	0			6400	81			15	0.00	0
MD406	4	20	11.68	120	6400	81	22	94	15	8.44	9580.1
MD501	5	0			10000	127			15	0.00	0
MD502	5	25	14.5	150	10000	127	24	176	15	6.75	9514.4

*Table A-2. Princeton Test Matrix*

Data File Name	Velocity (m/s)	Volts Applied	Amps Measured	Frequency Applied	$f_{\text{Nosenchuck}}$	$f_{\text{Bandy}}$	$V_{\text{bubble}}$	$f_{\text{bubble}}$	Electrical Conductivity	MHD Interaction Parameter	Load Factor
PI01	1	0			400	5			7.5	0.00	0
PI02	1	5.5	2.95	50	400	5	16	2.5	7.5	18.56	9678.5
PI41	1.4	0			784	10			7.5	0.00	0
PI42	1.4	6	3.15	50	784	10	16	3.25	7.5	10.33	7381.9
PI81	1.8	0			1296	17			7.5	0.00	0
PI82	1.8	6	3.18	100	1296	17	20.5	3.25	7.5	6.25	5796.2

**Table A-2. Princeton Test Matrix (cont'd)**

Data File Name	Velocity (m/s)	Volts Applied	Amps Measured	Frequency Applied	$f_{\text{Nosenchuck}}$	$f_{\text{Bandy}}$	$V_{\text{bubble}}$	$f_{\text{bubble}}$	Electrical Conductivity	MHD Interaction Parameter	Load Factor
P231	2.3	0			2116	27			7.5	0.00	0
P232	2.3	8	4.21	150	2116	27	24	7.25	7.5	5.10	6005.4
P271	2.7	0			2916	37			7.5	0.00	0
P272	2.7	10	5.5	150	2916	37	24	13.5	7.5	4.63	6683.2
P301	3	0			3600	46			7.5	0.00	0
P302	3	10	5.88	130	3600	46	22.5	13.5	7.5	3.75	6430.4
P303	3	0			3600	46			7.5	0.00	0
P304	3	12	6.96	130	3600	46	22.5	22.5	7.5	4.50	7611.5
P305	3	0			3600	46			7.5	0.00	0
P306	3	15	8.46	130	3600	46	22.5	42	7.5	5.63	9252
P307	3	0			3600	46			7.5	0.00	0
P308	3	17	9.7	130	3600	46	22.5	60	7.5	6.38	10608
P309	3	0			3600	46			7.5	0.00	0
P3010	3	21	12.18	130	3600	46	22.5	108	7.5	7.88	13320
P3011	3	0			3600	46			7.5	0.00	0
P3012	3	10	5.85	150	3600	46	24	13.5	7.5	3.75	6397.6
P3013	3	0			3600	46			7.5	0.00	0
P3014	3	10	5.85	180	3600	46	25	13.5	7.5	3.75	6397.6
P3015	3	0			3600	46			7.5	0.00	0
P3016	3	10	5.86	250	3600	46	28.25	13.5	7.5	3.75	6408.6
P3017	3	0			3600	46			7.5	0.00	0
P3018	3	12	6.96	180	3600	46	25	22.5	7.5	4.50	7611.5
P3019	3	0			3600	46			7.5	0.00	0
P3020	3	15	8.41	180	3600	46	25	42	7.5	5.63	9197.3
P341	3.4	0			4624	59			7.5	0.00	0
P342	3.4	21	11.58	150	4624	59	24	108	7.5	6.13	11174
P371	3.7	0			5476	70			7.5	0.00	0
P372	3.7	21	12.14	150	5476	70	24	108	7.5	5.18	10765
P373	3.7	0			5476	70			7.5	0.00	0
P374	3.7	17	9.5	50	5476	70	16	60	7.5	4.19	8423.8
P375	3.7	0			5476	70			7.5	0.00	0
P376	3.7	17	9.59	100	5476	70	20.5	60	7.5	4.19	8503.6
P377	3.7	0			5476	70			7.5	0.00	0
P378	3.7	17	9.6	130	5476	70	22.5	60	7.5	4.19	8512.4
P379	3.7	0			5476	70			7.5	0.00	0
P3710	3.7	17	9.61	150	5476	70	24	60	7.5	4.19	8521.3
P3711	3.7	0			5476	70			7.5	0.00	0
P3712	3.7	17	9.61	200	5476	70	26.25	60	7.5	4.19	8521.3
P3713	3.7	0			5476	70			7.5	0.00	0
P3714	3.7	17	9.6	300	5476	70	30.25	60	7.5	4.19	8512.4
P3715	3.7	0			5476	70			7.5	0.00	0
P3716	3.7	17	9.6	500	5476	70	36	60	7.5	4.19	8512.4

**Table A-3. NUWC Test Plan**

Data File Name	Velocity (m/s)	Volts Applied	Amps Measured	Frequency Applied	f <sub>Nosenchuck</sub>	f <sub>Bandy</sub>	V <sub>bubble</sub>	f <sub>bubble</sub>	Electrical Conductivity	MHD Interaction Parameter	Load Factor
NU401	4	0			6400	81			26.6	0.00	0
NU402	4	10	5.29	30	6400	81	13	13.5	26.6	7.48	4338.9
NU403	4	0			6400	81			26.6	0.00	0
NU404	4	10	5.3	40	6400	81	14	13.5	26.6	7.48	4347.1
NU405	4	0			6400	81			26.6	0.00	0
NU406	4	10	5.36	60	6400	81	17	13.5	26.6	7.48	4396.3
NU407	4	0			6400	81			26.6	0.00	0
NU408	4	10	5.36	70	6400	81	18	13.5	26.6	7.48	4396.3
NU413	4	0			6400	81			26.6	0.00	0
NU414	4	5	2.56	70	6400	81	18	1.95	26.6	3.74	2099.7
NU415	4	0			6400	81			26.6	0.00	0
NU416	4	13	7.8	70	6400	81	18	42	26.6	11.22	6397.6
NU417	4	0			6400	81			26.6	0.00	0
NU418	4	25	13.63	70	6400	81	18	176	26.6	18.70	11179
NU419	4	0			6400	81			26.6	0.00	0
NU420	4	10	5.4	250	6400	81	28.25	13.5	26.6	7.48	4429.1
NU421	4	0			6400	81			26.6	0.00	0
NU422	4	10	5.4	400	6400	81	34	13.5	26.6	7.48	4429.1
NU423	4	0			6400	81			26.6	0.00	0
NU424	4	10	5.4	500	6400	81	36	13.5	26.6	7.48	4429.1
NU425	4	0			6400	81			26.6	0.00	0
NU426	4	5	2.65	500	6400	81	36	1.95	26.6	3.74	2173.6
NU427	4	0			6400	81			26.6	0.00	0
NU428	4	15	7.83	500	6400	81	36	42	26.6	11.22	6422.2
NU429	4	0			6400	81			26.6	0.00	0
NU430	4	25	13.68	500	6400	81	36	176	26.6	18.70	11220
NU431	4	0			6400	81			26.6	0.00	0
NU432	4	40	21.8	500	6400	81	36	900	26.6	29.93	17881
NU433	4	0			6400	81			26.6	0.00	0
NU434	4	10	5.23	600	6400	81	37	13.5	26.6	7.48	4289.7
NU435	4	0			6400	81			26.6	0.00	0
NU436	4	10	5.21	700	6400	81	38	13.5	26.6	7.48	4273.3
NU437	4	0			6400	81			26.6	0.00	0
NU438	4	40	21.8	600	6400	81	37	900	26.6	29.93	17881
NU439	4	0			6400	81			26.6	0.00	0
NU440	4	40	21.8	700	6400	81	37	900	26.6	29.93	17881
NU501	5	0			10000	127			26.6	0.00	0
NU502	5	10	4.8	20	10000	127	11	13.5	26.6	4.79	3149.6
NU503	5	0			10000	127			26.6	0.00	0
NU504	5	10	4.8	40	10000	127	14	13.5	26.6	4.79	3149.6
NU505	5	0			10000	127			26.6	0.00	0
NU506	5	10	4.8	80	10000	127	19	13.5	26.6	4.79	3149.6
NU507	5	0			10000	127			26.6	0.00	0
NU508	5	10	4.84	90	10000	127	20	13.5	26.6	4.79	3175.9
NU509	5	0			10000	127			26.6	0.00	0
NU510	5	10	4.84	100	10000	127	21	13.5	26.6	4.79	3175.9
NU511	5	0			10000	127			26.6	0.00	0
NU512	5	10	4.88	200	10000	127	27	13.5	26.6	4.79	3202.1
NU513	5	0			10000	127			26.6	0.00	0
NU514	5	5	2.24	100	10000	127	21	1.95	26.6	2.39	1469.8
NU515	5	0			10000	127			26.6	0.00	0
NU516	5	20	10.15	100	10000	127	21	94	26.6	9.58	6660.1



**Table A-3. NUWC Test Plan (cont'd)**

Data File Name	Velocity (m/s)	Volts Applied	Amps Measured	Frequency Applied	$f_{\text{Nosenchuck}}$	$f_{\text{Bandy}}$	$V_{\text{bubble}}$	$f_{\text{bubble}}$	Electrical Conductivity	MHD Interaction Parameter	Load Factor
NU517	5	0			10000	127			26.6	0.00	0
NU518	5	40	21	100	10000	127	21	900	26.6	19.15	13780
NU519	5	0			10000	127			26.6	0.00	0
NU520	5	20	10.11	250	10000	127	28.25	94	26.6	9.58	6633.9
NU521	5	0			10000	127			26.6	0.00	0
NU522	5	20	10.13	500	10000	127	36	94	26.6	9.58	6647
NU523	5	0			10000	127			26.6	0.00	0
NU524	5	5	2.33	500	10000	127	36	1.95	26.6	2.39	1528.9
NU525	5	0			10000	127			26.6	0.00	0
NU526	5	10	4.86	500	10000	127	36	13.5	26.6	4.79	3189
NU527	5	0			10000	127			26.6	0.00	0
NU528	5	30	15.64	500	10000	127	36	250	26.6	14.36	10262
NU529	5	0			10000	127			26.6	0.00	0
NU530	5	40	20.9	500	10000	127	36	900	26.6	19.15	13714
NU531	5	0			10000	127			26.6	0.00	0
NU532	5	30	15.51	550	10000	127	37	250	26.6	14.36	10177
NU533	5	0			10000	127			26.6	0.00	0
NU534	5	30	15.51	650	10000	127	38	250	26.6	14.36	10177
NU535	5	0			10000	127			26.6	0.00	0
NU536	5	30	15.51	750	10000	127	39	250	26.6	14.36	10177
NU537	5	0			10000	127			26.6	0.00	0
NU538	5	30	15.5	850	10000	127	40	250	26.6	14.36	10171



## INITIAL DISTRIBUTION LIST

Addressee	No. of Copies
Defense Advanced Research Projects Agency (G. Jones)	2
Naval Sea Systems Command (SEA92R, PMS404)	2
Office of Naval Research (K. Conner, J. Fein, S. Lekoudis, P. Purtell, E. Rood, R. Vogelsong)	6
Naval Surface Warfare Center (Technical Library)	1
Naval Research Laboratory (Technical Library)	1
Naval Postgraduate School (Technical Library)	1
Applied Physics Laboratory, Johns Hopkins University (Technical Library)	1
Princeton University (D. Nosenchuck, G. Brown)	2
McDonnell Douglas Technologies Inc. (E. Garner, D. Parekh, J. Donovan)	3
Newport News Shipbuilding (J. Casper)	1
National Aeronautics and Space Administration (D. Bushnell)	1
Defense Technical Information Center	12
Center for Naval Analyses	1